

Development of Nanosphere Lithography Technique with Enhanced Lithographical
Accuracy on Periodic Si Nanostructure for Thin Si Solar Cell Application

by

Jeayoung Choi

A Dissertation Presented in Partial Fulfillment
of the Requirements for the Degree
Doctor of Philosophy

Approved March 2015 by the
Graduate Supervisory Committee:

Christiana Honsberg, Co-Chair
Terry Alford, Co-Chair
Stephen Goodnick

ARIZONA STATE UNIVERSITY

May 2015

ABSTRACT

In this thesis, a novel silica nanosphere (SNS) lithography technique has been developed to offer a fast, cost-effective, and large area applicable nano-lithography approach. The SNS can be easily deposited with a simple spin-coating process after introducing a N,N-dimethyl-formamide (DMF) solvent which can produce a highly close packed SNS monolayer over large silicon (Si) surface area, since DMF offers greatly improved wetting, capillary and convective forces in addition to slow solvent evaporation rate. Since the period and dimension of the surface pattern can be conveniently changed and controlled by introducing a desired size of SNS, and additional SNS size reduction with dry etching process, using SNS for lithography provides a highly effective nano-lithography approach for periodically arrayed nano-/micro-scale surface patterns with a desired dimension and period. Various Si nanostructures (*i.e.*, nanopillar, nanotip, inverted pyramid, nanohole) are successfully fabricated with the SNS nano-lithography technique by using different etching technique like anisotropic alkaline solution (*i.e.*, KOH) etching, reactive-ion etching (RIE), and metal-assisted chemical etching (MaCE).

In this research, computational optical modeling is also introduced to design the Si nanostructure, specifically nanopillars (NPs) with a desired period and dimension. The optical properties of Si NP are calculated with two different optical modeling techniques, which are the rigorous coupled wave analysis (RCWA) and finite-difference time-domain (FDTD) methods. By using these two different optical modeling techniques, the optical properties of Si NPs with different periods and dimensions have been investigated to design ideal Si NP which can be potentially used for thin c-Si solar cell applications. From the results of the computational and experimental work, it was observed that low

aspect ratio Si NPs fabricated in a periodic hexagonal array can provide highly enhanced light absorption for the target spectral range (600 ~ 1100nm), which is attributed to (1) the effective confinement of resonant scattering within the Si NP and (2) increased high order diffraction of transmitted light providing an extended absorption length. From the research, therefore, it is successfully demonstrated that the nano-fabrication process with SNS lithography can offer enhanced lithographical accuracy to fabricate desired Si nanostructures which can realize enhanced light absorption for thin Si solar cell.

Dedicated to my beloved parents:

Yi-Sik Choi and Young-Sang Yu

ACKNOWLEDGMENTS

During my Ph.D years, I have received support and encouragement from a great number of individuals without whom this dissertation might not have been written and to whom I am greatly indebted.

First of all, I would like to thank Dr. Christiana Honsberg for allowing me to have such a great opportunity as a Ph.D student in Solar Power Lab – Nano & III-V group. Because of her valuable advice and kind encouragement, I have greatly enjoyed my Ph.D years and earned valuable research and life experiences. There is no word to express my deepest gratitude to my advisor, Dr. Christiana Honsberg.

I would also like to give my sincere appreciation to Dr. Terry Alford, co-advisor, who has shown his great support and guidance which have been valuable resources for my research and academic life at ASU.

I would also express my gratitude to Dr. Stephen Goodnick for accepting to be my committee member.

Gratitude is extended to Dr. Clarence Tracy who has been willing to share his valuable knowledge and insight with me. The feedback and assistance that I had from him have been a great strength to overcome the huddle that I faced during my research.

In addition, I would really appreciate Bill Dauksher (SPL Lab Manager) who has kindly provided valuable advices and assistance for my experiments in Solar Power Lab. His help has always made things easier.

I would also like to express my sincere gratitude to Dr. Stuart Bowden who has advised me in many occasions while I study in Solar Power Lab.

Lastly, I would like to give my best thanks to my beloved parents, Yi-Sik Choi and Young-Sang Yu who always show their unconditional love and support throughout my life.

TABLE OF CONTENTS

	Page
LIST OF TABLE.....	x
LIST OF FIGURES.....	xi
CHAPTER	
1. INTRODUCTION	1
1.1. Background of Photovoltaic	1
1.2. Current Status of Photovoltaic.....	3
1.3. Nanostructured Si Solar Cells.....	7
1.3.1. Problem of Conventional Approach and Goal of Nanostructured Si Solar Cell	7
1.3.2. Current Status: Summary of Nano-lithography Techniques.....	9
1.3.3. Current Status: Summary of Nano-fabrication Techniques.....	12
1.4. Aim of This Work.....	15
2. NANO-LITHOGRAPHY & NANO-FABRICATION	16
2.1. Deposition of 2-Dimensional Silica Nanosphere (SNS)	16
2.1.1. Motivation and Background.....	16
2.1.2. Experimental Section.....	18
2.1.3. SNS Dispersibility in Solution.....	19
2.1.4. SNS Solution Wettability on Silicon Surface.....	21
2.1.5. Capillary Force for Short-range SNS Assembly.....	24
2.1.6. Convective Force for Long-range SNS Assembly	27

CHAPTER	Page
2.1.7. Large-scale Area SNS Monolayer Spin-coating.....	29
2.1.8. Spin-coating of SNS with Various Diameters: Diameter vs. SNS Solution Concentration	34
2.1.9. DMF vs. Other Solvents.....	35
2.1.10. Summary	36
2.2. Surface Nano-patterning.....	38
2.2.1. SNS Size Reduction by Reactive Ion Etching (RIE)	38
2.2.2. SNS Removal after RIE	43
2.3. Fabrication of Si NP with Metal-assisted Chemical Etching (MaCE)	45
2.3.1. Experimental Section	46
2.3.2. SNS Diameter Control with RIE	47
2.3.3. Metal Cathode Layer Deposition for Enhanced Lithographical Accuracy ..	49
2.3.4. Fabrication of Si NP with MaCE Technique.....	51
2.3.5. Summary.....	57
2.4. Fabrication of Si Nano-structures with Different Etching Techniques	59
2.4.1. Inverted Pyramid: KOH Solution Etching	59
2.4.2. Nano-pillar & Nano-tip: RIE.....	61
3. OPTICAL SIMULATION FOR SI NANOPILLAR ARRAY	66
3.1. Background	66
3.1.1. Motivation of This Work.....	66
3.1.2. Rigorous-Coupled Wave-Analysis (RCWA)	68
3.1.3. Finite-Difference Time-Domain (FDTD)	69

CHAPTER	Page
3.2. Design of Si NPs for Enhanced Light Absorption	70
3.2.1. Period of Si NPs	70
3.2.2. Height and Si FF of Si NPs	72
3.2.3. Diffraction Efficiency of Si NPs at Higher Orders (> 0th order)	77
3.2.4. Absorption Enhancement of Si NP Array	81
3.2.5. Summary	83
4. FABRICATION OF SI NPS BASED ON OPTICAL MODELING.....	84
4.1. Demonstration of Simulated Si NPs	84
4.1.1. Fabricated Si NP Vs. Simulated Si NP	84
4.1.2. Si NP Vs. Conventional KOH Pyramid	90
4.1.3. Summary	91
5. ORGANIC PASSIVATION FOR SI SURFACE	92
5.1. Understanding of Molecular Contribution for Effective Quinhydrone/Methanol Organic Passivation for Silicon.....	92
5.1.1. Fundamental of Recombination Process	92
5.1.2. Surface Passivation Approaches	99
5.1.3. Motivation of This Work	99
5.1.4. Experimental Section	101
5.1.5. Minority Carrier Lifetime	102
5.1.6. Uniformity of Organic Passivation Layer	103
5.1.7. Understanding of Molecular Reaction for Passivation	106
5.1.8. Carrier Lifetime Vs. Passivation Time in Solution	109

CHAPTER	Page
5.1.9. Kelvin Probe Measurement: Si Surface Band-Bending	110
5.1.10. Summary	114
6. CONCLUSION AND PROPOSED FUTURE WORK	115
6.1. Conclusion	115
6.2. Proposed Future Work	116
REFERENCES	118
APPENDIX	
A.1. LIMIT OF ABSORPTION ENHANCEMENT IN THIN-FILM WITH GRATING STRUCTURE FABRICATED IN SUBWAVELENGTH -SCALE PERIOD	130
A.2. STATISTICAL COUPLED-MODE THEORY	130
A.3. OVERVIEW OF THE THEORY	135
A.4. UPPER LIMIT OF ABSORPTION ENHANCEMENT IN 2-D GRATING.....	138
A.1-4. EFFECT OF PERIODIC LATTICE STRUCTURE	139

LIST OF TABLES

Table	Page
1.1. Performance of Commercial PV Technologies (Data from EPIA, 2011) [11].....	5
2.1. Comparison of CHF ₃ / Ar Gas RIE Etching Profile for 10-min Etching on SS Deposited Si Surface Which Were Performed under Three Different Chamber Pressures.....	39
5.1. N-type Si - SPV Values (Induced Charge at Si Surface) Measured by Kelvin Probe, and τ_{eff} & Implied V_{oc} Measured by Photoconductivity Decay with Various Surface Treatments & Passivation (or Dipping) Time.....	111

LIST OF FIGURES

Figure	Page
1.1. Historical and Projected World Energy Supply and Demand. [5].....	2
1.2. Average Solar Irradiance Map of the World	3
1.3. Total World Energy Consumption by Sources (2010)	4
1.4. Pie Chart of Capacity Percentage of Different Type of PVs. [12].....	6
1.5. The Absorption Length of Crystalline Silicon Juxtaposed Against the Am1.5G Solar Irradiance. The Blue, Green, and Red Colored Regions Indicate the Region with the Highest Optical Absorption, the Region with the Highest Solar Irradiance, and the Region with Absorptions Lengths in Excess of 100 μ m, Respectively.[17].....	7
1.6. (a) Schematic Illustration of E-beam Generation (Left),[26] and Overall Patterning Process in 6 Steps (Right),[27] (b) Mechanism of Laser (or Multi- beam) Interference Lithography Technique (Left), and Possible Patterns with Different Combination of Lasers (Right). [25].....	10
1.7. Schematic Illustration of (a) Nano-imprint Lithography,[29] (B) Nanosphere Lithography Processes. [28]	11
1.8. Schematic Illustration of Various Nano-fabrication Method; (a) CVD, (b) RIE, (c) ECE, and (d) MaCE.[35-38]	13
1.9. SEM Images of Si Nanowire (or Nanopillar) by Using (a) CVD,[39] (b) RIE,[40] (c) ECE,[41] and (d) MaCE	14
2.1. The SNS Cluster Effect Producing Non-uniform SNS Distribution Followed by Reduced Coverage.....	21

Figure	Page
2.2. Contact Angle Measurement of (a) Water ($\alpha = 26.9^\circ$), and (b) DMF ($\alpha \approx 0$ or unmeasurable). The Comparison of Wettability with 300ul (50mg/ml) of (c) SNS _{water} , and (d) SNS _{DMF} Solution Droplets on Piranha Cleaned 2-inch Si Substrate, and After-spin-coating Surface Images of (e) SNS _{water} , and (f) SNS _{DMF}	22
2.3. Schematic Illustration of Material Loss of (a) SNS _{water} and (b) SNS _{DMF} during Spinning, and the SEM Images to Compare the Coverages between (c) SNS _{water} and (d) SNS _{DMF} . To Focus on Solvent Influence, 50mg/ml of Low SNS Concentration was Used. Spin-coating Speed is Same for Both.....	23
2.4. Schematic Illustration of Two Spheres Partially Immersed in a Fluid Layer for Capillary Attraction, F_{cap} . [61]	25
2.5. (a) F_{cap} Plotted as a Function of L, and the Actual SEM Images from (b) SNS _{water} , and (c) SNS _{DMF} . (d) and (e) are the Schematic Illustration of Interparticle Distance, L, Depending of Wettability of Solvent, Water and DMF, Respectively. (Note: The F_{cap} Calculation was Made with $\alpha_{water} = 26.9^\circ$, $\alpha_{DMF} \approx 0$ to Determine the Ψ_c , $r_c = 130\text{nm}$ (radius of 2/3 sphere spot), $\gamma_{water} = 73\text{mN/m}$, and $\gamma_{DMF} = 25\text{mN/m}$, respectively.).....	26
2.6. Schematic Illustration of (a) Fast Solvent Evaporation of Water, and (b) Slow Solvent Evaporation of DMF during Spin-coating causing (c) Discontinuous SNS Assembly with Localized F_{cap} , and (d) Continuous SNS Assembly after Expanded F_{cap} , and Actual SEM Images of (e) SNS _{water} , and (f) SNS _{DMF} (50mg/ml of SNS with Same Spin-coating Condition).....	28

Figure	Page
2.7. SEM Images for SNS Coverage from Various Concentration of SNS _{DMF} , which are (a) 50mg/ml, (b)100mg/ml, and (c) 150mg/ml.....	29
2.8. Acceleration Speed Effect for Uniform SNS Assembly Layer Formation; (a) 20rpm/s, (b) 50rpm/s, and (c) 80rpm/s.....	31
2.9. (a) SNS Deposited 2-inch Round Si Surface Image, and the SEM Images with Different Magnifications, (b) 250x, c) 2000x, and (d) 25000x, Respectively.	32
2.10. (a) SNS Deposited 4-inch Round Si Surface Image, SEM Images of (b) Low Magnification, (c) Less SNS Monolayer Coverage Region of Blue Solid-box in (b), and (d) High SNS Monolayer Coverage Region of Red Solid-box in (b).....	33
2.11. Different Size of SNS in (a) 310nm, (b) 600nm, and (c) 840nm Diameters, Spin-coated on 2-inch Si Wafers (Top, Middle, and Bottom of (a) ~ (c) Represent the Whole 2-inch Wafer with Each SNS, ×2k, and ×20k Magnification SEM Images, Respectively.), (d) Optimum SNS Solution Concentration vs. SNS Diameter for Spin-coating and (e) Table Representing the Ratio of SNS Diameter (Dia., nm) to Solution Concentration (Conc', mg/ml) for Spin-coating.....	34
2.12. SEM Images of DMSO Introduced SNS (310nm) Spin-coated Si Surface Which Shows (a) Severely Non-uniform, and (b) Multi-layered SNS Film. (Note: Spin-coating Condition was 80rpm/sec Acceleration and 2000 rpm/sec Maximum Speed for 200-sec).....	36

Figure	Page
2.13. (a) Spin-coated 2-inch Round Si Surface Images and SEM Images of (b) Uniformly Distributed SS and (c) Closely-packed SS Shown in Different SEM Magnifications.....	38
2.14. Schematic Illustration (Top) and SEM Images (Bottom) to Compare the Effect of RIE Chamber Pressures, (a) As-deposited SS, (b) 75mTorr RIE Processed SS (Horizontal Dia. ~800nm, Vertical Dia. ~350nm), and (c) 100 mTorr RIE Processed SS (Horizontal Dia. ~800nm, Vertical Dia. ~260nm).....	40
2.15. (a) ~ (d) SEM Images of RIE Etched SS with Various Etching Times, 10-min, 13-min, 16-min, and 19-min, Respectively, and (e) Diagram of Inter-particle Spacing (d) Versus RIE Etching Time. (Note: RIE Conditions are 75mTorr Chamber Pressure, 200 Watts RF Plasma Power at 25/25sccm Gas Flow Rate) (Scale-bar: 1 um for Top Image, 500nm for Bottom Image).	42
2.16. Schematic Illustration of SNS Lithography Process and UVO Effect to Produce Clean Si Surface Patterning, and (e) Bottom is SEM Image of Non-UVO Treated Sample, and (f) Bottom is UVO Treated Sample. (Green-line Indicates Deposited Cr Layer, and Red-line Indicates C _x F _y Compound Layer on the Surface, Scale-bar = 1 μm).....	45
2.17. Three Different Sizes of SNS in (a) 310nm, (d) 600nm, and (g) 840nm in Diameter, and RIE Etched with Two Different Etch Times. (b), (c) are 1.5-min and 2.5-min on 310nm SNS, (e) and (f) are 4-min and 6-min on 600nm SNS, and (h) and (i) are 6-min and 8-min on 840nm SNS. (j) the SNS Diameter Change vs. RIE Time, and (k) a Table Showing Etch Rates for Each SNS.	48

Figure	Page
2.18. (a) The Etched Si Nanopillar Had Un-expected Structure Damage by Incomplete SNS Removal due to Metal Catalyst Covered on SNS, and (b) Peel-off Au Metal Layer during SNS Removal due to Weak Adhesion of Au on Bare Si Surface.....	50
2.19. (a) Si Surface with SNS Etched to 611nm Average Diameter (840nm period), (b) Cr/Au, (c) Ti/Au, and (d) Ni/Au Deposited Si Surface after SNS Removal Which Have 722nm, 667nm, and 622nm Diameter of Pattern, Respectively.	51
2.20. Scheme of Reaction Processes for Metal-assisted Chemical Etching Based on Galvanic Process. ① The Oxidant (i.e., H ₂ O ₂) is Reduced by the Catalytic Activity of Noble Metal. ② The Generated Holes from Reduction of Oxidant Consequently Diffuse to Si/Metal Interface through Metal Layer. ③ The Oxidation of Si is Occurred by the Injected Holes, and ④ SiO ₂ is Reacted with HF. ⑤ Finally, SiO ₂ is Dissolved and Etched Away into the Solution.[82].....	52
2.21. (a), (d), and (g) are RIE Etched SNS with 840, 600, and 310 nm Initial Diameter. (b), (e), and (h) are Up-side SEM Image, and (c), (f), and (i) are 80 Degree Angled SEM iImages for Si NPs.....	54
2.22. Ni/Au Catalyst Deposited Si Surface with (a) 30%, (b) 50%, and (c) 70% Fractional Coverage, and (d) ~ (f) Si NPs Fabricated from Each Catalyst Fractional Coverage after 5-min Etching in MaCE Solution. (g) Etch Rates from Each Ni/Au Fractional Surface Coverage. (h) ~ (j) ~ 500nm Height of Si NPs from (a) ~ (c) after Dipping in the Etching Solution for 8-min, 6.5-min, and 5-min, Respectively.....	56

Figure	Page
2.23. SEM Images of Fabricated Si NP Array at 3 μm Height in 840nm Period (50% Si FF) to Confirm the Uniformity of the Si NP Array Over the Surface; (a) $\times 35\text{K}$, and (b) $\times 10\text{K}$ Magnifications.....	57
2.24. SEM Images of (a) Cr Deposited Si Surface after SNS Removal, (b) 1% KOH Etched Surface with Cr Layer, (c) Inverted Si Pyramid after Cr Layer Removal, (d) Cross-sectional Image of Inverted Si Pyramid, and (e) Fabricated Inverted Pyramid over Large Surface Area to Show Its Uniformity (Inverted Pyramid Has $\sim 10\%$ Size Variation Likely Caused by an Initial SNS Size Variation of 10%). Note : (a) ~ (d) Scale-bar = 1 μm , and (e) Scale-bar = 10 μm	60
2.25. Schematic Illustration of RIE Process to Etch Solid Surface.[83].....	63
2.26. Schematic Illustration and SEM Images to Fabricate Nanopillar and Various Aspect-ratio Nano-tip Structure.	64
3.1. (a) Shematic Illustration of Simulated Si NP, and (b) Investigated Optical Properties of Si NPs Arrayed in 2-D Hexagonal Formation; (1) Forward Scattering for Reduced Front Surface Reflection Loss, and (2) Light Diffraction Order for Enhanced Light Absorption of Transmitted Light in the Absorber.	68
3.2. Constructed Structure to Solve a Diffraction Problem Using RCWA. (a) Structure Is Divided into Strata so That Each Stratum Is Homogeneous in the Z-direction, and (b) Horizontally Divided Strata so That Each Stratum Is Homogeneous in the y-direction for Circular-shaped Structure Calculation.	68

Figure	Page
3.3. Upper Limit of Absorption Enhancement for a Grating with Hexagonal Lattice Periodic Structure. Reprinted from Reference [98].....	71
3.4. Schematic Illustration of Grating Structured Layer for (a) Statistical Coupled-mode Theory, and for (b) Our Simulation.....	73
3.5. RCWA Results for Front Surface Reflections from Three Different Si FFs, (a) 30%, (b) 50%, and (c) 70% Representing 344, 444, and 520 nm Si NP Diameters, Respectively, and the Height Range Is from 100 to 400nm with 100nm Interval. In Addition, (d) Reflection Trends for Short (300~600nm) and Long (600 ~ 1100nm) λ Are Shown with Different NP Heights in Weighted Reflectance. (Note: Period Is Fixed at 600nm)	74
3.6. Incident Light Scattering Behavior ($\lambda = 900\text{nm}$) with Various Heights; (a) 100nm, (b) 200nm, (c) 300nm, and (d) 400nm at 30% Fixed Si FF	75
3.7. Incident Light Scattering Behavior ($\lambda = 900\text{nm}$) with Various Si FF; (a) 30%, (b) 50%, (c) 70% at 200nm Fixed Height.....	76
3.8. Red-shifting of Front Surface Reflection as (a) FF (or Diameter, at 100nm Height) and (b) Height (at 70% FF) Increases.	77
3.9. Schematic Illustration of Light Loss Mechanisms for Incident Light in Short (Blue Arrow), and Long (Red Arrow) Wavelength Region.....	78
3.10. Optical Simulation for Transmitted Light Orientation with (a) FDTD ($\lambda = 1000\text{nm}$), and (b) RCWA	79
3.11. Schematic Illustration of Grating Effect with Si NP to Produce High Order Transmitted Light Diffraction	79

Figure	Page
3.12. Fraction of High Order ($>0^{\text{th}}$) Transmitted Light Diffraction with (a) 30%, (b) 50%, and (c) 70% Si FF at Various Height from 100nm to 400nm.....	81
3.13. RCWA Results for Reflection of Si NP Fabricated at 30% FF, 200nm Height and 600nm Period and Reference Reflection from Bare Si surface (5 μm Thick Si Substrate). Both Surfaces Have Back Reflector (BR, 200nm in Perfect Mirror Condition) and Front Anti-reflection Layer (AR, 70nm SiN_x).	82
4.1. Fabricated 30% FF Si NPs in 600nm Periodic Hexagonal Array Approximately for (a) 100nm, (b) 200nm, (c) 300nm, and (d) 400nm Heights.....	85
4.2. Measured Reflectance of Si NPs at Different Heights.....	86
4.3. Comparison of Surface Reflection between Computational (RCWA, Dash-line) and Measured (Measured, Solid-line) Reflection for (a) 100nm, (b) 200nm, (c) 300nm, and (d) 400nm Si NP Heights (Measured Si Substrate Thickness = 280 μm and RCWA Simulated Si Substrate Thickness = Semi-infinite).....	87
4.4. Comparison of Measured (Red Solid-triangle) and RCWA Simulated (Blue Solid-diamond) Weighted Reflection Change for (a) Whole Wavelength Range (300 ~ 1100nm), (b) Short (300 ~ 700nm) and (c) Long (700 ~ 1100nm) λ Region with Increasing Si NP Height	88
4.5. Example of Structural Damage on Top of 400nm Si NP in Red-circle.....	89
4.6. Comparison of Surface Reflection between Si NPs (Red Solid-line, 200nm Height, 30% FF, and 600nm Period) and Conventional KOH Solution Etched Random Pyramid (Black Solid-line) Fabricated on 280 μm Si Substrate.	90
5.1. Carrier Recombination Mechanism in Semiconductor System.[103]	94

Figure	Page
5.2. Molecular Structures of (a) BQ, (b)HQ, (c) QHY, (d) SQ (Passivation Agent).....	100
5.3. (a) Measured Minority Carrier Lifetimes (τ_{eff}) of BQ (Solid-square) and HQ (Solid-triangle) Treated Si Compared to an HF (Open-circle) Only Cleaned Sample and (b) the Measured τ_{eff} at a Minority Carrier Density of $2 \times 10^{15} \text{ cm}^{-3}$ with 100% BQ, HQ, and Various HQ Mixture ratios into a Fixed 10mM BQ in MeOH.....	103
5.4. HR-AFM Images of (a) Pure BQ, (b) 5 mM HQ, (c) 10 mM HQ, (c) 15 mM HQ Addition into 10 mM of BQ in MeOH. (Scan-scale : 200 nm x 200 nm & Scale-bar : 50nm)	104
5.5. TUNA Image of (a) 5 mM HQ, (e) 10 mM HQ, (f) 15 mM HQ Addition into 10 mM of BQ in MeOH. (Scan-scale : 200 nm x 200 nm & Scale-bar : 50nm), (Note: It Is Note-worthy that a 1 to 1 Mixture Ratio of BQ and HQ Might also Produce a More Ordered Molecular Stacking of the Passivation Layer since the Higher Current Flow (or Brighter Color) at the Molecular Island Region in Figure.5 (b) Might Indicate That There Is a Well-ordered Pi-Pi Stacking Formation among Molecules Which Improves the conductivity of the Molecular Layer.[114, 127, 128]).....	105
5.6. Schematic Illustration for SQ Formation in Solution to Produce Si-SQ Bonding for Si Surface Passivation.....	107
5.7. (a) FT-IR Results of BQ, HQ, and Various HQ Mixture Ratios into Fixed BQ in MeOH and Pure MeOH, (b) Reducing BQ into One SQ in BQ/MeOH, (c) Two SQ Formation in BHQ/MeOH.....	108

Figure	Page
5.8. Measured τ_{eff} of Si Samples after Dipping in Pure BQ and HQ Added MeOH Solution for 10-min to 180-min.....	109
5.9. HR-AFM Images of Si Surface after Dipping in BHQ [a, b] and BQ Solution [c, d] for 1-hr and 3-hr, Respectively. (scale-bar = 50nm).....	112
5.10. Schematic Illustration of (a) SQ in Mono-layer, and (b) SQ in Aggregation (or Multi-layer) Producing Different Degree of Molecular Dipole Moment.....	113
A1. Light Trapping with Random Texture and a Grating Structure. (A) Light Trapping by Randomly Textured Surface. (B) Light Trapping Using a Periodic Grating on a Back-Reflector (Yellow); $d = 2 \mu\text{m}$, $L = 250 \text{ nm}$. The Depth and Width of the Dielectric Groove in the Grating are 50 and 175 nm, Respectively. The Dielectric Material is Crystalline Silicon. (C) Absorption Spectrum [Transverse Magnetic (TM) Mode, Normal Incidence] and Dispersion Relation of Waveguide Modes for the Structure in B. Resonances Occur When $k_{\parallel} = 2\pi/L$ (Red Dots). Reprinted from Reference [103].....	131
A2. (a) Channels in 2-D k-space for a Grating with the Square Lattice Periodic Structure and (b) its Upper Limit of Absorption Enhancement. Reprinted from Reference [102]	137
A3. (a) Channels in 2-D k-space for a Grating with Hexagonal Lattice Periodic Structure and (b) its Upper Limit of Absorption Enhancement. Reprinted from Reference [102]	139

Chapter. 1

INTRODUCTION

1.1. Background of Photovoltaic

After the discovery of the photovoltaic effect by Becquerel in 1839,[1] numerous scientific and technical successes have been achieved to develop the first silicon solar cells based on a diffused p-n junction at Bell labs in 1954.[2] Since the first foot step of Si solar cell, solar cell industry has been rapidly grown and in 2014, ~ 45 giga watt (GW) capacity of solar panels have been installed around the world.[3] This phenomenal growth of solar industry has been motivated by global warming originated from the excess carbon dioxide emission from traditional fossil fuel based power generation. In addition, the risk of nuclear power which can produce almost irretrievable damage both to human-being and environment make itself less ideal energy resource regardless of its meager chance of accident. Therefore, there is growing interest in developing clean and renewable energy to sustain human life accompanied by preserving our nature.

In addition to drawbacks of traditional power generation methods, recent global population growth and rapid industrialization in 3rd world undeveloped countries have casted a huge question how we will satisfy the exponential demand of energy in the future to sustain our society. The question must be considered very seriously since as shown in Figure 1, the global demand of energy will be exceeded far beyond possible energy supply from traditional fossil fuel based energy generation.[4, 5] This energy shortage has significant implication to the future of our society. For example, in order for

10 billion people to sustain their current level of lifestyle, the world needs at least ten additional terawatts (TWs) which is equivalent to 150 millions of barrels of oil per day until 2050.[6, 7] Furthermore, the energy crisis will be more exacerbated by the concerns about global warming from greenhouse gas emission due to increasing fossil fuel consumption. [8-10] Therefore, developing clean, un-depletable, and less geometrically dependent energy resource is the major and very first challenge of our society to continue the prosperity of human-being in this world.

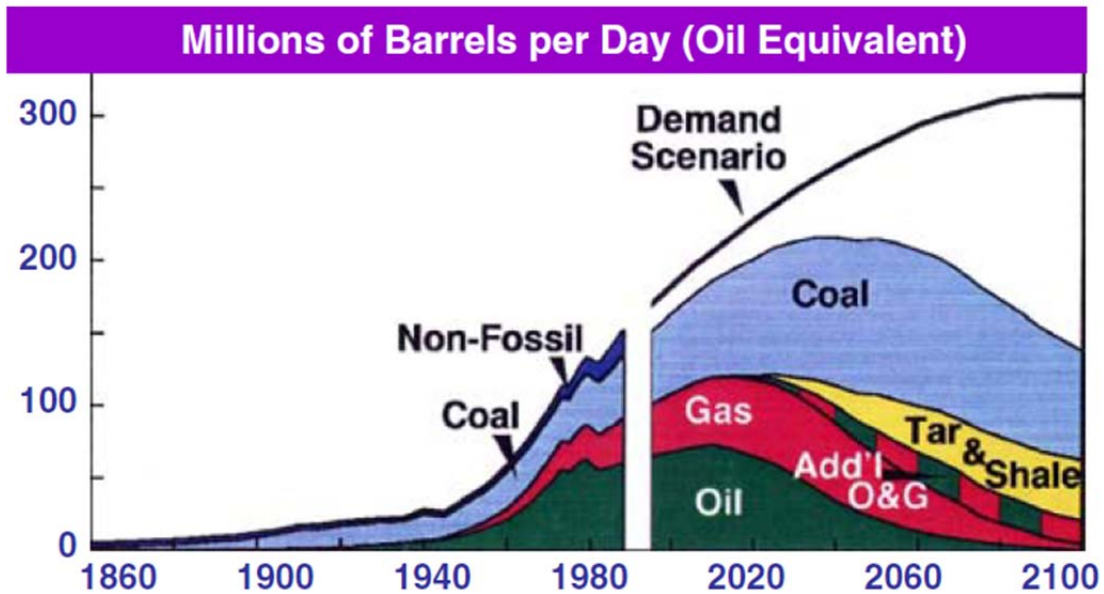


Figure 1.1. Historical and projected world energy supply and demand. [5]

1.2. Current Status of Photovoltaic

In terms of the effort to find new energy resource, recently various kind of clean and renewable energy resources and generation techniques have been developed including biomass, geothermal, wind, and solar energy. However, among these resources, solar energy is considered as the most ideal candidate for future energy resource which can satisfy the conditions as clean, un-depletable, and less geometrically dependent energy source. In Figure 2 for average solar irradiance map of the world clearly shows that the enormity of the distributed solar resource and its highly open accessibility regardless of location. Therefore, solar energy has a huge potential to replace conventional fossil fuel in addition to its safety.

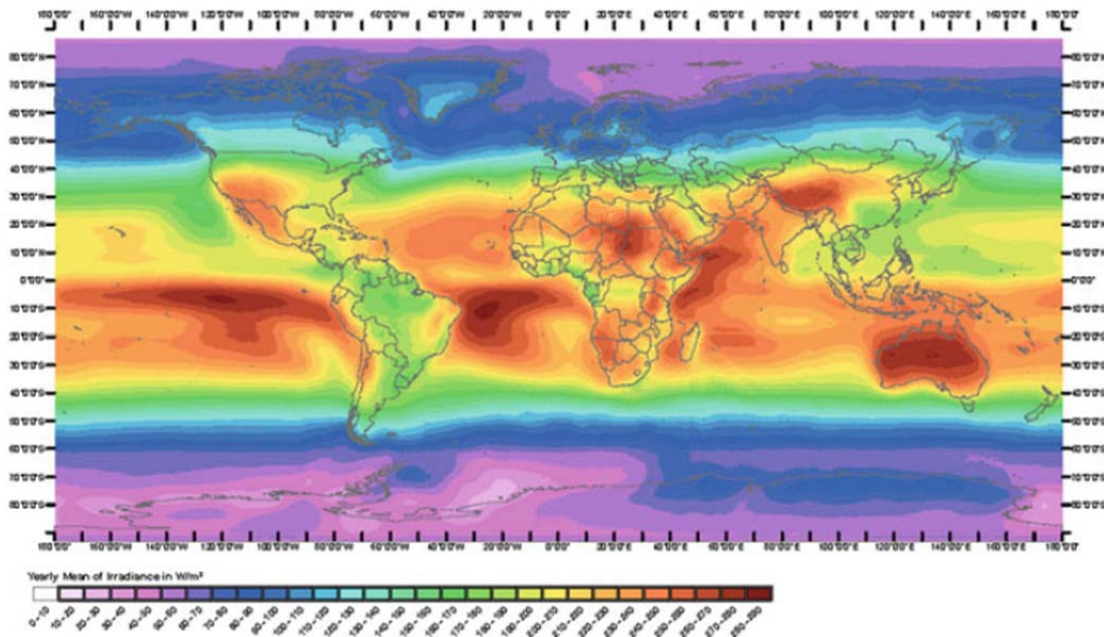


Figure 1.2. Average solar irradiance map of the world. (Copyright Mines Paristech/Armines 2006)

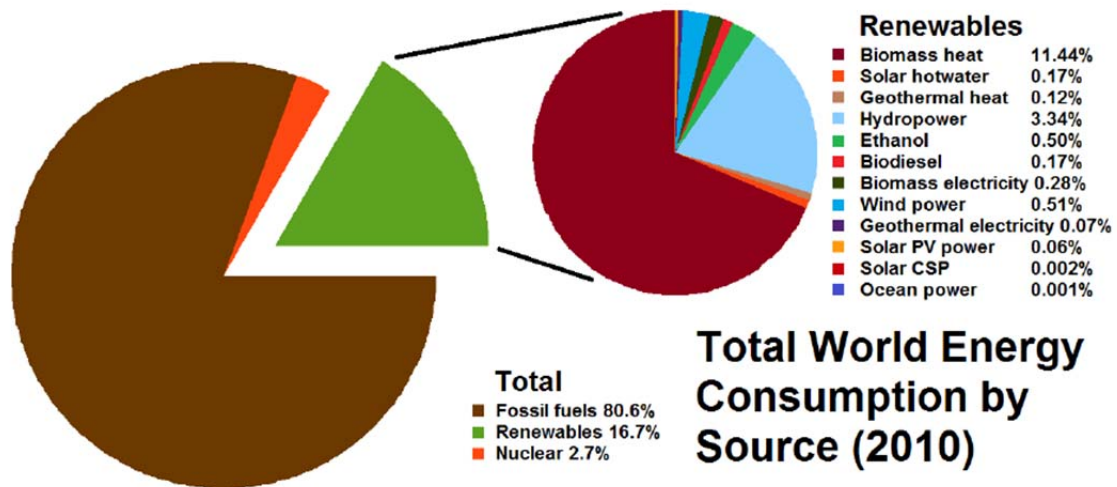


Figure 1.3. Total world energy consumption by sources (2010)

As shown in Figure 3, however, fraction of world energy consumption from solar energy is less than 0.1% among total world energy consumption. In addition, even compared with other renewable energy resources, energy supply from solar is still too meager to be meaningful energy supply source. The major barrier for this very limited energy consumption from solar energy is attributed to the high cost and/or insufficient efficiencies of existing solar cells. Therefore, many of recent PV researches have focused on developing high or reasonable efficiency of solar cells accompanied by economical viability to compete with traditional fossil fuel.

	Cell effic. (%)	Module effic. (%)	Record commercial and (lab) efficiency, (%)	Area/kW (m ² /KW) ^{a)}	Life-time (yr)
c-Si					
Mono-c-Si	16 - 22	13 - 19	22 (24.7)	7	25 (30)
Multi-c-Si	14 -18	11 - 15	20.3	8	25 (30)
TF					
a-Si	4 - 8		7.1 (10.4)	15	25
a-Si/ μ c-Si	7 - 9		10 (13.2)	12	25
CdTe	10 - 11		11.2 (16.5)	10	25
Cl(G)S	7 - 12		12.1 (20.3)	10	25
Org.Dyes	2 - 4		4 (6-12)	10 (15)	na
CPV	na	20 - 25	>40	na	na

a) A module efficiency of 10% corresponds to about 100 W/m²

Table 1.1. Performance of commercial PV technologies (Data from EPIA, 2011) [11]

In Table 1, commercially available solar cells are listed with their performances, [11] and from the Table 1, it is obvious that conventional bulk (or thick) c-Si PV still offers superior performance compared to newly developed PV with different materials which has developed to provide cost-effective PV. This inferior performance of newly developed PV cannot provide sufficient grid parity (i.e. the parity between the PV generation cost for residential and commercial systems and the electricity retail price for householders) due to their poor performance despite the lower mass production cost compared to convention bulk c-Si PV. Furthermore, suitable PV processing technologies must be developed to produce PV from new material with reasonable grid parity. However, unlike c-Si PV which already made tremendous advancement in the

microelectronics, metal contact, and dielectric passivation techniques due to the long history of c-Si PV and its technical compatibility with Si based semiconductor area, the immature technical and infrastructural basement of new PVs is considered as a barrier for their continuous development. Therefore, as shown in Figure 4, conventional bulk c-Si PV is still playing a dominant role in the global PV market.[12]

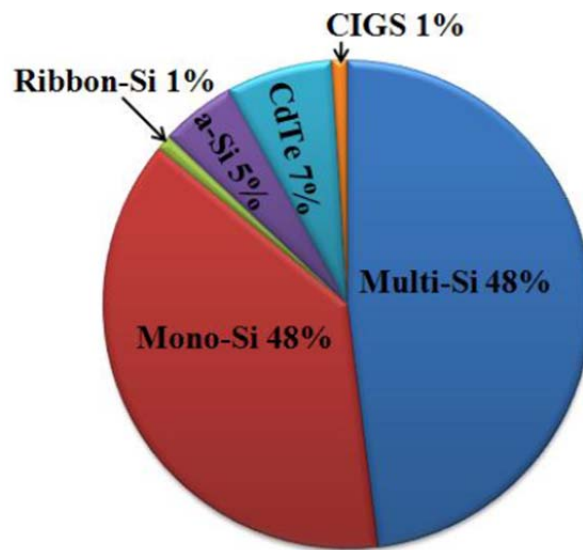


Figure 1.4. Pie chart of capacity percentage of different type of PVs.[12]

However, as discussed previously, despite the numerous advantages of bulk c-Si PV, the high production cost has prevented its wide deployment to replace traditional energy resources. Therefore, milestone innovation must be achieved to improve its efficiency and/or economical viability.[13, 14]

1.3. Nanostructured Thin Si Solar Cells

1.3.1. Problem of conventional approach and goal of nanostructured Si solar cells

To produce a cost-effective, but high efficiency Si PV, there is a growing attention for thin c-Si PV to save material cost which has 20~30% of total module cost.[] In addition, thin Si PV also has a great potential for increased efficiency compared to bulk Si PV since thinner absorber produces less bulk recombination for increased short-circuit current (J_{SC}) and recent state-of-the-art amorphous Si (a-Si) passivation technique has achieved more than 750mV open circuit voltage (V_{OC}) with thinner Si wafer.[15, 16]

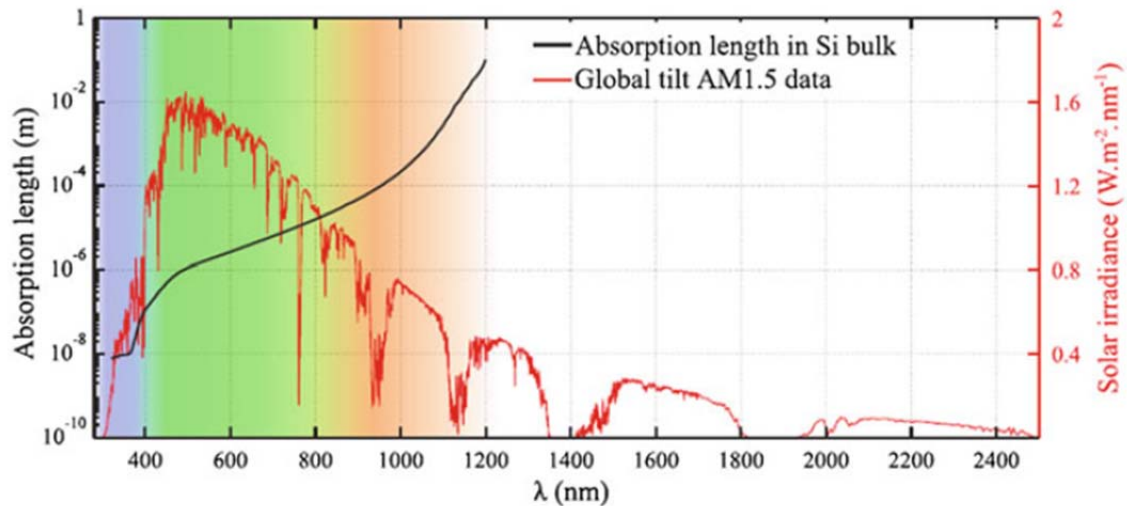


Figure 1.5. The absorption length of crystalline silicon juxtaposed against the AM1.5G solar irradiance. The blue, green, and red colored regions indicate the region with the highest optical absorption, the region with the highest solar irradiance, and the region with absorptions lengths in excess of $100\mu m$, respectively.[17]

Reduction in absorber thickness for commercial Si solar cells requires multiple elements to come together, including thin wafers; good surface passivation; low temperature processing; and a high degree of light absorption. Among these elements, particularly, demonstration of high degree of light absorption with thin Si wafer has been one of major concerns in the field due to the material limit of Si conveying low absorption coefficient at longer wavelength region which requires significantly increased light absorption length as shown in Figure 5. However, the thin Si wafer only provides a short optical length; in a consequence, large fraction of light loss, especially from longer wavelength region, will be expected. Therefore, special surface architecture must be introduced to increase optical length of physically thin Si absorber.

In general, surface texturing is the most widely used approach to increase light absorption of Si solar cells which can provide significantly reduced surface light reflection. The most well-known method for c-Si texturing is anisotropic etching in alkaline solution such as KOH to texture the surface with randomly arrayed pyramids having dimensions in the range of several microns.[18] However, this conventional pyramid structure is not ideal for thin Si solar cell application due to its large material loss during etching process in addition to its insufficient optical property.

Nano-scaled Si surface texturing, therefore, has been widely studied to replace conventional large-scaled pyramid structure due to its reduced material loss from etching process in addition to its highly enhanced AR effect and light absorption.[19, 20] However, regardless of the great potential of Si nanostructures, their excess close-packing and high aspect-ratio have been considered as main barriers to produce high efficiency nanostructured Si solar cell. This is because its complicated surface geometry

is highly challenging for effective surface passivation [21-23] and intimate electrode contact [6] which produce large surface defect density and poor photo-generated carrier extraction, respectively. In a consequence, poor performance of fabricated device is unavoidable. Therefore, well-designed Si nanostructure must be presented which can offer not only enhanced optical path length within thin Si absorber, but also high level of process compatibility for high performance device fabrication.

1.3.2. Current Status: Summary of Nano-lithography techniques

Prior to fabrication of nanostructure on Si surface, highly well-defined surface patterning in nano-scale must be introduced to determine the period, dimension and/or shape of nanostructures since the structural optical properties can be varied depending on physical conditions of fabricated nanostructure. For surface patterning, optical lithographic techniques are the major conventional lithographic approach which create pattern through the use of photons or electrons to modify the chemical and physical properties of the resist. However, nano-fabrication with photo-resist based lithography has limited resolution due to diffractive effects.[24] Since a large number of research groups are working on nanostructure to utilize diverse electrical, physical, and optical advantages of nano-scaled structure, electron beam lithography (Figure 6 (a)) and laser interference technique (Figure 6(b)) have been widely developed to fabricate nanostructures in a desired physical dimension due to their high lithographical resolution for 1-D or 2-D structure in periodic or aperiodic array.[25] These techniques, however, are

not adequate for wide application due to their time-consuming, expensive, and small area restricted processes.

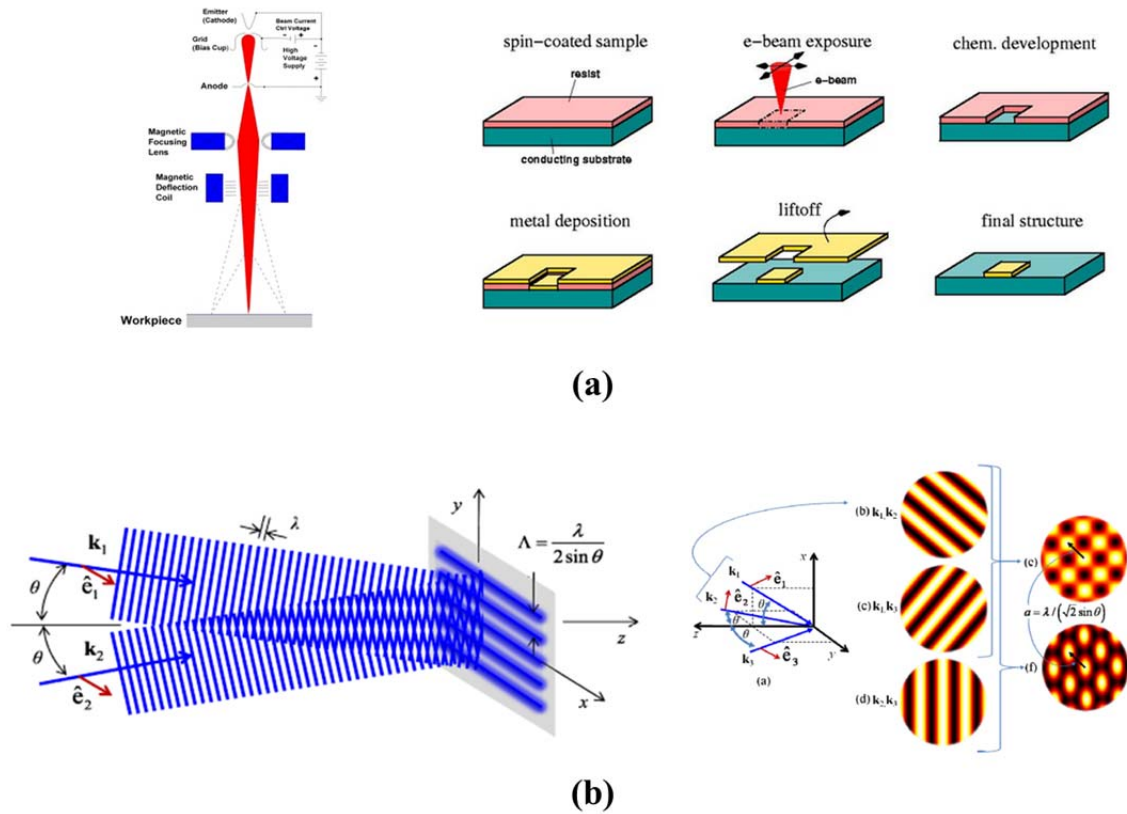


Figure 1.6. (a) Schematic illustration of e-beam generation (left),[26] and overall patterning process in 6 steps (right),[27] (b) mechanism of laser (or multi-beam) interference lithography technique (left), and possible patterns with different combination of lasers (right).[25]

Because of these barriers from conventional nano-lithography processes, a lot of researches are ongoing to find a cost-effective, less time-consuming and large area nano-lithography process that provides acceptable lithographical accuracy and reproducibility. As a part of this effort, currently various novel nano-lithography and fabrication techniques have been developed and investigated for their wide application. Nano-imprint lithography technique, Figure 7(A), is one of those and it has been proven its

great potential as a highly accurate nano-lithography approach which also offers enhanced capability for large-area application.[28-30] However, regardless of the great potential of nano-imprint lithography technique, it still requires conventional nano-lithography processes including electron beam,[31] and laser interference lithography[32] techniques to fabricate a master mold to produce secondary mold for nano-imprinting process. Nanosphere lithography (NSL), Figure 7(B), approach, therefore, has been widely studied since NSL can produce directly nano-patterned surface using nanosphere as a mask layer for etching, but also the patterned surface can be used as a master mold for nano-imprinting application.[33] Furthermore, NSL provides convenient control of the lithographical scale just by introducing different sizes of nanospheres to fabricate intended scales and shapes of nanostructure on the surface by using proper etching techniques.

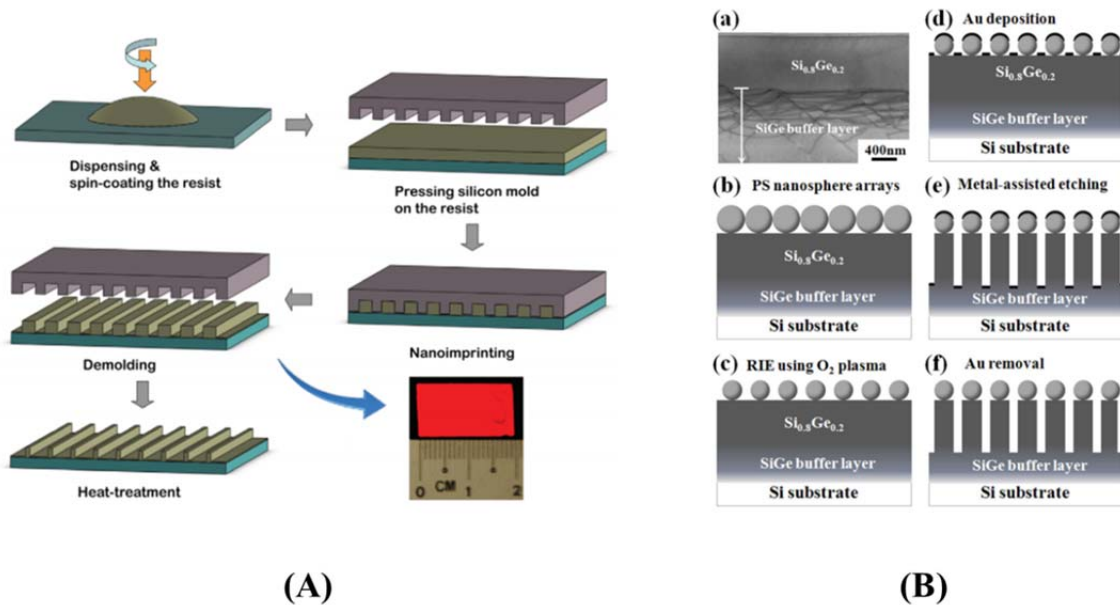


Figure 1.7. Schematic illustration of (A) nano-imprint lithography,[28] (B) nanosphere lithography processes. [34]

In our research, therefore, we have introduced and developed nanosphere lithography (NSL) technique rather than nano-imprint process because of its wider applications.

1.3.3. Current status: Summary of Nano-fabrication techniques

In addition to nano-lithography methods, nano-fabrication process is also highly crucial to produce nanostructure in an intended physical dimension without any change for fabricated nanostructure. Fortunately, due to the key role of Si material in modern semiconductor area and the immense potential of Si nanostructure for various applications, enormous developments in nanotechnology have been made in the past decades and wide range of Si nanostructures from 0-D to 3-D have been demonstrated, such as nanocrystals,[35] nanowire (or nanopillar),[36] nanotube,[37] and porous Si.[38, 39]

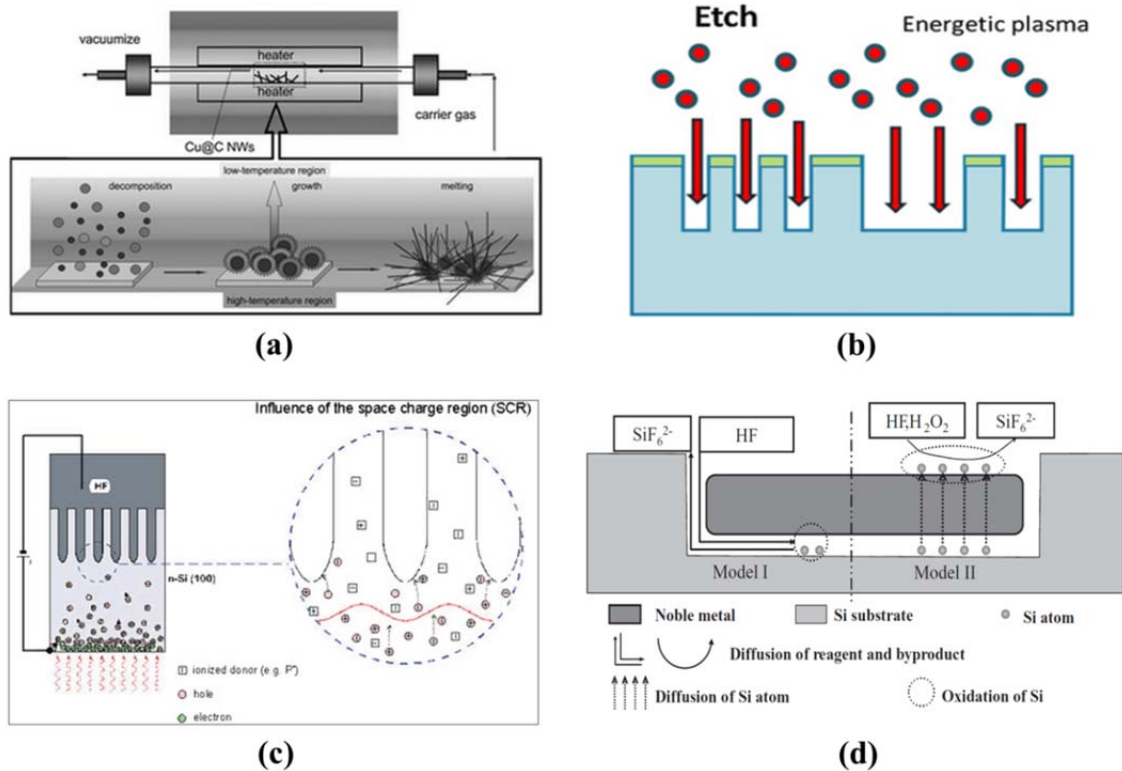


Figure 1.8. Schematic illustration of various nano-fabrication method; (a) CVD, (b) RIE, (c) ECE, and (d) MaCE.[40-43]

Modern nano-fabrication methods can be roughly divided into two categories which are (1) bottom-up and (2) top-down structure fabrication methods. The bottom-up method basically introduces seed materials (or growth catalyst) on the Si surface to facilitate the growth of nanostructure. In case of top-down method, it is relatively straight-forward compared to bottom-up method since nanostructures can be prepared through dimensional reduction of bulk Si by introducing proper etching techniques which determine the shape of fabricated nanostructure. In Figure 8, examples of currently available nano-fabrication methods are presented with their rough etching mechanism

including chemical vapor deposition (CVD),[43] reactive-ion etching (RIE),[42] electrochemical etching (ECE),[41] and metal-assisted chemical etching (MaCE).[40]

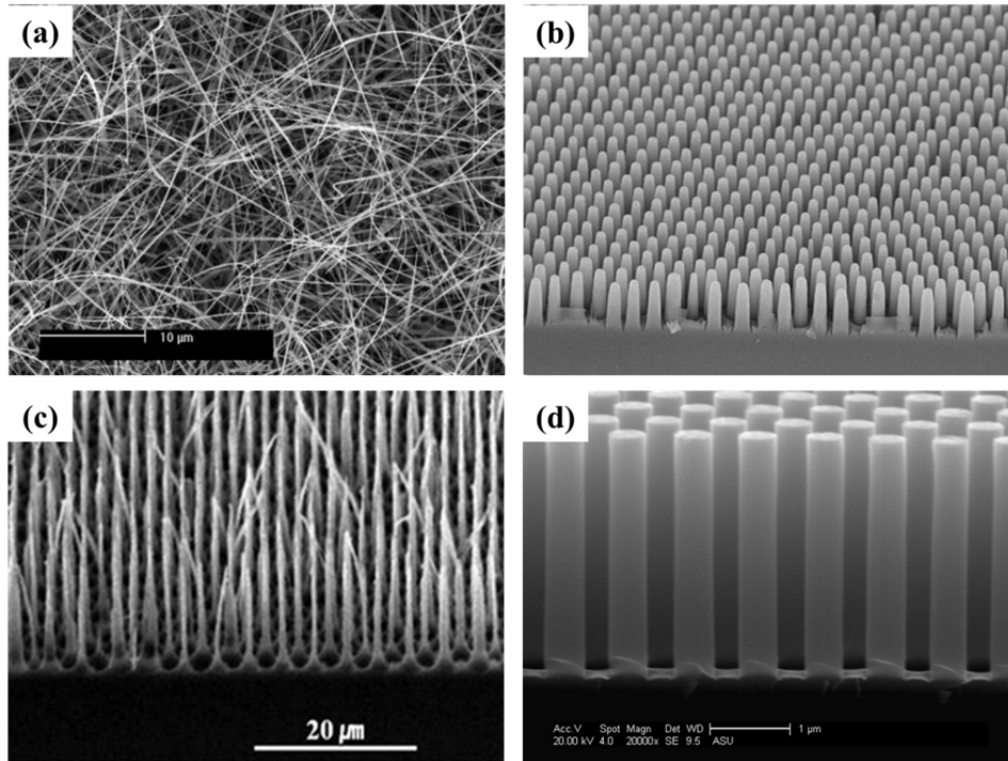


Figure 1.9. SEM images of Si nanowire (or nanopillar) by using (a) CVD,[44] (b) RIE,[45] (c) ECE,[46] and (d) MaCE.

In Figure 9, four different Si nanowire (or nanopillar) are shown which fabricated by different nano-fabrication techniques mentioned previously. Each SEM images well represent the overall nano-fabrication nature of each technique. Specifically, in our research, we have chosen MaCE process to fabricate Si nanopillar (Si NP) and this is because (1) CVD process is highly challenging to control the dimension and orientation of structure in addition to its high-cost, (2) RIE process produces certain amount of

under-cutting of structure during etching which causes unexpected physical dimension change, and (3) ECE process is highly challenging to control the etching rate for desired nanostructure fabrication. On the other hand, MaCE can offer a fast and low-cost etching process that also achieves effective vertical etching with minimal size variation of the NPs from top to bottom.

1.4. Aim of This Work

The aim of this dissertation is to develop fast, cost-effective nano-fabrication process which can produce highly accurate Si nanostructure in a desired period and physical dimension. Via our nano-fabrication approach, we have fabricated various nanostructures including Si nanopillar, nanotip, nanohole and inverted pyramid. Especially, we have investigated the optical property change of Si nanopillar depending on the structural dimension. In particular, (1) grating effect of periodic Si NP array will be computationally studied by using rigorous coupled wave analysis technique and (2) scattering behavior of Si NP will be also investigated with finite-difference time-domain (FDTD) method. From the computational work, we will fabricate the Si NP to compare the results from experimental and computational works to find ideal Si NP dimension which can provide not only enhanced optical property for thin Si solar cell application, but also potentially high compatibility with actual device fabrication process.

Chapter. 2

NANO-LITHOGRAPHY & NANO-FABRICATION

2.1. Deposition of 2-Dimensional Silica Nanosphere (SNS)

2.1.1. Motivation and Background

High uniformity and large area substrate coverage are fundamental requirements for self-assembled colloidal particle monolayer deposition processes to be used in nanosphere lithography.[47-49] A variety of techniques have been explored to produce uniform colloidal particle monolayer assembly, including Langmuir-Blodgett deposition,[50, 51] convective self-assembly,[52, 53] and dip-coating.[54] Even though these techniques have successfully provided close-packed colloidal particle monolayers with high uniformity, substrate area limitations and slow processing are barriers for their wider scale use.

Because of these issues, spin-coating methods have been developed to offer fast and inexpensive large-area colloidal particle monolayer assembly.[55] However, the poor silicon surface wettability or fast evaporation rate during spin-coating of the commonly chosen solvents (*e.g.* water) have made the spin-coating process challenging.[49, 55] Therefore, there is a clear need for well-designed material preparation and an improved spin-coating process that leads to a well close-packed colloidal particle monolayer assembly with high coverage.

Previous reports have addressed these conventional solvent issues in several ways. In one approach, additional surfactant mixtures were added to induce improved solution wettability and colloidal particle dispersion in solution in addition to delayed evaporation rate.[56, 57] However, many surfactant approaches are restricted to low density polystyrene spheres (PS $\sim 1.0 \text{ g/cm}^3$) where it is relatively easy to produce a direct effect by adding small amount of surfactant.[49, 57] For example, Triton-X is a widely used surfactant for improved interparticle interaction and delayed evaporation rate of methanol based PS solutions and is typically mixed in a 1 : 400 ratio for enhanced quality PS spin-coated films.[57, 58] This surfactant approach is very challenging for the high density silica spheres dispersed in water which has a high surface tension at the liquid/solid interface as shown in Figure 3(a). A relatively large amount of the highly viscous Triton-X is required which makes it more difficult to produce a uniform monolayer of silica spheres even with a delayed solvent evaporation rate. Other than Triton-X, ethylene glycol (EG) is reported as a surfactant and the spin coating of colloidal silica films on 1-inch square glass substrates was demonstrated.[56] However, the high viscosity of EG (16.9 cP at 25°C, water = 1.0 cP) causes the same issues as Triton-X. Therefore, it is challenging to find the right surfactant and its optimal mixture ratio for silica sphere spin-coating. Takashi *et.al.* have introduced a no-surfactant spin-coating method; however, this method requires additional control of the humidity and temperature during spin-coating in order to slow the solvent evaporation rate and resulted in only 72% average SNS coverage on a 2-inch round surface area.[55] Additionally Jiang *et.al.*, reported a no-surfactant spin-coating method to create non-close-packed SNS arrays but it requires a surface polymerization process for improved wetting.[59]

We introduce the use of the organic solvent, N,N-dimethyl-formamide (DMF) for silica nanosphere (SNS) monolayer spin-coating on Si surfaces which shows great potential for high-throughput spin-coating processing. We show that the DMF can replace the conventional solvents, and provide enhanced uniformity and coverage of a close-packed SNS monolayer on large surface areas (> 2-inch round Si surface) even under ambient laboratory spin-coating conditions. The quality of SNS assembled monolayers and the coverage after spin-coating with the DMF solvent are compared to films made with the most widely using solvent, water.

2.1.2. Experimental Section

Both the experimental DMF and control water solvent solutions were prepared in the laboratory and spin coated on identical substrates. The SNS solution was prepared with a powder of 310nm diameter silica nanospheres (Bang Lab.) which were dissolved either in the solvent, DMF (Sigma-Aldrich) or de-ionized water (DI-water). The solutions were sonicated for 5 hours to produce complete dispersion of SNS in the solution. 2-inch and 4-inch round polished n-type Si (100) substrates (280 μ m and 460 μ m thickness, respectively) were cleaned in a piranha solution [H₂SO₄ (96%):H₂O₂ (30%) = 4:1] for 15-min to form a hydrophilic Si surface followed by 10-min DI-water rinse.

SNS solution and its monolayer were evaluated with various characterization techniques. The SNS dispersion for each solvent was characterized by measuring absorbance using a UV-VIS spectrophotometer. The SNS spin-coated samples were

observed by scanning electron microscopy (SEM, JEOL XL-30), and the coverage of the SNS monolayer was calculated by the direct counting of the SNS covered area on the Si surface through image analysis software, “image J” (National Institutes of Health, USA)¹⁸, which has been widely used for particle related surface analysis.^{13, 19-23} The wettability of solvent on a Si wafer was determined by measuring the contact angle with an EasyDrop contact angle measurement system (KRUSS).

2.1.3. SNS Dispersibility in Solution.

Prior to SNS spin-coating, the SNS must be well-dispersed in the solution to avoid aggregated SNS deposition on the surface. In Figure 2.1(a), we show the normalized absorbance of 0.5wt% 310nm SNS in DMF and water and compare to the calculated absorbance based on the extinction cross-sections of isolated SNS in each solvent. Mie theory was used to fit the experimental results and to compare SNS dispersibility.^[60] The data shows that DMF produces a high level of SNS dispersibility in the solution since the experimental absorbance behavior of SNS_{DMF} (DMF_{UV-VIS}, red solid-line) has a well-matched trend with its calculated absorbance (DMF_{Calc.}, red dash-line), indicating SNS_{DMF} was in nearly complete dispersion. For SNS in water (SNS_{water}), however, the experimental absorbance (WATER_{UV-VIS}, black solid-line) is substantially broadened compared to the calculated absorbance (WATER_{Calc.}, black dashed-line), which suggests that larger than 310nm SNS exist in the water and therefore supports the fact of clustering of SNS_{water}.

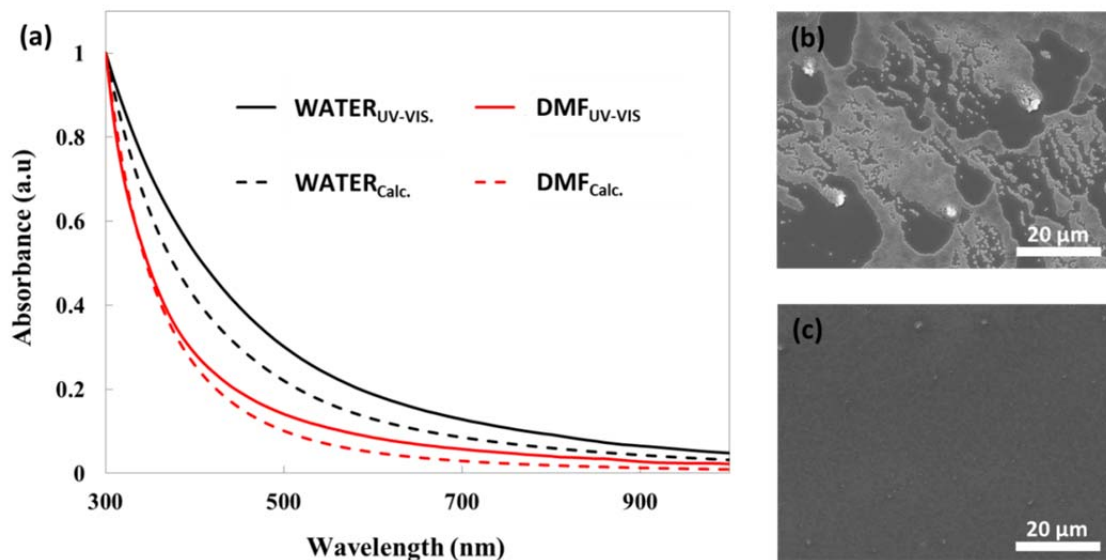


Figure.2. 1. SNS dispersibility comparison between DMF and water; (a) absorbance (a.u.) plotted by UV-VIS spectrophotometer measurement (UV-VIS), and calculation (Calc.) of a single 310nm SNS in each solvent. SEM images of (b), and (c) shows SEM images of the SNS assembled surfaces with SNS_{DMF}, and SNS_{water}, respectively.

Figure 2.1 (b) and (c) are SEM images of the spin coated films on silicon with the water and DMF solvent solutions, respectively. Consistent with the absorbance data, there are no noticeable SNS clusters observed on SNS_{DMF} based films shown in Figure 2.1(c), in contrast to that of SNS_{water}, Figure 2.1(b). The existence of SNS clusters in the solution is especially problematic during spin-coating since they produce anchored SNS clusters in the middle of the surface consequently acting as a barrier for subsequent SNS to be distributed beyond that cluster. As shown in Figure 2.2, the non-dispersed SNS cluster in the solution produces a large SNS-free area that follows the radial direction of the substrate and significantly affects the coverage of SNS after spin-coating. Therefore, a high level of SNS dispersibility in solution must be achieved in advance to produce good uniformity and coverage of an SNS assembled monolayer with spin-coating.

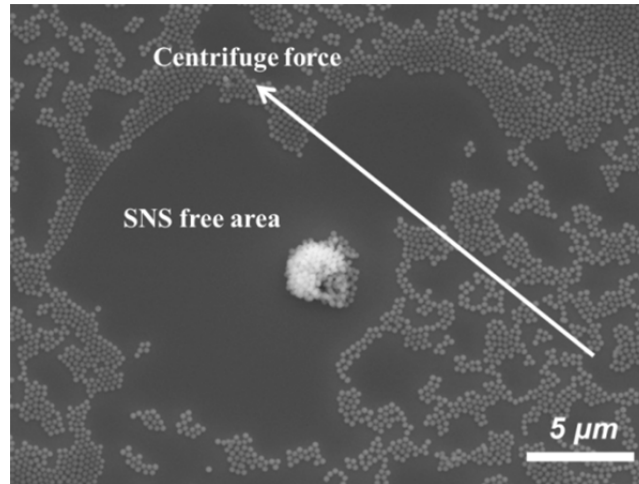


Figure 2.1. The SNS cluster effect producing non-uniform SNS distribution followed by reduced coverage.

2.1.4. SNS Solution Wettability on Silicon Surface.

The contact angles (α) of DMF and water on the Si surface which has a thin hydrophilic wet-oxide formed by piranha cleaning were measured to compare the degree of wettability of each solvent. From Figure 2.3 (a) and (b), it is clear that DMF offers an outstanding wettability ($\alpha_{\text{DMF}} \approx 0$, un-measurable) when compared to water ($\alpha_{\text{water}} = 26.9^\circ$) on the piranha-cleaned Si surface. The importance of solvent wettability has been mentioned in early reports, and those show that wetting of solvent is a crucial factor to obtain uniform colloidal particle monolayer coverage.[49] This is because the high wettability of solvent can provide fast, uniform, and omnidirectional solution spread-out during spinning (or even before spinning) due to its low surface tension (γ) at the liquid/solid interface. For a direct wettability comparison, 300 μl of 100mg/ml SNS_{water} and SNS_{DMF} solutions were dispensed on piranha cleaned 2-inch round Si wafers. From

Figure 2.3 (c), and (d), the SNS_{DMF} solution revealed a complete wetting layer; in contrast, the same volume of SNS_{water} solution produced only a partially covered surface due to its poor wettability.

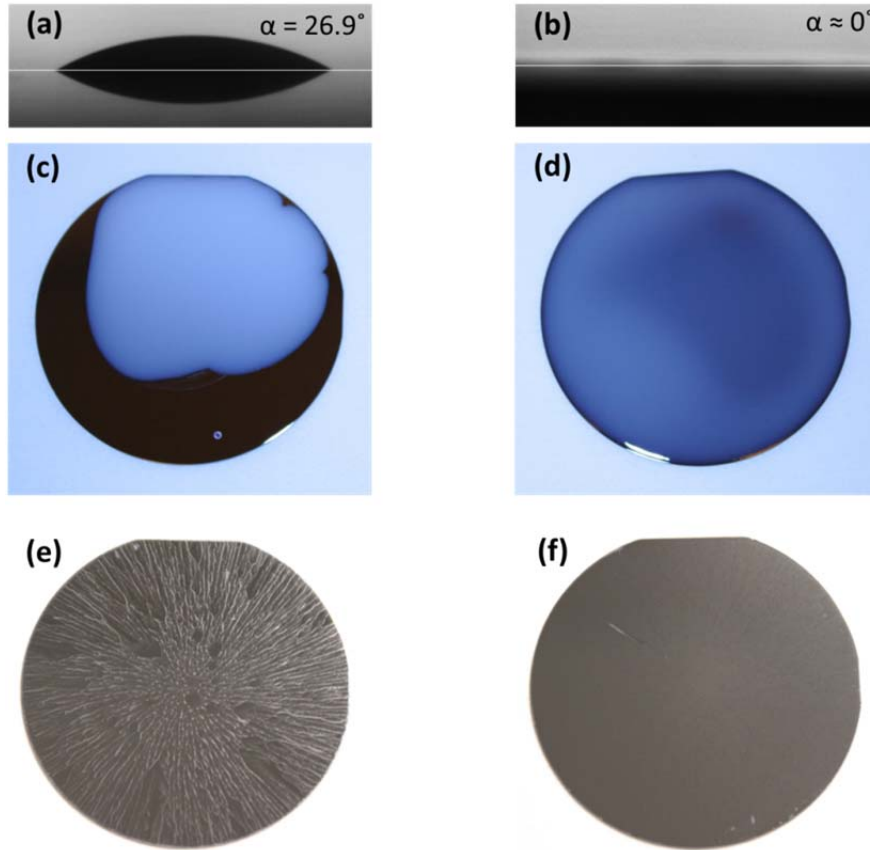


Figure 2.2. Contact angle measurement of (a) water ($\alpha = 26.9^\circ$), and (b) DMF ($\alpha \approx 0$ or un-measurable). The comparison of wettability with 300ul (50mg/ml) of (c) SNS_{water}, and (d) SNS_{DMF} solution droplets on piranha cleaned 2-inch Si substrate, and after-spin-coating surface images of (e) SNS_{water}, and (f) SNS_{DMF}.

In Figure 2.3 (e) and (f), we compare wafer images after spin-coating of the SNS_{DMF} and SNS_{water} solutions to observe the influence of wettability on quality of assembled SNS layers. These images demonstrate that DMF can produce a highly

uniform SNS assembled layer from center to edge, while using water as a solvent gives rise to a non-uniform layer. This significantly improved uniformity can be explained by the low γ of DMF ($\gamma_{\text{DMF}} = 25\text{mN/m}$) compared to that of water ($\gamma_{\text{water}} = 73\text{mN/m}$). A high γ solvent (e.g., water) requires higher centrifugal force (or high spin speed) for solution distribution, but as the spin speed increases, there is a faster solvent evaporation rate which prevents the SNS from uniform distribution (lack of lubricant) and assembly (lack of media between the SNS).

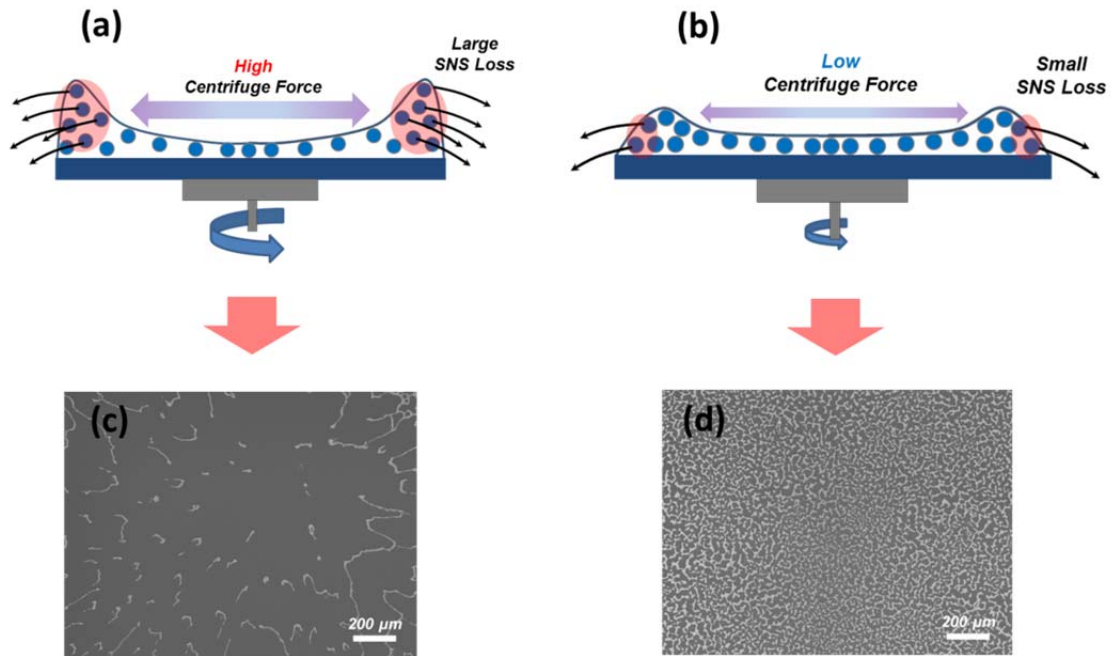


Figure 2.3. Schematic illustration of material loss of (a) SNS_{water} and (b) SNS_{DMF} during spinning, and the SEM images to compare the coverages between (c) SNS_{water} and (d) SNS_{DMF}. To focus on solvent influence, 50mg/ml of low SNS concentration was used. Spin-coating speed is same for both.

In addition to impacting uniformity, γ is also crucial to determine SNS coverage on the surface. This is because the lower γ solvent enables a slower spin speed for SNS

distribution which reduces the SNS loss at the substrate perimeter. High γ and therefore high spin speed inevitably produces a large loss of SNS due to the strong centrifugal force as schematically illustrated in Figure 2.4 (a). The resulting effect is shown in the SEM images in Figure 2.4 (c) and (d), where SNS_{DMF}, Figure 2.4 (c), reveals noticeable coverage improvement when compared to SNS_{water} as shown in Figure 2.4 (d). (Note: the SEM images were taken from exact center of each sample to exclude possible secondary SNS delivery during solution spreading.) Therefore, the excellent wettability (or low γ) of DMF offers both improved uniformity of the SNS assembled layer and enhanced coverage. (Note: 50mg/ml of low SNS concentration was used to focus on solvent influence.)

2.1.5. Capillary Force for Short-Range SNS Assembly

To produce a highly close-packed SNS assembled monolayer with spin-coating, the capillary force (F_{cap}) between the nanospheres must be considered. This is because F_{cap} is mainly the force occurring between each single SNS; therefore, the SNS packing in a short range assembly (or capillary assembly) is directly affected by the degree of F_{cap} which can be calculated by Eq. (1) below;

$$F_{cap} = 2\pi\gamma r_c^2 (\sin^2 \Psi_c) (1/L) \quad (1)$$

where, as illustrated in Figure 2.5, γ is the surface tension of the liquid, r_c is the radius of the three-phase contact line at the particle surface, Ψ_c is the mean meniscus slope angle at the contact line, and L is the interparticle distance (the distance between the centers of the particles).

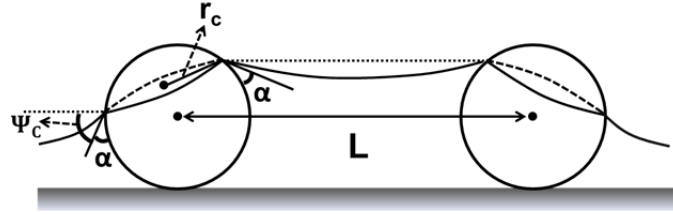


Figure 2.4. Schematic illustration of two spheres partially immersed in a fluid layer for capillary attraction, F_{cap} . [61]

Based on Eq. (1), we have calculated and plotted the F_{cap} of the SNS in DMF and water, respectively, and the results are shown in Figure 2.6. From the diagram in Figure 2.6 (a), the F_{cap} of DMF never exceeds that of water at the same interparticle distance, L , since γ_{DMF} (25mN/m) is significantly lower than γ_{water} (73mN/m). However, the SEM images of Figure 2.6 (b) and (c) show that after spin coating both solutions provide a highly close-packed SNS assembled layer. A reason for this effect may be because the enhanced wetting of the SNS_{DMF} solution results in a higher density of SNS located near the surface than that of SNS_{water} , reducing L as schematically illustrated in Figure 2.6 (d) and (e). We counted the SNS covered areas from SNS_{DMF} and SNS_{water} for the same surface area and the results showed that despite the significantly low γ_{DMF} compared to γ_{water} , SNS_{DMF} provides $\sim 97\%$ of SNS packing to that of SNS_{water} which proves that DMF provides a comparable F_{cap} to that of water to produce a highly close-packed SNS assembled monolayer after spin-coating.

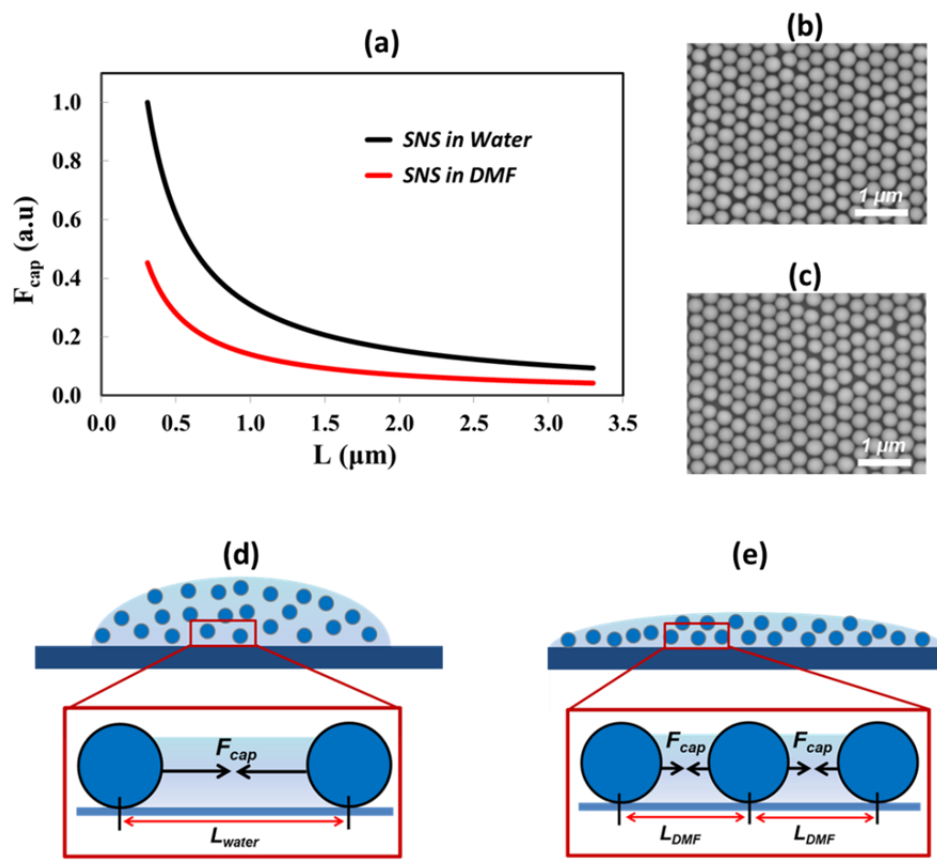


Figure 2.5. (a) F_{cap} plotted as a function of L , and the actual SEM images from (b) SNS_{water}, and (c) SNS_{DMF}. (d) and (e) are the schematic illustration of interparticle distance, L , depending of wettability of solvent, water and DMF, respectively. (Note: The F_{cap} calculation was made with $\alpha_{water} = 26.9^\circ$, $\alpha_{DMF} \approx 0$ to determine the Ψ_c , $r_c = 130\text{nm}$ (radius of 2/3 sphere spot), $\gamma_{water} = 73\text{mN/m}$, and $\gamma_{DMF} = 25\text{mN/m}$, respectively.)

2.1.6. Convective Force for Long-Range SNS Assembly

For highly uniform and close-packed SNS assembled monolayer deposition with spin-coating, two main processes must be considered. The first is capillary assembly driven by interparticle F_{cap} , within a domain region as discussed in the previous section.

The second is the convective particle flux (J_w) [61, 62] into the capillary assembled region which is directly related to long range SNS assembly. J_w can be defined as directional particle motion driven by hydrodynamic pressure differences due to wetting thickness variation between spots, indicating that the existence of a certain amount of solution is essential for effective J_w during spin-coating. The spin-coating process, however, causes very fast liquid evaporation due to its high speed spinning, and thus the vapor pressure must be considered when selecting a solvent.

The commonly used solvent, water has a high vapor pressure ($VP_{\text{water}} = 17.54$ Torr at 20°C) which leads to rapid liquid evaporation during spin-coating and produces a fast reduction of wetting layer thickness variations from center to edge regions on the substrate; consequently, J_w occurs only for a short-time period as illustrated in Figure 2.7 (a). With this insufficient J_w , there is no continuous interaction between SNS due to free SNS regions as schematically shown in Figure 2.7 (c); as a result, only short-range SNS ordered regions are formed followed by localized SNS assembly as shown in Figure 2.7 (e). Because of the evaporation rate issue of the commonly used solvents (*e.g.*, water for SNS and methanol for polystyrene bead), [55, 63] most current spin-coating approaches mix surfactants [57, 64] into the solution or process under controlled temperature and humidity conditions to delay evaporation. [55]

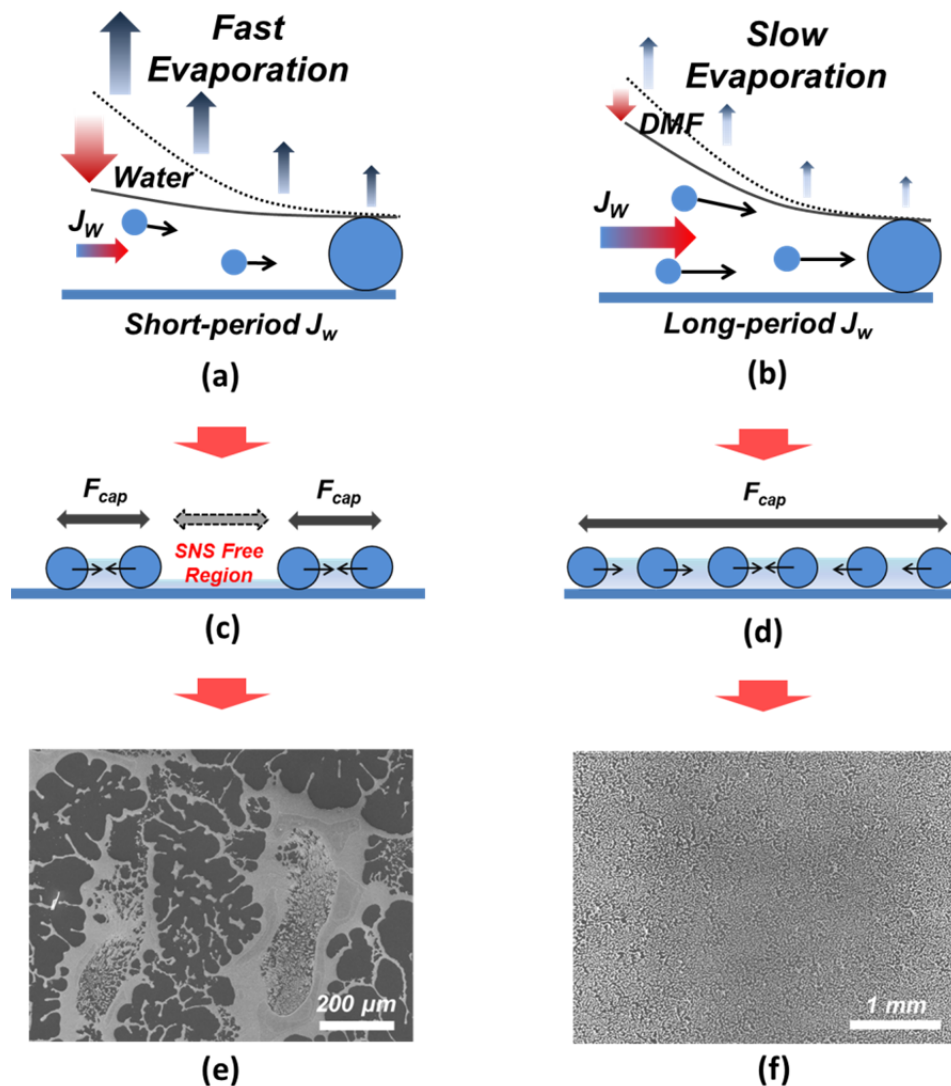


Figure 2.6. Schematic illustration of (a) fast solvent evaporation of water, and (b) slow solvent evaporation of DMF during spin-coating causing (c) discontinuous SNS assembly with localized F_{cap} , and (d) continuous SNS assembly after expanded F_{cap} , and actual SEM images of (e) SNS_{water}, and (f) SNS_{DMF} (50mg/ml of SNS with same spin-coating condition).

DMF, however, provides a significantly delayed liquid evaporation rate caused by its low VP_{DMF} (2.7 Torr at 20°C), which leads to a long-period J_w that delivers a sufficient amount of SNS from disordered regions to ordered regions as illustrated in Figure 2.7 (b).

Therefore, an expanded SNS assembled region is formed with continuous F_{cap} as illustrated in Figure 2.7 (d); consequently, a high uniformity for the assembled SNS layer from center to edge of the substrate is achieved as shown in Figure 2.7 (f).

2.1.7. Large-Scaled Area SNS Monolayer Spin-Coating

In addition to choice of solvent, the solution concentration and spin-coating speeds are also very critical parameters in order to assemble highly uniform SNS monolayers with good coverage over large-scale surface areas. The SEM images in Figure 2.8 show the effect of SNS_{DMF} concentration on the coverage over the 2-inch Si surface. Concentrations of 50mg/ml, 100mg/ml, and 150mg/ml of SNS_{DMF} have been spin-coated to observe their coverage on the surface with a fixed non-optimized spin-coating process (20rpm/s acceleration, 2000rpm for 150sec). From the SEM images, we observe that higher SNS coverage is obtained as the concentration increases to 150 mg/ml SNS_{DMF} .

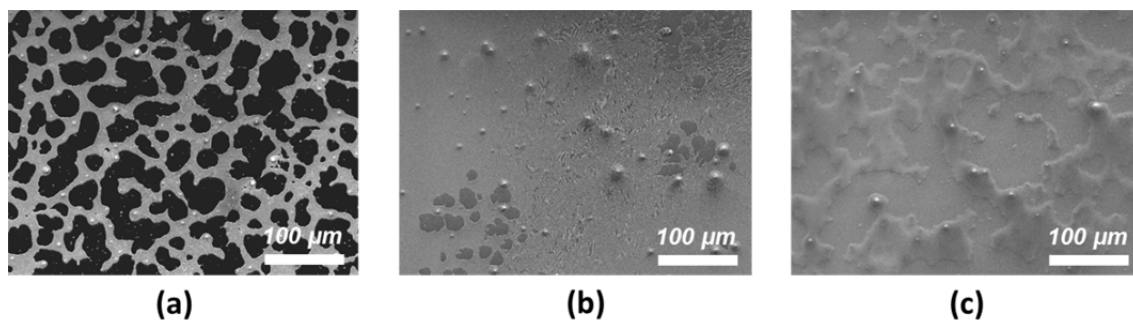


Figure 2.7. SEM images for SNS coverage from various concentration of SNS_{DMF} , which are (a) 50mg/ml, (b) 100mg/ml, and (c) 150mg/ml.

However from Figure 2.8, we can also clearly observe that a further increased concentration produces more severe non-uniformity of the SNS assembly layer. This is because, most probably, the higher concentration of SNS results in a smaller amount of solvent between particles resulting in stronger interparticle interaction with the closer interparticle distance, consequently requiring higher centrifugal force for uniform distribution.[65] Therefore, a well-optimized spin-coating process is required for uniform distribution of SNS over the surface. Generally for self-assembly particle monolayer deposition, the spin-coating process is designed into two steps; (1) a dispersion step at slow spin speed for particle distribution on the surface, and (2) drying step at high spin speed for removing residual solvent to prevent further solvent interactions with the particles.[55] When water is used as the solvent, the surface tension property and high evaporation rate require a dispersion step with slow spin speed to distribute the SNS uniformly with minimize the SNS loss. However, with DMF (low γ_{DMF} and VP_{DMF}) a simplified one-step spin-coating process is possible since a highly uniform SNS distribution can be obtained simply by setting a proper acceleration to target speed. In our process, the target speed is fixed at 2000 rpm/s, but accelerations of 20rpm/s, 50rpm/s, and 80rpm/s were explored with 150-sec of total spinning duration.

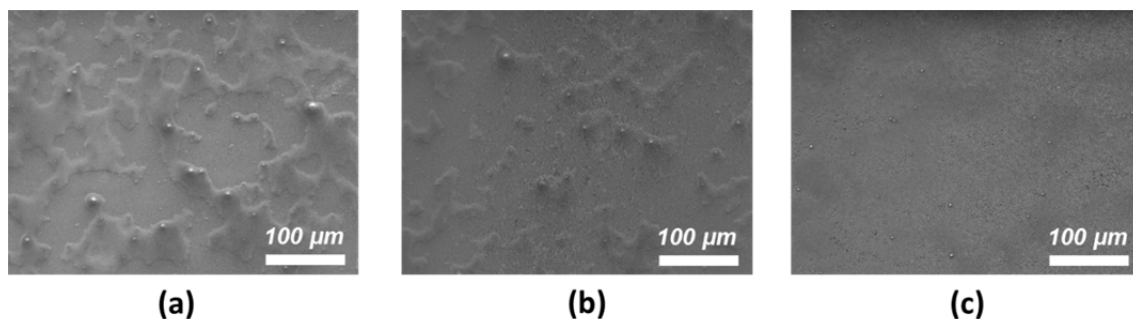


Figure 2.8. Acceleration speed effect for uniform SNS assembly layer formation; (a) 20rpm/s, (b) 50rpm/s, and (c) 80rpm/s.

From Figure 2.9, as the acceleration increased, the surface morphology of the SNS assembly layer improved and, at 80rpm/s acceleration, a very uniform SNS assembled monolayer was obtained. In Figure 2.10 (a), a photograph of a 2-inch substrate after spin-coating at 80rpm/s acceleration is shown, and from the image, ignoring some insignificant defects on the surface, the overall SNS monolayer uniformity is excellent. The SEM images in Figure. 2.10 (b), (c), and (d) at three different magnifications are typical of the SNS film and we find that more than 95% monolayer coverage has been achieved, which compares favorably with the 72% previously reported for spin coated films on 2-inch sapphire substrates.[55]

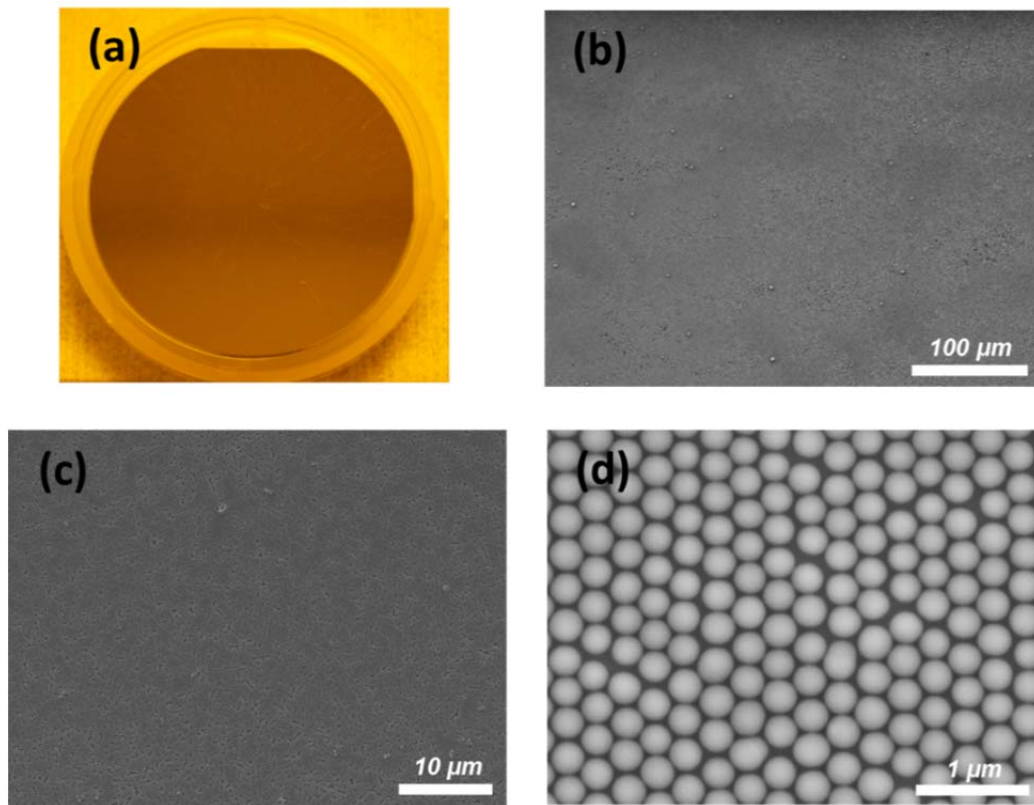


Figure 2.9. (a) SNS deposited 2-inch round Si surface image, and the SEM images with different magnifications, (b) 250x, c) 2000x, and (d) 25000x, respectively.

Furthermore, we also tested 4-inch round substrates to investigate the feasibility of DMF for SNS assembled monolayer spin-coating on an even larger-scale surface area using the identical spin-coating recipe and SNS_{DMF} concentration. The only parameter changed was the dispensed solution volume which was 800μl (300 μl for 2-inch) to compensate for the increased surface area. As shown in the photograph and SEM images in Figure 2.11, we found that the DMF based solution performs well on larger substrates with more than 90% averaged monolayer coverage achieved on 4-inch wafers with good monolayer uniformity. For 4-inch wafer spin-coating, however, there were some less SNS covered (76~88%) areas observed as shown in Figure 2.11 (c).

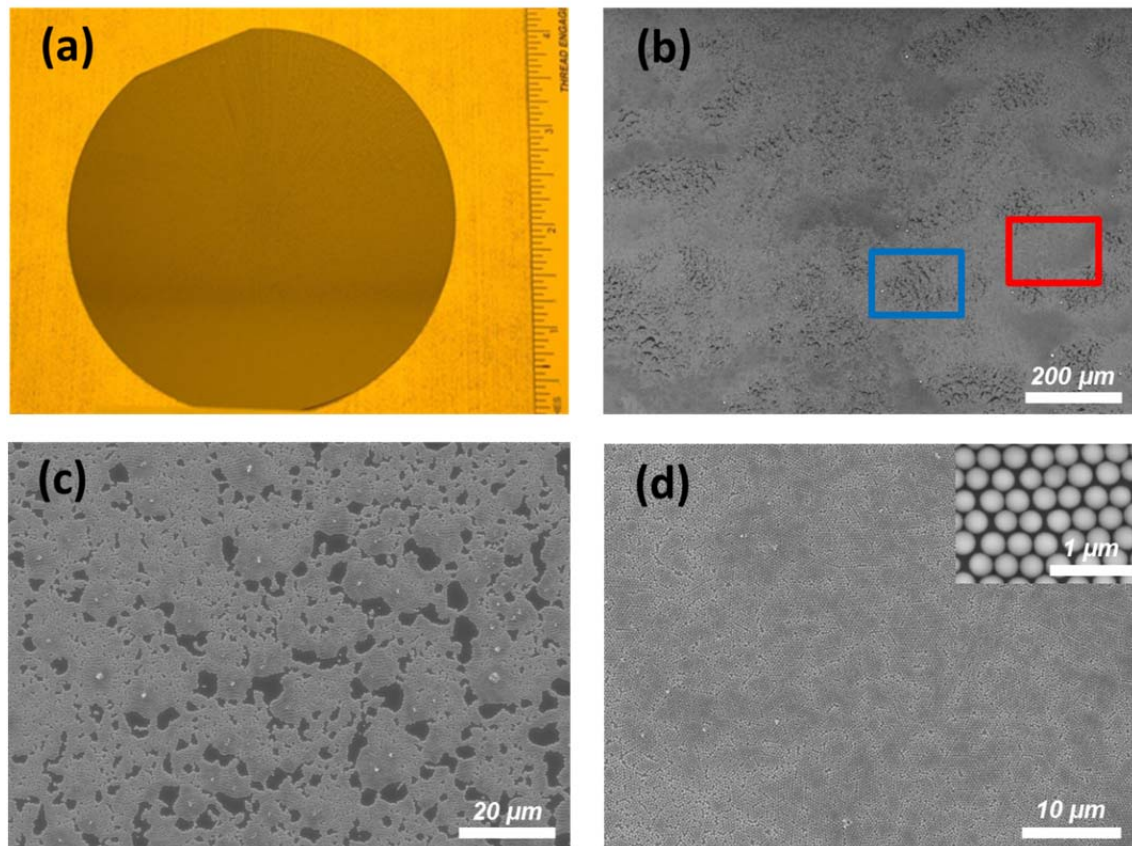


Figure 2.10. (a) SNS deposited 4-inch round Si surface image, SEM images of (b) low magnification, (c) less SNS monolayer coverage region of blue solid-box in (b), and (d) high SNS monolayer coverage region of red solid-box in (b).

Based on our experiments (see Figure 2.8), the appearance of this reduced coverage area is typical when the solution concentration was not optimal and therefore we believe that the coverage can be further improved by adjusting the solution concentration. However, even without further optimization, we credit as a rare success the SNS spin-coating of a 4-inch wafer at this level of monolayer coverage and uniformity without special environment controls or additional surface functionalization.[59]

2.1.8. Spin-Coating of SNS in Various Diameters: Diameter vs. SNS Solution Concentration

In this section, we also demonstrate the effectiveness of our DMF introduced spin-coating method to deposit SNS with various diameters. Three different sizes of SNS (310, 600, and 840 nm in diameter) are tested to observe the relation between SNS diameter and concentration to produce maximum SNS monolayer coverage (>95%) on 2-inch Si wafer surface. In Figure 2.26 (a) ~ (c), photographs and SEM images of three 2-inch Si wafers are shown with three different SNS sizes: 310, 600, and 840 nm in diameter, respectively, and all have more than 95% monolayer coverage.

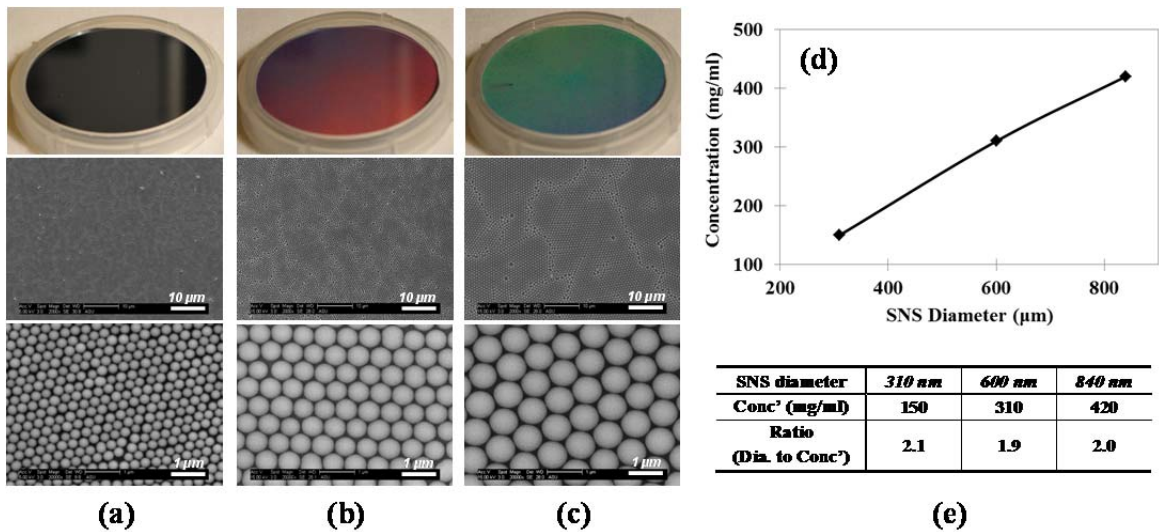


Figure 2.11. Different size of SNS in (a) 310nm, (b) 600nm, and (c) 840nm diameters, spin-coated on 2-inch Si wafers (Top, middle, and bottom of (a) ~ (c) represent the whole 2-inch wafer with each SNS, $\times 2k$, and $\times 20k$ magnification SEM images, respectively.), (d) Optimum SNS solution concentration vs. SNS diameter for spin-coating and (e) table representing the ratio of SNS diameter (Dia., nm) to solution concentration (Conc', mg/ml) for spin-coating.

From the Figure 2.21(d), we observe that the most optimal concentration of DMF based SNS solution just proportionally increases with the SNS diameter along with its phenomenal SNS monolayer uniformity. From the Figure 2.21(e), the ratio of SNS diameter (Dia.) to solution concentration (Conc') is around "2" for all three diameters of SNS. Therefore, with our spin-coating method, uniform coatings of various sizes of SNS are achieved by simply changing the SNS solution concentration based on the SNS diameter. This provides the user with the capability to control the period (or density) of fabricated Si nanostructures.

2.1.9. DMF vs. Other Solvents

In addition to DMF, we also tested other solvents for SNS spin-coating such as dimethyl-sulfoxide (DMSO) which offers a high boiling temperature (189°C), reduced γ ($\gamma_{\text{DMSO}} = 43.5\text{mN/m}$) compared to water (73mN/m), and less toxicity than DMF. However, its high viscosity (2.0cP at 20°C) produced severe non-uniformity and multi-layered SNS films after spin-coating as shown in Figure 2.12 (a) and (b). These results show the importance of each and every solvent property and their combination in producing uniformly distributed SNS monolayers in close-packed arrays with spin-coating. Therefore, we believe that, regardless of the toxicity concerns of DMF, it offers highly optimal solvent properties for large-scale surface area SNS spin-coating accompanied by outstanding SNS monolayer uniformity and coverage even under common ambient lab conditions.

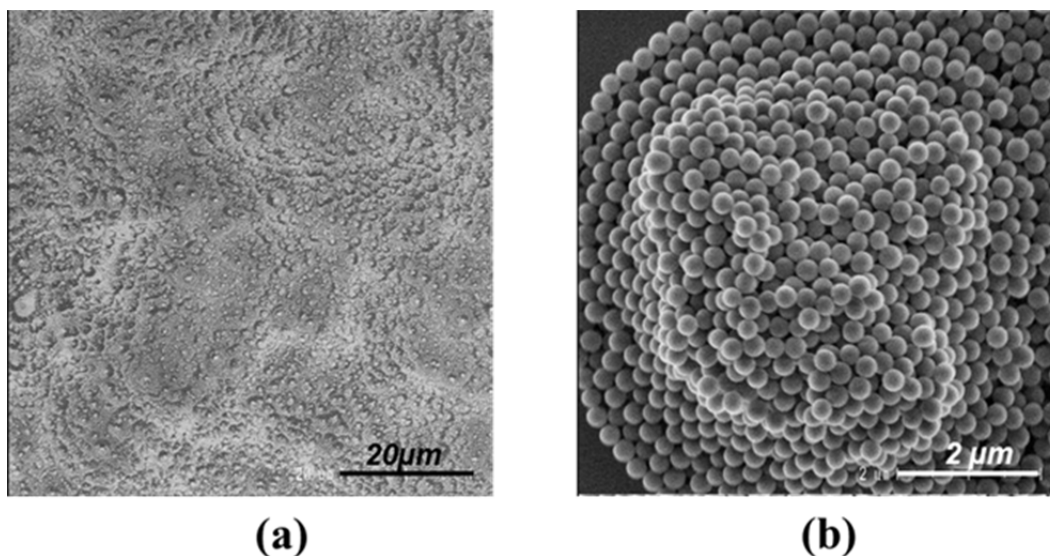


Figure 2.12. SEM images of DMSO introduced SNS (310nm) spin-coated Si surface which shows (a) severely non-uniform, and (b) multi-layered SNS film. (Note: Spin-coating condition was 80rpm/sec acceleration and 2000 rpm/sec maximum speed for 200-sec)

2.1.10. Summary

We have introduced the use of DMF as a solvent for spin-coating SNS assembled monolayers on silicon wafers under ambient laboratory conditions without the addition of surfactants or special surface treatment of the Si. In comparison with the commonly used solvent, water, it becomes obvious that DMF offers optimal solvent properties for the SNS spin-coating application. First, DMF leads to highly dispersed SNS in the solution which is close to the theoretical limit, important in producing a uniform SNS distribution on the surface. Second, the outstanding wettability of DMF caused by its low surface tension ($\gamma_{\text{DMF}} = 25\text{mN/m}$) at the liquid / solid interface provides superior coverage and uniformity of the SNS assembled monolayer compared to the same volume and

concentration of SNS in water. In addition, the low γ_{DMF} also improves the interparticle interaction since the enhanced wetting of the solution leads to a higher density of SNS placed near the surface reducing the interparticle distance. Third, the slow evaporation rate of DMF is desirable for spin-coating applications. Based on these outstanding DMF properties, we successfully demonstrate excellent coverage with high uniformity of the SNS monolayer on 2-inch (~ 95%) and 4-inch (~90%) Si substrates. Furthermore, different sizes of SNS can be coated simply by adjusting the SNS concentration in the solution which is easily estimated by diameter of SNS. From these achievements, it is clear that DMF has a great potential for a high-throughput SNS spin-coating application with simple, and low-cost spin-coating approach to produce highly uniform colloidal particle monolayer assembly over large-scale surface which can be used as a mask layer for Si surface nano-lithography.

2.2. Surface Nano-patterning

2.2.1. SNS Size Reduction by Reactive-Ion Etching (RIE)

One of major advantages of using SNS for lithography application is that SNS (i.e., SiO₂) can offer stable and uniform etching with plasma assisted dry etch to produce desired surface pattern size after SNS size reduction. Currently, the most reported colloidal sphere lithography techniques are based on polystyrene spheres (PS) which it is highly challenging to produce repeatable size control and well-defined patterns because of its soft material nature.

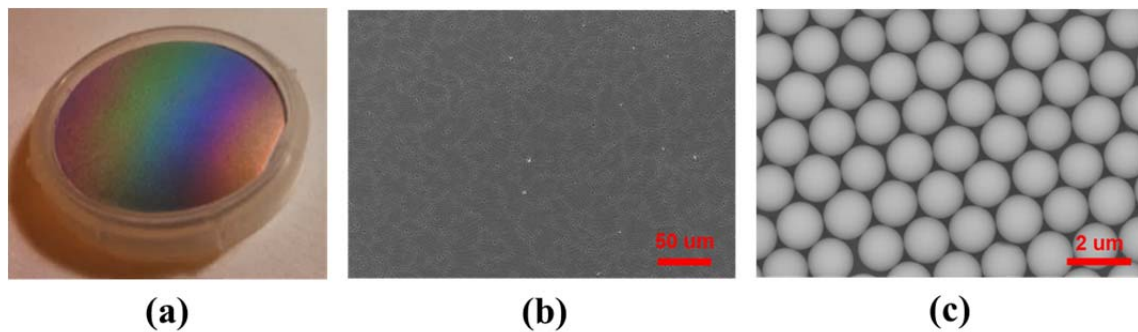
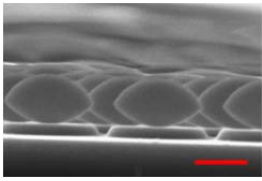
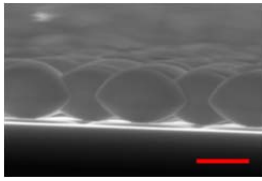
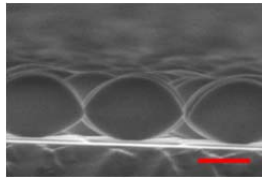


Figure 2.13. (a) Spin-coated 2-inch round Si surface images and SEM images of (b) uniformly distributed SS and (c) closely-packed SS shown in different SEM magnifications.

For effective SNS size reduction, there are two criteria to consider; (1) high enough SNS etching selectivity with Si, and (2) effective horizontal direction etching of SS with minimized vertical etching rate. The high SNS etching selectivity is important because excess Si etching during SNS size reduction would affect the shape of target surface geometry after nanostructure fabrication. Directional selective SNS etching is

needed to adjust the lateral dimensions while maintaining sufficient vertical height to permit clean SNS removal and mask layer liftoff. 1.57 μ m large diameter of SNS was used to optimize the SNS etching condition due to its relative large size can provide better visible observation on etching selectivity and orientation. The deposited 1.57 μ m SNS is shown in Figure 2.13.

Table 2.1. Comparison of CHF₃ / Ar gas RIE etching profile for 10-min etching on SS deposited Si surface which were performed under three different chamber pressures.

Pressure Property	50 mTorr	75 mTorr	100 mTorr
Cross-sectional SEM Image (Scale-bar : 500nm)			
Vertical Etching rate (nm/min)	90.3	80.3	70.3
Horizontal Etching rate (nm/min)	34.8	30.3	18.1
Vertical / Horizontal Etching ratio	2.6	2.6	3.9

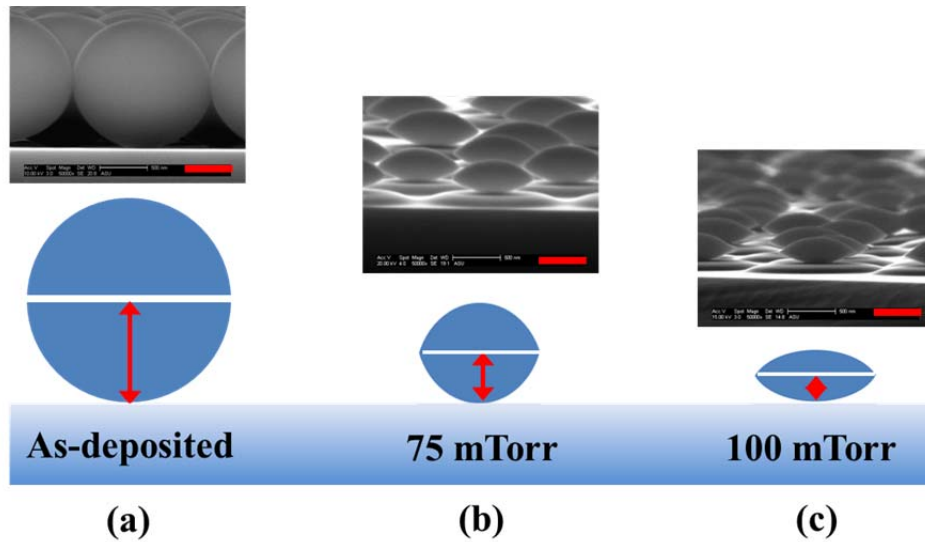


Figure 2.14. Schematic illustration (top) and SEM images (bottom) to compare the effect of RIE chamber pressures, (a) as-deposited SS, (b) 75mTorr RIE processed SS (horizontal dia. \sim 800nm, vertical dia. \sim 350nm), and (c) 100 mTorr RIE processed SS (horizontal dia. \sim 800nm, vertical dia. \sim 260nm).

Based on these considerations, we utilize a CHF_3/Ar gas combination in our process and have optimized its etching conditions by applying different gas flow rates, RF power, and chamber pressure. From the experiments, we observe that chamber pressure is the most critical parameter for both of high SNS etching selectivity and low vertical / horizontal etching ratio. Wide range of chamber pressure was tested, and results from three different chamber pressures (50, 75, and 100mTorr) are shown in Table 2.1. With 50mTorr chamber pressure, a noticeable etching of the Si substrate between the SNS was observed due to intensified ion-bombardment.[66] Therefore, we increased the chamber pressure to 75 and 100mTorr, resulting in significantly less Si substrate etching because of the decreased mean-free path of ionized-species. However, even though higher chamber pressure results in further reduced Si substrate etching, the vertical /

horizontal etching ratio (calculated from radius change in each direction after 10-min etching) listed at the bottom of Table 2.1 increased for 100mTorr. As mentioned before, this excess etching rate in the vertical direction is not ideal for SNS lithography because a relatively fast vertical diameter reduction compared to that of the horizontal direction potentially restricts the choice on the pattern size weakening the ability of the SS to pattern the surface as SNS size decreases. As shown in Figure 2.13, for the same SNS target size (~800nm), a higher chamber pressure, 100mTorr in Figure 3(c), produced a reduced vertical SNS radius compared to that of the lower chamber pressure, 75mTorr in Figure 2.13(b), due to its relatively faster vertical direction etching. Therefore, 75mTorr was used for SNS size reduction resulting in acceptable Si substrate etching and increased flexibility for target pattern size.

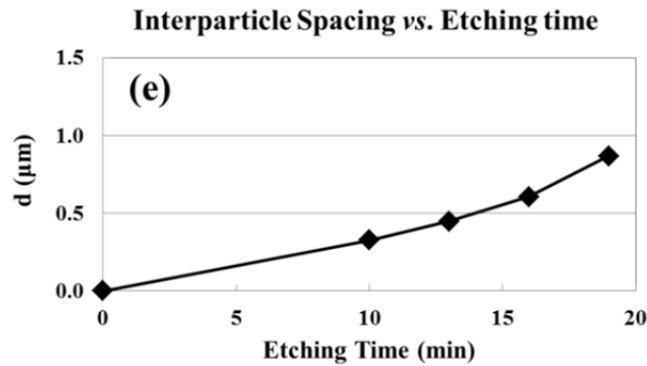
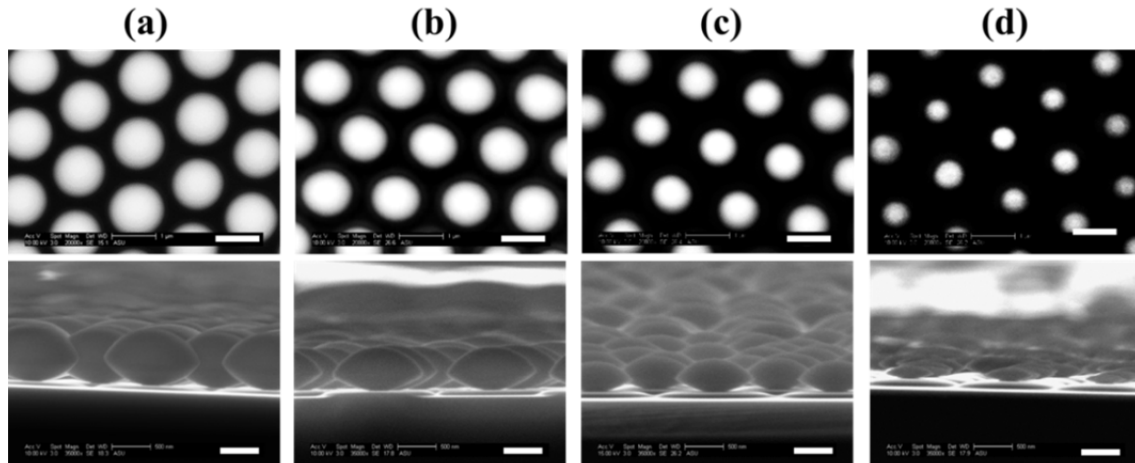


Figure 2.15. (a) ~ (d) SEM images of RIE etched SS with various etching times, 10-min, 13-min, 16-min, and 19-min, respectively, and (e) diagram of inter-particle spacing (d) versus RIE etching time. (Note: RIE conditions are 75mTorr chamber pressure, 200 Watts RF plasma power at 25/25sccm gas flow rate) (scale bar: 1 μm for top image, 500nm for bottom image).

In Figure 2.14, RIE etched 1.57 μm SNS is shown with various etching times (10, 13, 16, 19-min) under the optimized RIE conditions. From the SEM images in Figure 2.14 (a) ~ (d), highly effective SNS size reduction was observed with minimal Si substrate etching. In addition, from Figure 2.14(e), the measured inter-particle spacing with different etching times showed that SS size can be easily reduced in a desired scale due to its reasonably linear relation between reduced SS diameter and etching time.

Moreover, as observed from Figure 2.14(a) ~ (d) top, after RIE, there was still highly well-defined circle shape of SNS without any rugged edge which often occurs with soft PS.[58, 67] Therefore, by using optimal RIE condition with various sizes of SNS, a highly controlled surface pattern can be produced in a desired period and size.

2.2.2. SNS Removal after RIE

In the previous section, we showed that CHF_3/Ar RIE etching can provide effective SNS selective etching to the Si substrate. However, CHF_3/Ar RIE also causes an issue for SNS removal following mask layer deposition. This is because there is a formation of a thin C_xF_y compound layer on all exposed surfaces during the etching process,[68] and this C_xF_y compound is highly stable in a hydrofluoric acid based solution like BOE; as a consequence, clean SNS removal using BOE cannot be achieved as schematically shown in Figure 2.15(c) and (e) where the red solid-line indicates the residual C_xF_y compound layer. In addition, the C_xF_y also has strong mechanical property; mechanical SNS removal process (*i.e.* sonication) is not effective for clean SNS elimination. (Note: Here, BOE solution etching is used for SNS removal, but later sonication process is also used to exclude acid involvement during process)

From the illustration and subsequent SEM image in Figure 2.15(e), a sample after Cr evaporation and BOE etch / liftoff, the C_xF_y residue results in a collapsed metal mask layer and incomplete metal liftoff. The SS itself have been etched away by infiltrated BOE solution. For clean SNS removal from Si surface, therefore, we introduced a simple

no-vacuum required UV-ozone (UVO) surface treatment before the Cr evaporation because of its effective organic contamination removal in a non-aggressive environment. From Figure 2.15(f) bottom, the SEM image of a sample treated with a 10-min UVO treatment before Cr evaporation and BOE (10:1) etch shows very clean SS removal from the Si surface, resulting in well-defined surface patterns.

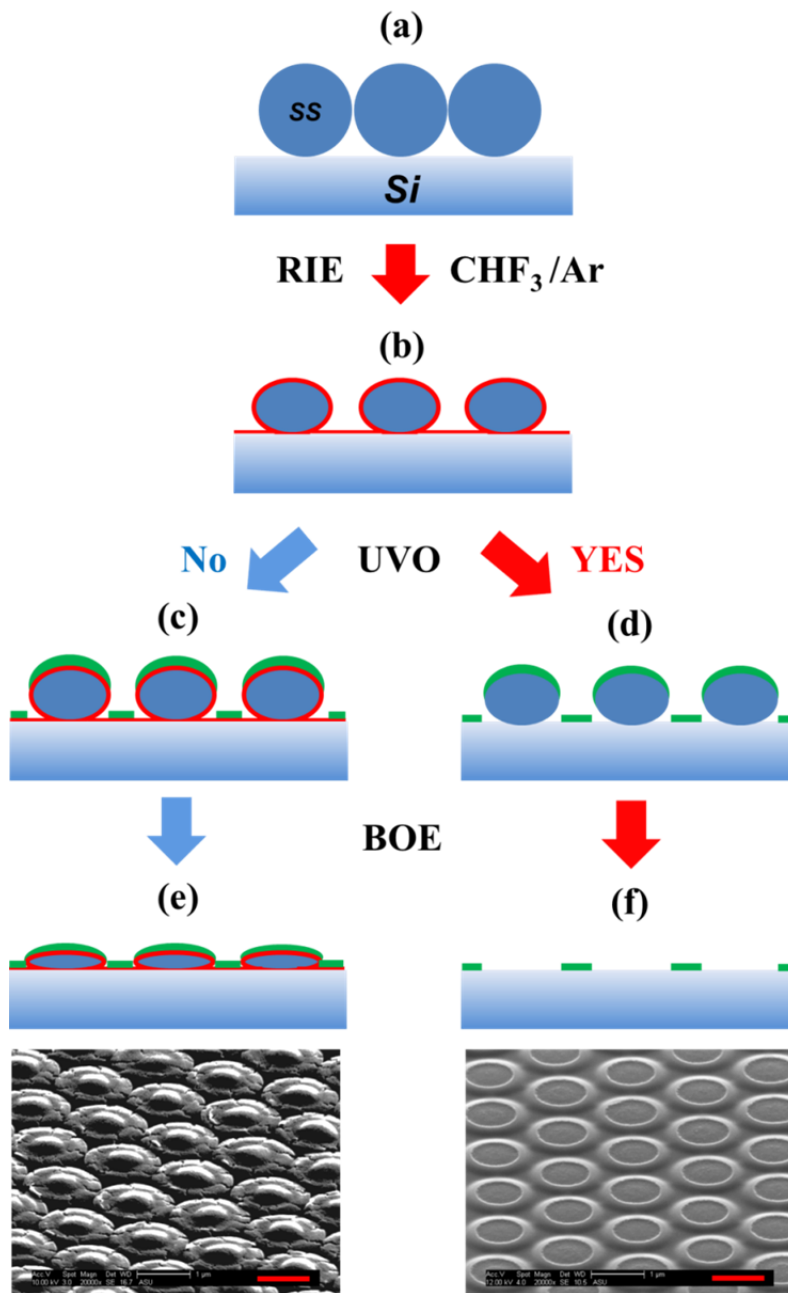


Figure 2.16. Schematic illustration of SNS lithography process and UVO effect to produce clean Si surface patterning, and (e) bottom is SEM image of non-UVO treated sample, and (f) bottom is UVO treated sample. (Green-line indicates deposited Cr layer, and red-line indicates C_xF_y compound layer on the surface, scale-bar = 1 μm)

2.3. Fabrication of Si NP with Metal-assisted Chemical Etching

In this section, we demonstrate our effective Si nanopillar (Si NP) fabrication process to produce Si NP with highly well-controlled structural dimension (*i.e.* period, diameter, and height). The dimension control of fabricated Si nanostructures in a chosen period is a key consideration in fields like opto-electronics for effective light diffraction and/or scattering, [69, 70] which are also highly crucial to realize enhanced light absorption for thin Si solar cells.

Here, we show our novel fabrication process for Si NPs with control over both period and dimension. A metal-assisted chemical etching (MaCE) technique is introduced to provide a fast and low-cost etching process that achieves effective vertical etching with minimal size variation of the NPs. Various interface metal layers (Cr, Ti, and Ni) are investigated as Au adhesion layers and Ni is determined to produce enhanced lithographical accuracy for highly uniform Si NP fabrication of an intended dimension. Moreover, for MaCE, the influence of fractional catalyst coverage on etch rate and controlled vertical etching is investigated.

2.3.1. Experimental Section

The SNS solution was prepared with powders of 310nm, 600nm, or 840nm diameter SNS (Bang Lab.) which were dispersed in N,N-dimethyl-formamide (DMF) (Sigma-Aldrich) at an optimized concentration. The solutions were sonicated for 5 hours to produce complete dispersion of the SNS.

The test substrates consisted of 2-inch round polished n-type Si (100) wafers (280 μ m thickness) cleaned in a piranha solution [H_2SO_4 (96%): H_2O_2 (30%) = 4:1] for 15minutes to form a hydrophilic Si surface followed by a 10minute DI-water rinse.

SNSs were spin-coated under common ambient lab conditions at 2000rpm/sec (80rpm/sec acceleration) for 120 seconds after dropping 300 μ l of solution on the wafer surface. The uniformity of SNS spin-coated samples was observed by scanning electron microscopy (SEM, JEOL XL-30), and the coverage of the SNS monolayer was calculated by direct counting of the SNS covered area on the Si surface through image analysis software, “image J” (National Institutes of Health, USA)[71] as shown in our previous report.[72]

SNS coated Si substrates were then transferred to the reactive ion etching chamber (Oxford PlasmaLab 80+, RIE) and the SNS size reduction was performed using a CHF_3/Ar gas combination with 200 watts RF plasma power at 25/25sccm gas flow rate and 75mTorr chamber pressure followed by a 2-min O_2 plasma clean with 100 watts at 45sccm gas flow rate and 150mTorr chamber pressure to remove surface organic contamination resulting from the CHF_3/Ar RIE. (Note: The O_2 cleaning step after RIE is highly crucial for later complete SNS removal.) Metal layers for the subsequent MaCE

process were deposited with an electron-beam evaporator (Lesker PVD-75); then the SNS were removed by sonication in water.

The MaCE solution was prepared by mixing 2.5vol% hydrogen peroxide (H_2O_2) with 10vol% hydrofluoric acid (HF, 49%) in DI-water. Etching was performed by immersing samples into the etching solution while stirring. After MaCE, the Au layer was removed by dipping in Au etchant for 5-min.

2.3.2. SNS Diameter Control with RIE

Here, we measured the etching rate of SNS with various initial diameter which are shown in Figure 2.17 (310, 600, and 640nm in diameter) to investigate the relation between etching rate and SNS size. This is because in addition to structure period, the fabrication of Si nanostructures in a certain dimension is also highly crucial to realize certain optical property. For instance, the study by Spinelli, *et al.* has demonstrated that well-defined Si NPs with optimized period and dimension can offer enhanced forward scattering of incident light providing an improved omnidirectional anti-reflection effect over a broad wavelength range.[69] Furthermore, the study by Sang Eon *et al.* emphasized the importance of Si nanostructure size (or Si filling fraction) in producing strong transmitted light diffraction for enhanced light absorption.[73] Thus effective SNS dimension control is highly crucial to offer highly enhanced optical property for thin Si solar cell application.

The advantage of using SNS for the NSL process as opposed to widely available polystyrene sphere (PS) is that SNS (*i.e.*, SiO_2) offers sufficient etching selectivity to Si

which allows uniform SNS size reduction with an RIE process. Of course, size reduction of PS is possible, but the soft material nature inevitably produces a non-uniform result; consequently, the fabricated nanostructure has a rough surface.[74, 75] This rough surface is especially problematic for surface dominant device application like solar cells since it generally increases the surface recombination velocity and consequently degrades solar cell performance.[76]

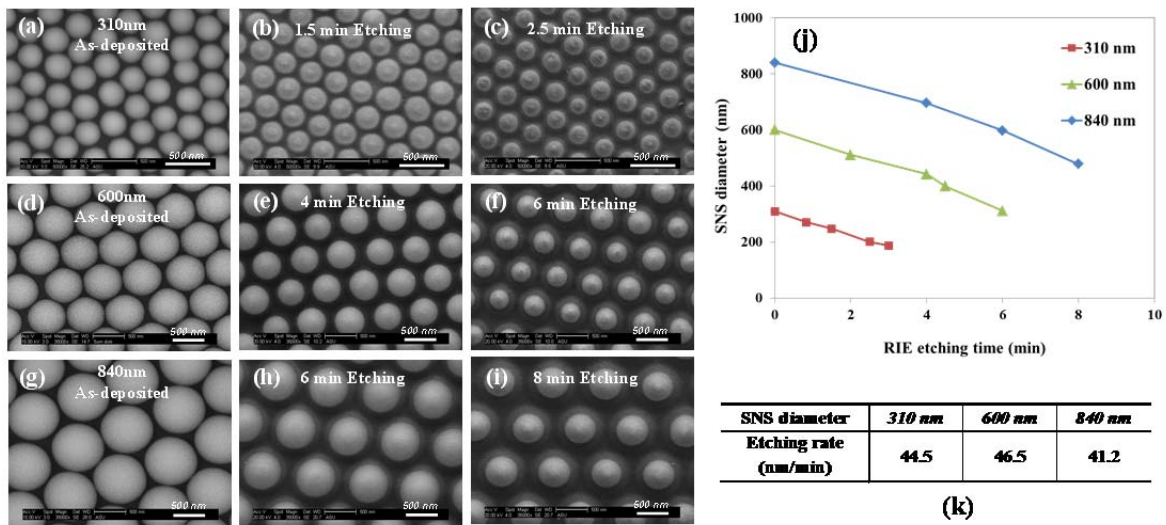


Figure 2.17. Three different sizes of SNS in (a) 310nm, (d) 600nm, and (g) 840nm in diameter, and RIE etched with two different etch times. (b), (c) are 1.5-min and 2.5-min on 310nm SNS, (e) and (f) are 4-min and 6-min on 600nm SNS, and (h) and (i) are 6-min and 8-min on 840nm SNS. (j) the SNS diameter change vs. RIE time, and (k) a table showing etch rates for each SNS.

In Figure 2.17 (a) ~ (i), plan view SEM images of RIE etched SNS with different initial diameters prior to and after etching clearly reveal uniform SNS etching retaining a smooth circular shape. In Figure 17 (j) and (k), the SNS horizontal etching rates are shown to be relatively constant, ranging from 41.2 ~ 46.5 nm/min as the RIE etching time

increases regardless of initial SNS size. Therefore, effective size control of the SNS mask layer can be achieved with well-defined shapes.

2.3.3. Metal Cathode Layer Deposition for Surface Patterning

The above described SNS nano-lithography technique has been combined with MaCE technique to fabricate well-defined Si NPs. The MaCE process requires a metal catalyst layer to reduce the Si surface, forming SiO₂ which is etched away by HF mixed in the MaCE solution. An Au cathode layer was chosen since Au offers a slower etch rate compared to other noble metals (*i.e.*, Pt, and Ag) and thus provides controllable etching for Si NPs fabrication.[77] In addition, the process with Au etches Si vertically without a porous layer formation, and avoids unexpected surface morphology changes.[78] Au, however, inherently has weak adhesion to the Si surface which is problematic in our process. After Au layer deposition, a lift off process is used to remove the SNS mask layer to avoid etching of the Si NPs related to the Au-covered SNS as shown in Figure 2.18 (a). The SNS removal is performed with sonication which leads to Au layer lift-off from the Si when the adhesion is poor as shown in Figure 2.18 (b). Therefore, an Au adhesion layer must be introduced and here, three different interfacial metal layers, Cr, Ti, and Ni, are tested. For the test, 3nm of each adhesion layer is deposited before a 30nm Au layer deposition. Figure 3 shows SEM images of patterned Au layers with different adhesion layers taken before and after the 1-hr sonication in DI-water for SNS removal.

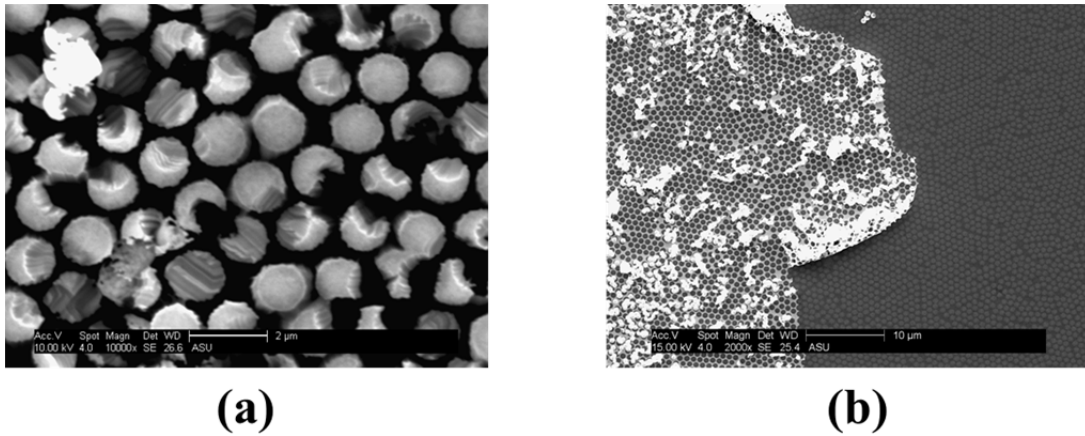


Figure 2.18. (a) The etched Si nanopillar had un-expected structure damage by incomplete SNS removal due to metal catalyst covered on SNS, and (b) peel-off Au metal layer during SNS removal due to weak adhesion of Au on bare Si surface.

The diameter of the SNS before metal layer deposition was an average of 611nm (Period: 840nm) as shown in Figure 2.19 (a). After SNS removal by sonication, the diameter of each pattern is measured and as shown in Figure 2.19 (b) ~ (d) with red numbers, Cr and Ti produced a significantly larger diameter, 722nm and 667nm, respectively, than the initial SNS diameter, 611nm, but the Ni/Au metal layer combination resulted in an average pattern diameter of 622nm and this is very close to the initial SNS size. Therefore, the Ni interfacial layer for Au offers the best lithographical accuracy for Si NPs fabrication in a desired diameter.

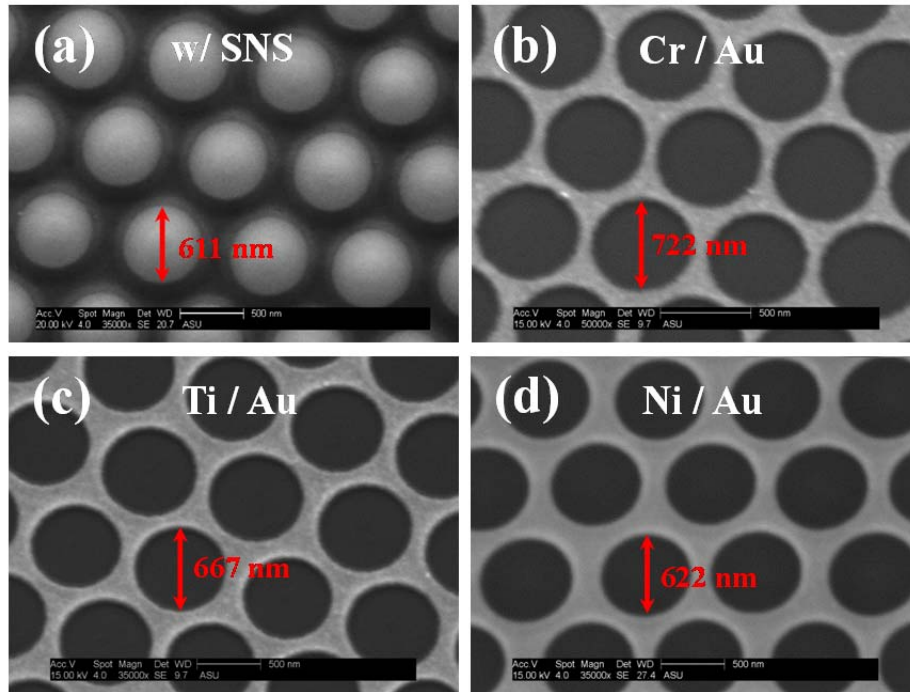
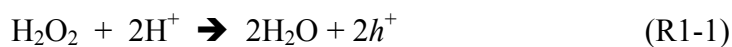


Figure 2.19. (a) Si surface with SNS etched to 611 nm average diameter (840 nm period), (b) Cr/Au, (c) Ti/Au, and (d) Ni/Au deposited Si surface after SNS removal which have 722 nm, 667 nm, and 622 nm diameter of pattern, respectively.

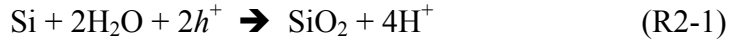
2.3.4. Fabrication of Si NP with MaCE Technique

The MaCE technique is used to fabricate Si NPs since it provides vertical etching with minimal diameter variation from top to bottom. One of the widely accepted mechanisms for the MaCE galvanic process is summarized by the two half-cell reaction below: [74, 79-82]

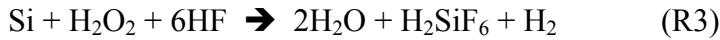
Cathode reaction at the metal:



Anode reaction at Si:



Overall reaction:



The galvanic process was schematically illustrated in Figure 2.30 in steps 1 through 4.

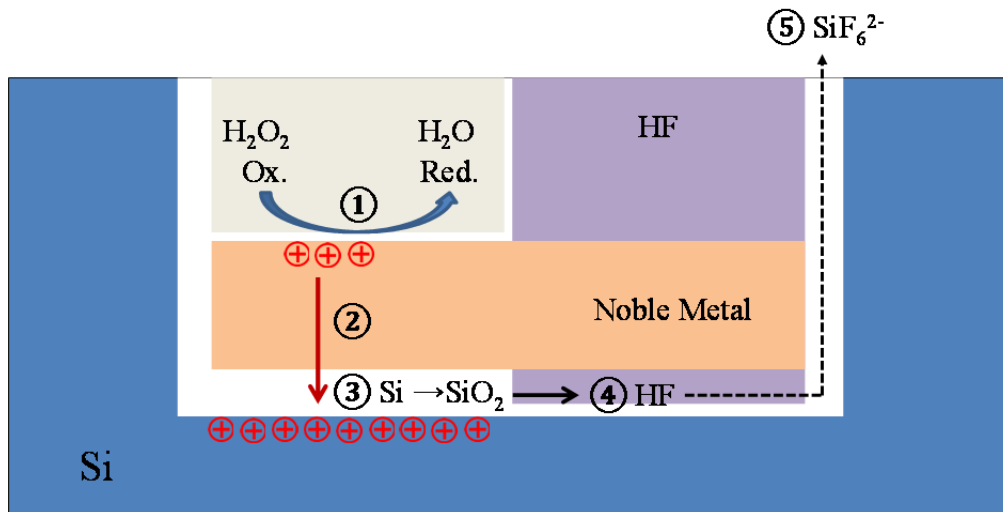


Figure 2.20. Scheme of reaction processes for metal-assisted chemical etching based on galvanic process. (1) The oxidant (i.e., H₂O₂) is reduced by the catalytic activity of noble metal. (2) The generated holes from reduction of oxidant consequently diffuse to Si/metal interface through metal layer. (3) The oxidation of Si is occurred by the injected holes, and (4) SiO₂ is reacted with HF. (5) Finally, SiO₂ is dissolved and etched away into the solution.[82]

We found that a Ni/Au layer provided a precise control on surface pattern size and subsequent Si NPs dimension as fabricated with MaCE. In Figure 5, plan view and

angled SEM images of three different dimensions of the SNS features and the resulting MaCE fabricated Si NPs are presented. Figure 21(a), (d), and (g) represents the SNS etched to 600nm, 445nm and 223nm average diameters (Note: these diameters represent 50% Si filling fraction in the structured layer) arrayed at 840nm, 600nm, and 310nm periods, respectively. Figure 21(b), (e) and (f) are plan view SEM images and (c), (f) and (i) are 80 degree angled SEM images of the NPs. The red solid-arrow for each period is the identical length and indicates good lithographic accuracy.

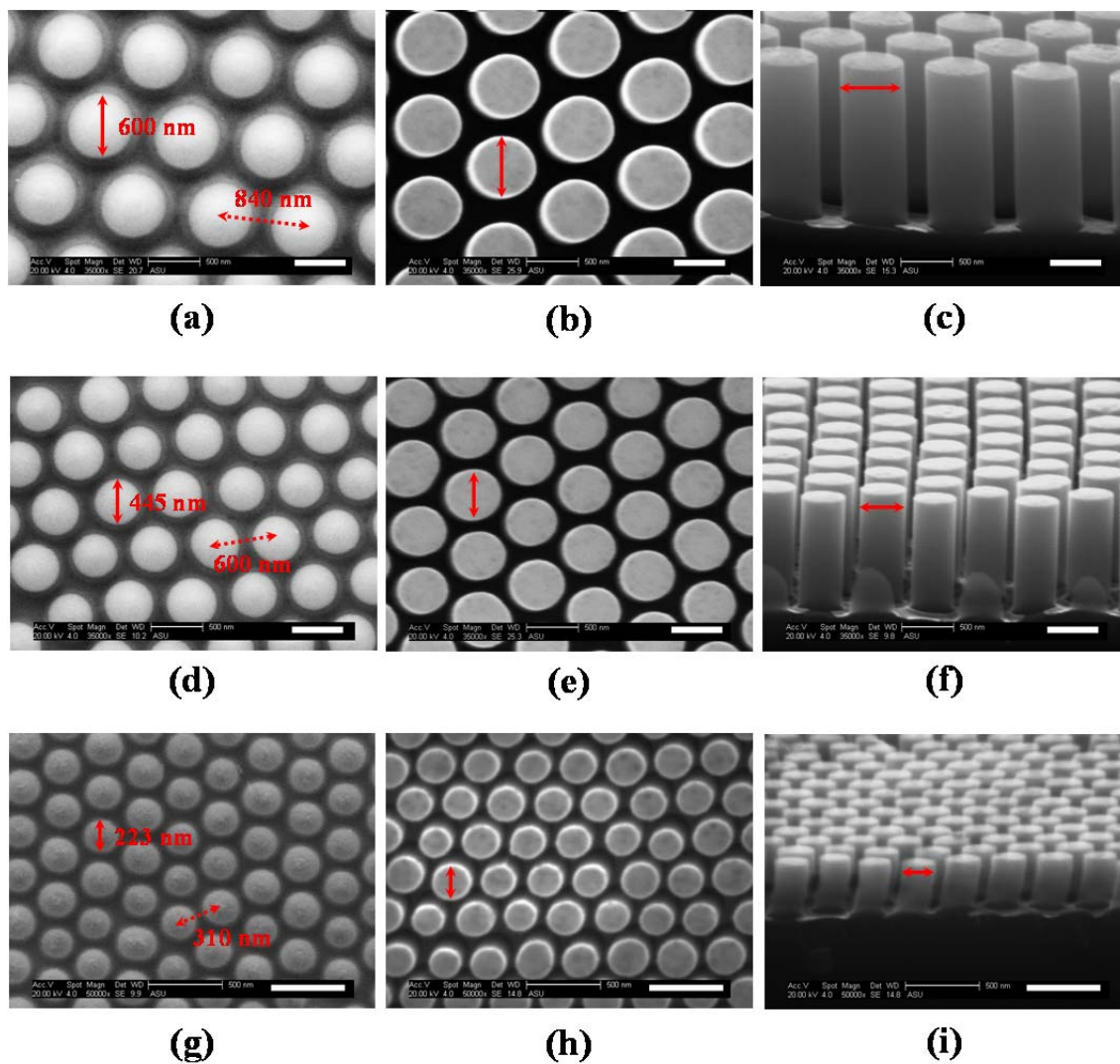


Figure 2.21. (a), (d), and (g) are RIE etched SNS with 840, 600, and 310 nm initial diameter. (b), (e), and (h) are up-side SEM image, and (c), (f), and (i) are 80 degree angled SEM images for Si NPs.

In addition to period and diameter control, a reproducible vertical etching rate for MaCE is crucial for Si NP fabrication. Therefore, the etching rates with different fractional Ni/Au catalyst coverage were investigated. Three different fractional coverage (30%, 50%, and 70%) of the Ni/Au layer, were deposited as shown in Figure 2.22 (a) ~ (c) and dipped in the MaCE solution for 5-min, with the results as shown in Figure 2.22 (d) ~

(f). From the height of the etched Si NP, a gradual increase of etch rate was observed as the catalyst fractional coverage increased. The plot of the etch rate versus catalyst coverage indicated that 30%, 50%, and 70% Ni/Au fractional coverage produced 63, 77, and 104 nm/min etching rates, respectively (see Figure 2.22 (g)). The faster etch rate, with the larger fractional coverage of catalyst, was explained by enhanced penetration of etching solution with larger catalyst coverage due to wider inter-spacing between etched Si NPs. Since the etch depth increases linearly with etch time for MaCE,[82] the etch times were estimated for a desired height of Si NP. In Figures 2.22 (h) ~ (j), we fabricated approximately 500 nm height of Si NPs having 70%, 50%, and 30% Si filling fractions in the structured layer. The Si NPs were produced after dipping in the etching solution for 8-min, 6.5-min, and 5-min, respectively, which were determined based on the measured etch rates in Figure 2.22 (g). As a result, fabrication of Si NP in a desired period and dimension was successfully achieved.

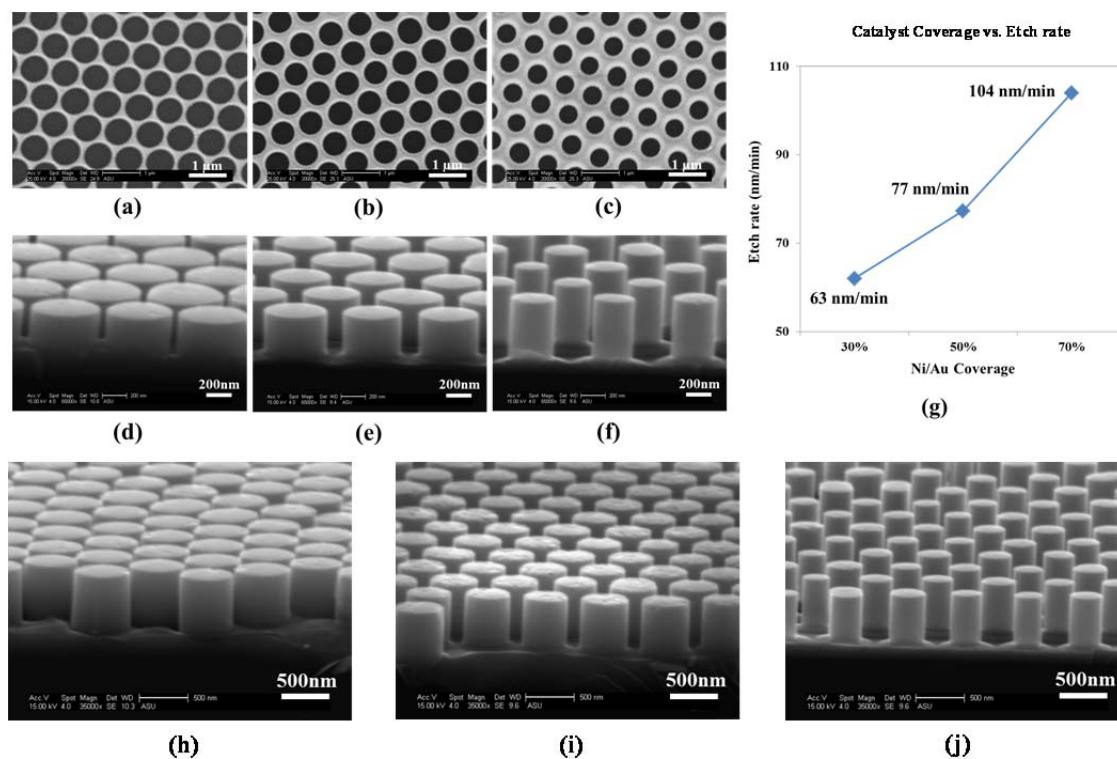


Figure 2.22. Ni/Au catalyst deposited Si surface with (a) 30%, (b) 50%, and (c) 70% fractional coverage, and (d) ~ (f) Si NPs fabricated from each catalyst fractional coverage after 5-min etching in MaCE solution. (g) Etch rates from each Ni/Au fractional surface coverage. (h) ~ (j) ~ 500nm height of Si NPs from (a) ~ (c) after dipping in the etching solution for 8-min, 6.5-min, and 5-min, respectively.

In addition, we also confirmed our nano-fabrication process can offer phenomenal uniformity of fabricated Si NP as shown in Figure 2.23.

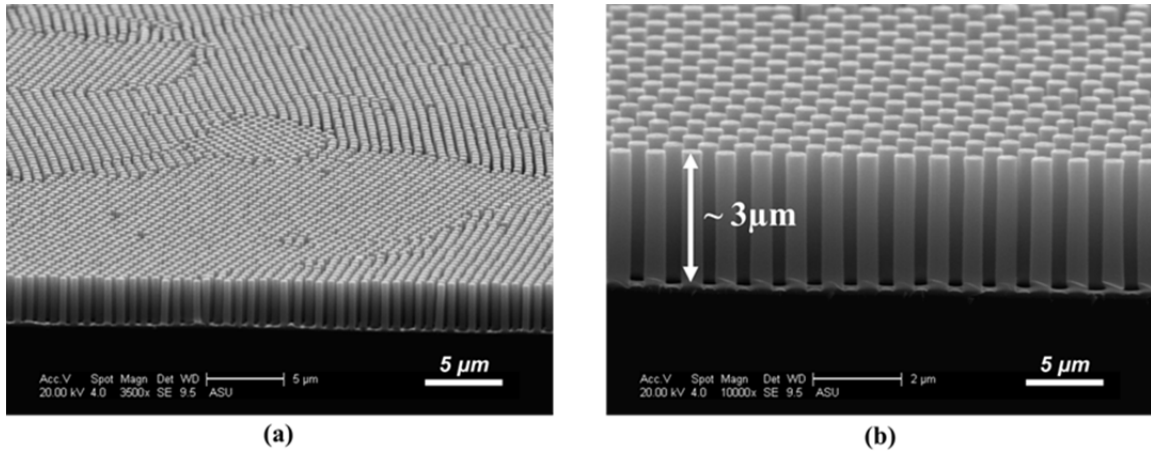


Figure 2.23. SEM images of fabricated Si NP array at 3 μm height in 840nm period (50% Si FF) to confirm the uniformity of the Si NP array over the surface; (a) $\times 35\text{K}$, and (b) $\times 10\text{K}$ magnifications.

2.3.5. Summary

An improved method for fabricating desired aspect ratio Si NPs using silica nanosphere lithography in combination with metal assisted chemical etching has been developed. To produce a desired dimension for the SNS mask layer in a fixed period, an RIE process is used for size reduction of the deposited SNS. Under optimized RIE conditions, a constant SNS horizontal etch rate regardless of the initial SNS size is confirmed that retains a well-defined etched SNS shape. For Si NP fabrication, MaCE is combined with the silica nanosphere lithography technique. Au catalyst layer with Ni inserted as an Au adhesion layer provides enhanced lithographic accuracy of the metal mask layer. Further, we were able to observe that the measured etch rates gradually increase as the fractional coverage of catalyst increases, and successfully estimate the etch time to produce a desired height of Si NPs with various diameters. As a result, well-

controlled Si NPs can be fabricated in a desired period and dimension on large surface area accompanied by great structure uniformity which potentially provides a powerful approach to realize enhanced optical and electrical properties of Si for practical application.

2.4. Fabrication of Various Si Micro-/Nano-Structures with Different Etching Techniques

In this section, we also discuss the potential of silica nanosphere lithography technique for various micro-/nano-scaled Si surface structures fabrication with different etching techniques like KOH solution etching and reactive-ion dry etching.

2.4.1. Inverted Pyramid: KOH Solution Etching

For the first demonstration of Si surface structure fabrication using our process, we decided to fabricate an Si inverted pyramid structure which is known to offer effective light trapping in an optimal subwavelength-scale.[19] In my thesis, we show our result of $\sim 1.1 \mu\text{m}$ scale inverted pyramid with $1.57\mu\text{m}$ period in a hexagonal array. (Note: Optically, this is not an optimal scale and density, but is intended to show our capability to control the size and density of fabricated structure.) To provide a stable masking layer on the Si surface during the KOH etch, we have chosen Cr mask layer which is reasonably robust in both BOE and KOH solutions and is a relatively inexpensive metal. 50nm Cr layer was deposited by e-beam evaporation following which the sample was dipped in BOE (10:1) solution for SS removal. For anisotropic etching of Si inverted pyramids, a 1% KOH solution was prepared after Si saturation to prevent excess Si etching and etching was done with 4% IPA addition to improve the etching uniformity. After KOH anisotropic etching for 2-min at 85°C , a well-defined inverted pyramid features was observed as shown in Figure 2.24(b) ~ (d). The pattern diameter in Figure

2.16(a) was $\sim 1.1 \mu\text{m}$, and the resulting inverted pyramid lateral dimension is also approximately $1.1 \mu\text{m}$ as shown in Figure 2.16(b).

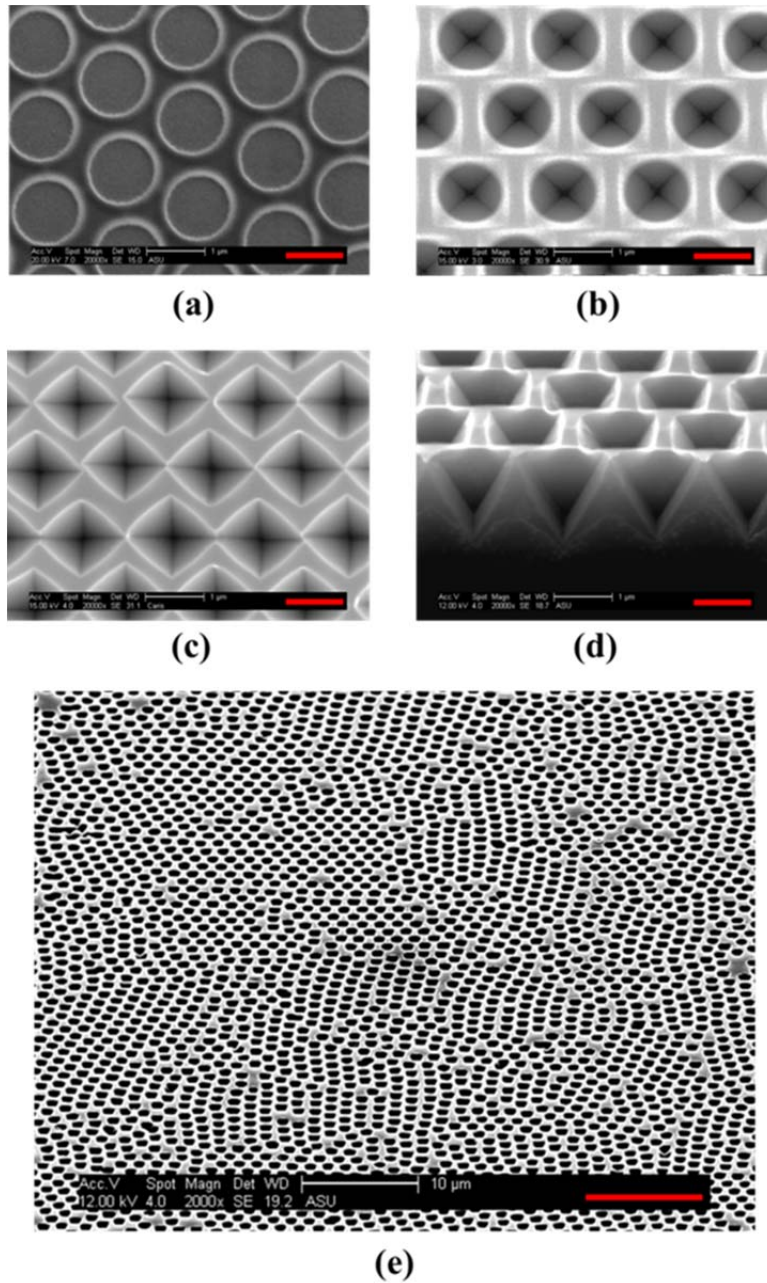


Figure 2.24. SEM images of (a) Cr deposited Si surface after SNS removal, (b) 1% KOH etched surface with Cr layer, (c) inverted Si pyramid after Cr layer removal, (d) cross-sectional image of inverted Si pyramid, and (e) fabricated inverted pyramid over large

surface area to show its uniformity (Inverted pyramid has ~10% size variation likely caused by an initial SNS size variation of 10%). Note : (a) ~ (d) scale-bar = 1 μm , and (e) scale-bar = 10 μm .

In addition, Figure 2.24(c) ~ (e) showed that our nano-fabrication process can produce highly uniform inverted pyramid structures over a large surface area with controlled size and density. Mavrokefalos, *et.al* demonstrated that the proper scale of Si surface structure can produce an absorption close to the Lambertian limit in the visible and near IR regions.[7] Therefore, future size and period optimization for SWSS will be able to produce broadband absorption enhancement for thin c-Si solar cell applications.

2.4.2. Nano-Pillar & Nano-Tip: Reactive-Ion Etching

Basically, plasma –assisted reactive ion etching (RIE) is the etching method combining physical and chemical etching which can be done by ion sputtering, and chemical reaction of radicals with target materials. The basis of RIE is simple; use a gas glow discharge to dissociate and ionize relatively stable molecules forming chemically reactive and ionic species and choose the chemistry such that these species react with the solid surface to be etched to form volatile products. The processes are taking place during RIE process have been described below,[66] and the processes are schematically illustrated in Figure. 2.25.

Generation – A glow discharge is used to generate from a suitable feed gas (e.g. SF₆ for Si etching) by electron-impact dissociation/ionization the gas phase etching

environment which consists of neutrals, electrons, photons, radicals (F^*) and positive (SF_5^+) and negative (F^-) ions.

D.C. bias formation – The Si wafer is placed on an RF driven capacitatively coupled electrode. Since the electron mobility is much greater than the ion mobility, after ignition of plasma, the electrode acquires a negative charge, i.e. the D.C. self-bias voltage.

Diffusion/forced convection – The transport of reactive intermediates from the bulk of the plasma to the Si surface occurs by diffusion. Positive ions from the glow region are forced to the substrate surface by way of the D.C. self-bias (negative) and will assist the etching.

Adsorption – Reactive radicals adsorb on the Si surface. This step can be strongly enhanced by concurrent ion bombardment which serves to produce ‘active sites’ since it aids in the removal of e.g. the SiF_x layer which otherwise passivates the Si surface.

Reaction – A reaction between the adsorbed species and the Si must take place. In the case of fluorine-based etching of Si, chemical reactions between F atoms and the surface spontaneously produces either volatile species, SiF_4 , or their precursors, SiF_x ($x < 4$). However, in Cl-based etching atoms are known to adsorb readily on Si surfaces but the spontaneous etch rate is very slow. Ion bombardment makes it possible for adsorbed Cl atoms to attack the backbones of Si more efficiently and form a volatile $SiCl_4$ molecule. This mechanism is called ion-induced RIE.

Desorption – A desorption of the reaction product into the gas phase requires that the reaction product is volatile, thus it should have a high vapor pressure at the substrate temperature. Additionally, there should be no deposited blocking film at the surface. The

removal of these films can be greatly accelerated by ion bombardment via sputtering. This mechanism is known as ion-inhibitor RIE.

Exhaust – The desorbed species diffuse from the etching surface into the bulk of the plasma and should be pumped out, otherwise plasma-induced dissociation of product molecules will occur and re-deposition can take place.

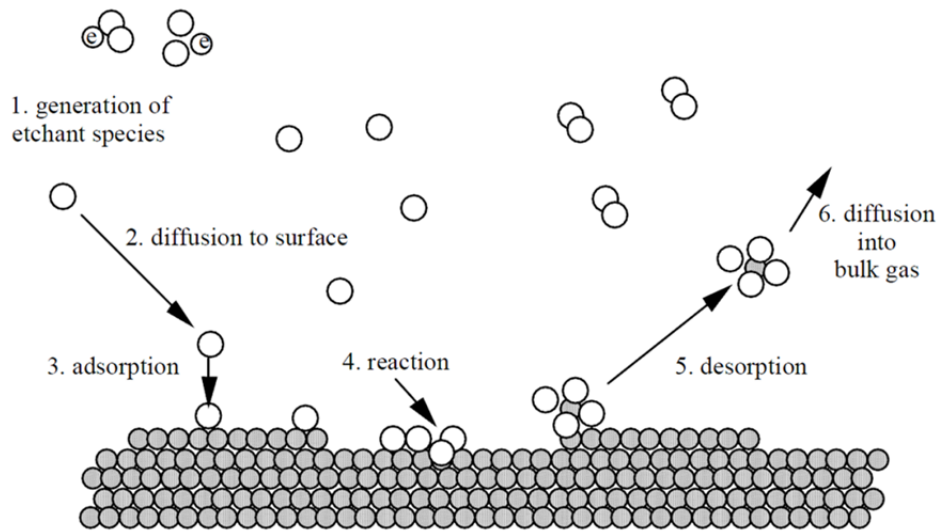


Figure 2.25. Schematic illustration of RIE process to etch solid surface.[83]

In our work, the Si surface etching was made with using two major etching elements which are chlorine (Cl) and fluorine (F). The utilization of these two etching elements based RIE process can provide more choices on the target shape of surface texture. F in plasma can offer high reaction probability with Si which is suitable for isotropic Si etching. In contrast, low reaction probability of Cl can offer highly anisotropic etching environment producing surface structure with great profile control.

Therefore, by combination of F and Cl based RIE processes under various etching conditions (e.g. gas flow rate, RF power, pressure),[66, 84] the diverse shape of nanostructures can be fabricated with relatively easy control.

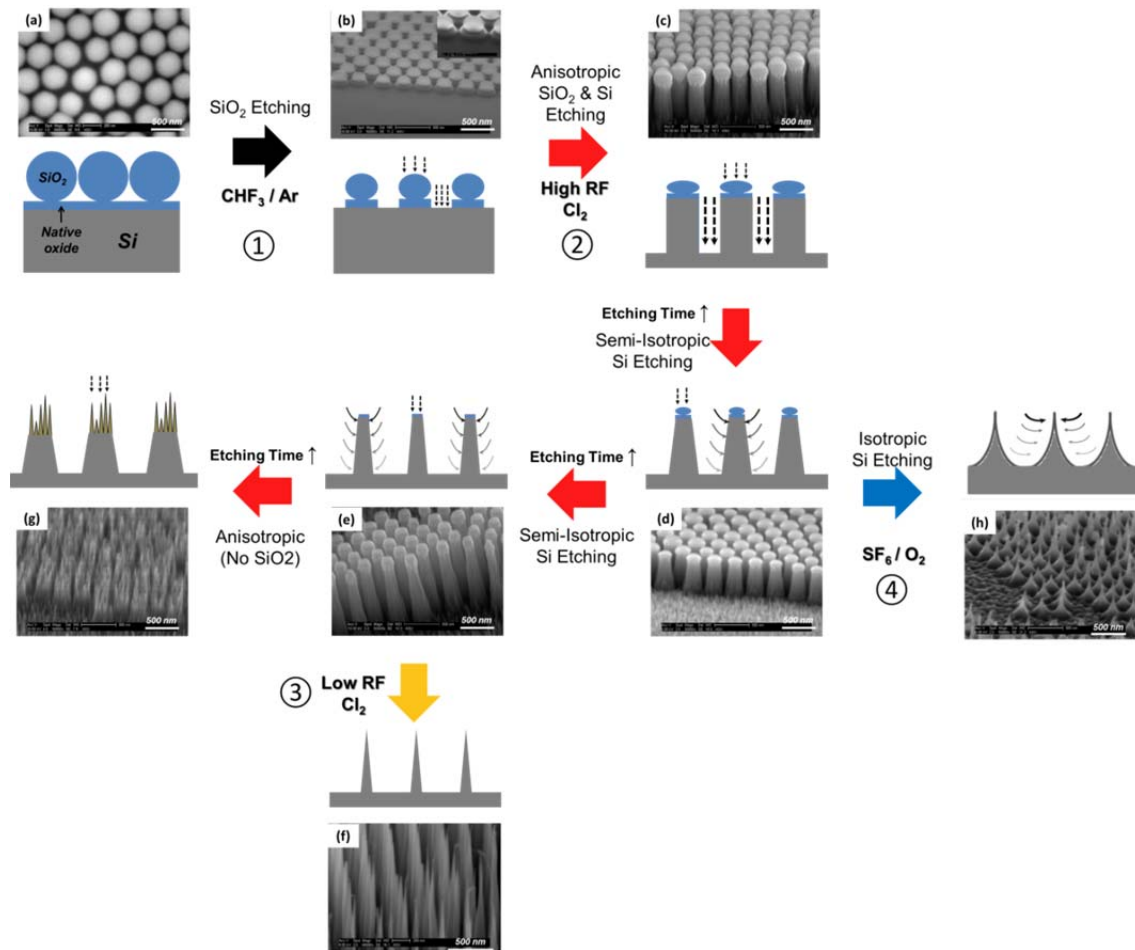


Figure 2.26. Schematic illustration and SEM images to fabricate nanopillar and various aspect-ratio nano-tip structure.

In Figure 2.26, our RIE texturing process has been illustrated with actual SEM images at each step. As shown in Figure 2.26 (b), the first etching step with ① CHF₃/Ar

gases is to reduce SNS (SiO_2) size to provide etching path for following RIE process, in addition, to determine lateral size of nanostructure. After SNS size reduction, ② Cl_2 (10sccm & 30 mTorr) etching has been made to form nanopillar structure by intensified anisotropic etching with high RF power (100 watt) as shown in Figure 2.26 (c). Under continuous ② etching, however, the increased interparticle distance between SNS on top of Si nanopillar would accelerates the etching rate of Si at top which provides weakened anisotropic etching producing varied etching rate of Si from top to bottom. With extended ② etching, SNS would be completely removed and the top of Si would be anisotropically etched to produce dual-scale nanostructure as shown in Figure 2.26 (h). If there is reduced RF power (50watt) applied under same conditions (③), then, the overall density and energy of the free electrons would be decreased which produce less negative D.C. voltage causing further weakened anisotropy and etching rate; consequently, the super-sharp nano-tip structure can be fabricated as shown in Figure 2.26 (f). However, from Figure 2.26 (g), if low-aspect ratio nanotip structure should be made, we can change gas from Cl_2 to SF_6/O_2 which can provide intensified isotropic etching. (Note: SF_6 etching is quite drastic, so should be operated for short period to prevent complete destruction of texturing). Therefore, the RIE processes with F and Cl based gases can offer excellent control on Si etching directionality and selectivity to fabricate various desired Si nanostructures.

Chapter 3

OPTICAL SIMULATION FOR SI NANOPILLARS

3.1. Background

3.1.1. Motivation

As briefly mentioned in the introduction, c-Si is an indirect bandgap material which has a low absorption coefficient especially for long wavelength region (or near-infrared region). For example, the absorption length will be increased from 10 μm to about 3 mm in the wavelength range 700 ~ 1100 nm, but this long wavelength region includes about 41% of photons with energies above the bandgap (E_g) of Si.[20, 85] Therefore, appropriate optical architecture must be designed for effective light absorption from long wavelength region to realize high efficiency thin c-Si solar cell fabrication.

In many previous reports, enhanced light absorption with 2-D periodic arrayed nanostructure has successfully demonstrated computationally and experimentally.[86-91] This increased light absorption with periodically arrayed nanostructures is attributed to (1) enhanced anti-reflection (AR) effect from gradual refractive index change or enhanced photonic behavior for downshifting within nanostructured layer,[92, 93] and (2) increased fraction of high order transmitted light diffraction.[20, 94] From both of these effects, highly increased light absorption will be expected by suppressed surface reflection and increased light path-length in the absorber. However, regardless of their great potential for enhanced light absorption, their complicated surface geometries including densely packed and high aspect-ratio nanostructure followed by large surface area enlargement

have been main barriers for realistic nanostructure for thin c-Si solar cell application. Therefore, the complexity of surface geometry must be considered along with optical property of Si nanostructure.

Therefore, in this chapter, we will investigate the optical properties of Si NPs in two-dimensional (2-D) periodic hexagonal array fabricated in various geometric conditions including height, diameter, and period as schematically illustrated in Figure 3.1(a) which can be fabricated by our nano-fabrication process as shown in Chapter 2. The optical properties of Si NP array are calculated with two different optical modeling techniques which are rigorous coupled wave analysis (RCWA) and finite-difference time-domain (FDTD) and methods. RCWA is used to provide a full wavelength-scaled analysis for incident light scattering behavior and transmitted light diffraction efficiency, and combination with FDTD successfully provides well-visualized understanding on overall incident light behavior in different NP conditions. By using these two different techniques, the optimal geometric conditions of Si NP array for thin c-Si solar cell will be determined based on effectiveness of resonant scattering in forward direction and magnitude of transmitted light diffraction at high orders ($> 0^{\text{th}}$ order) as schematically illustrated in Figure 3.1 (b) - (1) and (2), respectively. [93, 94]

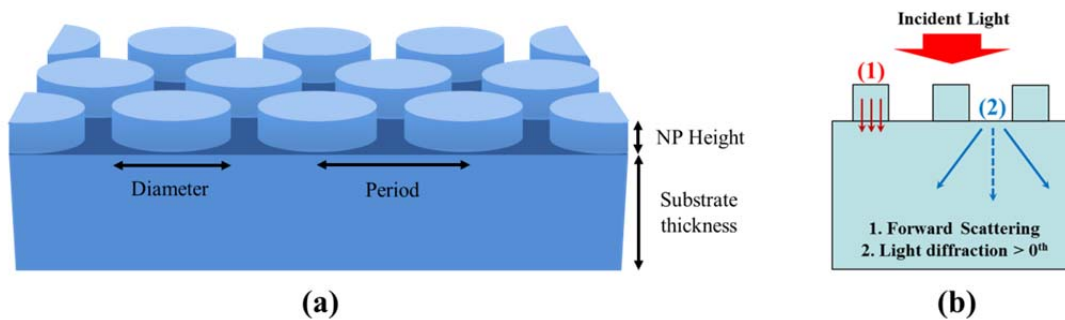


Figure 3.1. (a) Schematic illustration of simulated Si NP, and (b) investigated optical properties of Si NPs arrayed in 2-D hexagonal formation; (1) forward scattering for reduced front surface reflection loss, and (2) light diffraction order for enhanced light absorption of transmitted light in the absorber.

3.1.2. Rigorous Coupled Wave Analysis (RCWA)

Here for my thesis, RCWA method is used as a main optical modeling technique to analyze the optical properties of Si NP array due to its less time consuming calculation process to understand full wavelength-scaled reflection and transmission in addition to its effectiveness to calculate the diffraction efficiency.

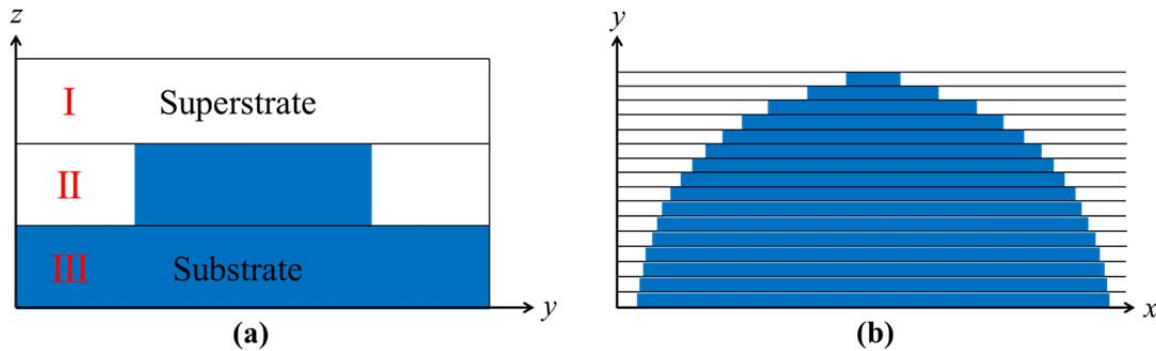


Figure 3.2. Constructed structure to solve a diffraction problem using RCWA. (a) Structure is divided into strata so that each stratum is homogeneous in the z-direction, and (b) horizontally divided strata so that each stratum is homogeneous in the y-direction for circular-shaped structure calculation.

RCWA is a well-known optical simulation technique to calculate the diffraction behaviors from a periodically arrayed structure. [95-98] Basically, RCWA aims to solve the equations of light propagation from a homogeneous superstrate through a periodic medium to a homogeneous substrate as illustrated in Figure. 3.2, RCWA requires that

region II in Figure 3.2 (a) is homogeneous in the z-direction. For circular shaped structure, due to limitation of RCWA for angled shape, the structure is also divided into y-direction as shown in Figure 3.2 (b). The further theoretical details are shown in reference [99].

Here for my thesis, the commercial software package (GD-Calc), which runs in MATLAB environment, is used for the RCWA simulations. Incident light was considered to be randomly polarized by averaging transverse magnetic (TM) and transverse electric (TE) polarizations.

3.1.3. Finite Difference Time Domain (FDTD)

FDTD is a numerical method where the Maxwell equations are solved by discretizing time and space.[100] The spatial discretization utilizes a Yee lattice where the E and H field are stored at intermediate positions to reduce the memory consumption. The E and H field are then solved in discrete time intervals within the Yee lattice using the Maxwell equations in partial differential form. The time resolution is usually directly related to the spatial resolution. FDTD does not require the structure to be periodic, but periodic, or Bloch wave, boundary conditions may be applied for simulations of waves in periodic media. The source in an FDTD simulation is an electromagnetic pulse with a given frequency and duration. The FDTD software computes the E and H field at every time step until the magnitude of a chosen field component at a given detector position reaches a certain threshold value. A short pulse length in the temporal domain will result in a broadening of the frequency spectrum, i.e. one pulse consists of an extended range of

frequencies centered on a mean frequency. The response at the detectors may be Fourier transformed to get spectrally resolved reflection and transmission. In other words, the response at all frequencies may be computed in only one run. Further details are shown in reference [101].

Here, I used FDTD to visualize the scattering behavior for Si NP array fabricated in various geometric conditions to confirm the results of RCWA.

3.2. Design of Si Nanopillar Array with Optical Simulation

3.2.1. Period of Si NPs: Statistical coupled-mode theory (SCMT)

Before we study the specific optical properties of Si NPs with simulation, the grating period, L , must be determined to accomplish high absorption enhancement over a broad spectrum range. In previous reports by Yu *et.al*, [102, 103] the effect of period is well explained with “statistical coupled-mode theory” based on the number of guided resonance in a free space and number of resonant channels with incident wavelength.

From the theory, the absorption enhancement factor, F , can reach beyond the bulk-limit, $4n^2$, when the normalized frequency, $s = L / \lambda$, is comparable or smaller than “1” which indicates that the period, L , must be comparable or smaller than incident λ . Based on theory, in case of hexagonal arrayed grating structure, absorption enhancement beyond bulk-limit, $4n^2$, when “ s ” lies between 0.6 and 1.1 as shown in Figure 3.4 below.

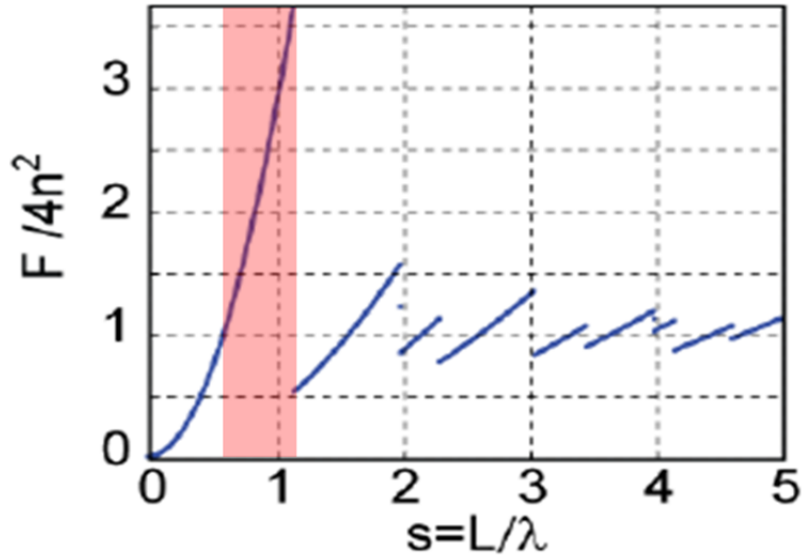


Figure 3.3. Upper limit of absorption enhancement for a grating with hexagonal lattice periodic structure. Reprinted from Reference [102]

Therefore, if target wavelength region for absorption enhancement is chosen, the period also can be decided based on that wavelength region. In this thesis, our target region is longer wavelength since the nano-fabrication process has been developed for thin-film Si solar cell application which inevitably produces large fraction of light loss in longer wavelength region. Based on this reason, our target spectral area is 600 to 1100 nm where requires effective light trapping for absorption enhancement; in a consequence, for our periodic Si NPs in hexagonal array, 600nm grating period ($L = 600\text{nm}$) is chosen which provides normalized frequency range of $0.54 < s < 1.0$ for 600 ~ 1100nm wavelength region.

3.2.2. Height and Si FF of Si NPs

In case of statistical coupled-mode theory, it assumes that the layer with periodic grating structure is placed at back surface, Figure 3.4 (a), with perfect mirror condition. The theory doesn't account for any front surface reflection since it only focuses on the relation between the number of guided resonances and channel numbers, not the light interaction between incident light and absorber. However, this is not what actually happens in reality. For periodic grating structure for practical application, the light interaction with absorber and/or interference among scattered light also must be under control or induce in a desired way to realize maximum light absorption within reduced volume of absorber. In addition to period, therefore, the individual dimension of grating structure also must be manipulated in an intended scale. From Figure 3.4 (b), our grating structure, Si NP, is illustrated which is placed on top of absorbing medium. In this case for front surface grating structure, unlike statistical coupled-mode theory, the front surface reflection, $R\%$, must be considered to achieve maximum light transmittance to the medium for its enhanced light absorption.

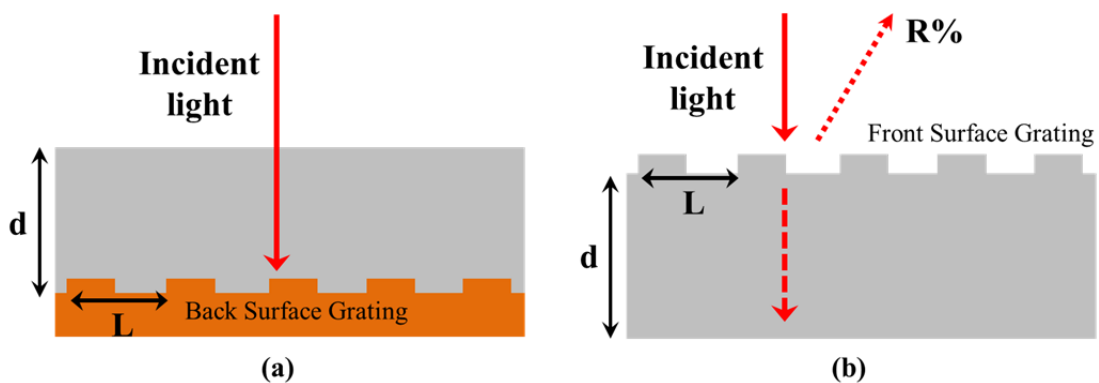


Figure 3.4. Schematic illustration of grating structured layer for (a) statistical coupled-mode theory, and for (b) our simulation.

Here, we investigate the dimension effect of Si NP arrayed at 600nm period by introducing different heights and diameters. Since dimension of standing structures at fixed period is highly crucial in terms of (1) effective confinement of resonant scattering within structure, and (2) reduced light interference between structures which are directly related to the magnitude of reflection from the structured surface.[93, 104, 105] In Figure 3.5 (a) ~ (c), the front surface reflection of Si NPs built on semi-infinite thick Si substrate is calculated with RCWA simulation with three different Si FFs (30%, 50%, and 70%), and various NP heights from 100 to 400 nm. The FF is defined by the fractional area of Si NP and each FF of 30%, 50%, and 70% FF are equivalent to 344, 444, and 520 nm in diameter, respectively. From the Figure 3.5 (a), 30% FF at 200nm Si NP height (red-line) reveals highly suppressed front surface reflection, especially in the 600nm ~ 1100nm wavelength range compared to other aspect-ratio Si NPs. However, even with same height, as FF increases, overall reflection from front surface increases. In Figure 3.5 (d), the weighted reflection are shown separately for short (300 ~ 600nm) and long (600 ~ 1100nm) λ region in different NP heights and FFs. From the Figure 3.5 (d), for long λ region, the front surface reflection can be very effectively suppressed for both of 30% and 50% FFs at 200nm height, but 30% FF can also provide enhanced AR effective to suppress reflection from short λ region compared to 50%.

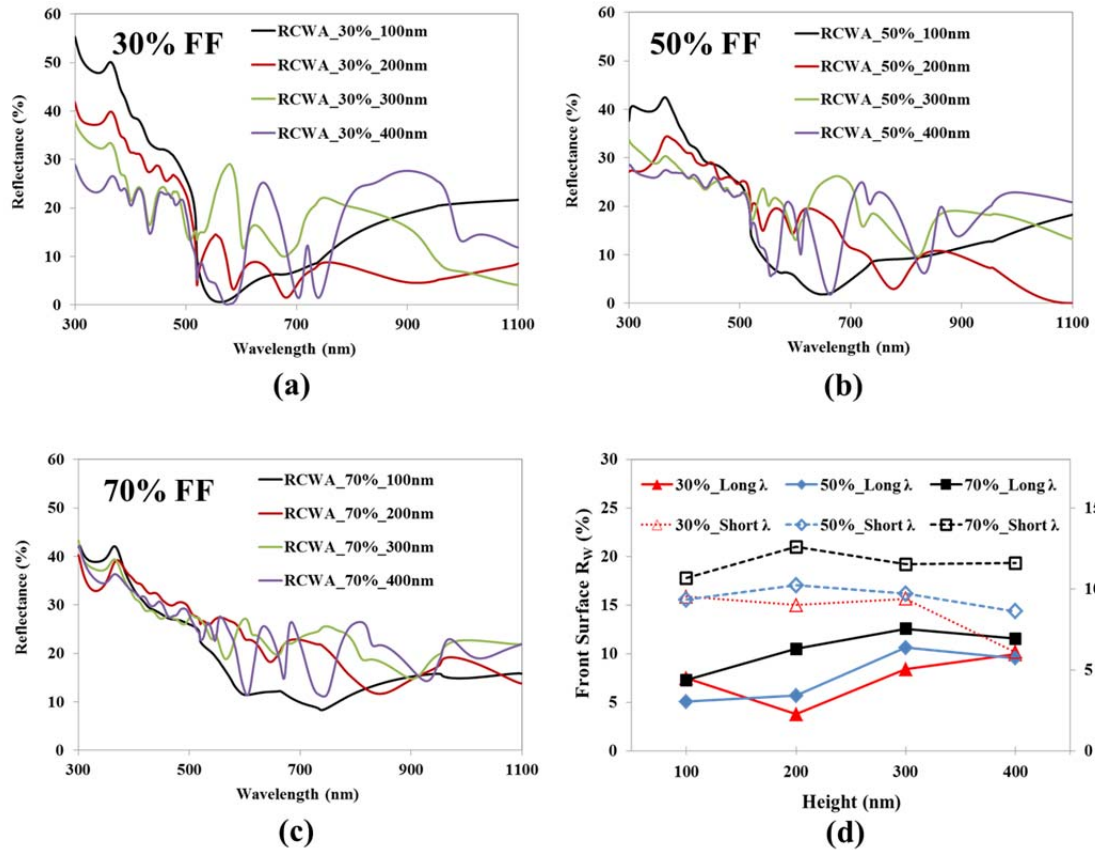


Figure 3.5. RCWA results for front surface reflections from three different Si FFs, (a) 30%, (b) 50%, and (c) 70% representing 344, 444, and 520 nm Si NP diameters, respectively, and the height range is from 100 to 400nm with 100nm interval. In addition, (d) reflection trends for short (300~600nm) and long (600 ~ 1100nm) λ are shown with different NP heights in weighted reflectance. (Note: Period is fixed at 600nm)

Therefore, well-optimize Si NP in volume represented by Si FF (NP diameter) and height can produce suppressed reflection despite of its low-aspect ratio. Typically, the AR effect gets intensified with higher aspect-ratio of nanostructure, so this highly suppressed reflection at lower aspect-ratio (30% FF at 200nm height) compared to other high aspect-ratio Si NPs cannot be explained only with AR effect of NP.

To understand the resonant scattering behavior with various Si NP dimensions, FDTD simulation also has been performed due to its effectiveness to analyze certain optical phenomena with visualized results. In Figure 3.6, height effect has been simulated at 30% fixed Si FF (344nm in diameter) with 900nm incident λ .

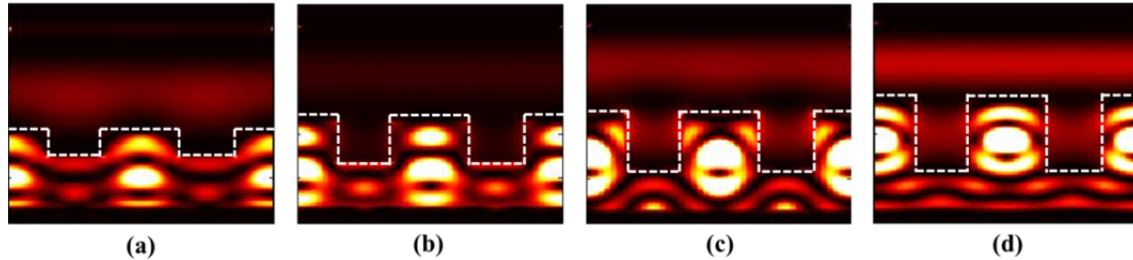


Figure 3.6. Incident light scattering behavior ($\lambda = 900\text{nm}$) with various heights; (a) 100nm, (b) 200nm, (c) 300nm, and (d) 400nm at 30% fixed Si FF

From the results, as the increases from 100nm to 200nm, highly well-confined scattering behavior is observed within 200nm NP. In addition, the magnitude of scattering is also stronger at 200nm compared to 100nm NP. However, in case of taller NPs, 300nm and 400nm, even though stronger intensity of scattering within NPs is still observed, we also found that confinement of light scattering within NP is getting weakened with these taller NPs which can attribute to scattered light interference inside NPs is also getting significant due to increased density of state with taller Si NP. [106] As a result, electric field distribution above the structured surface is getting noticeable indicating large fraction of back reflection occurred with taller NP above 200nm. Furthermore, the increased intensity of electric field between NPs taller than 200nm represents the weakened confinement effect for resonant scattering with taller NPs due to

excess scattered light interference. From the same reason, in Figure 3.7, we also observe that increased back reflection as NP FF (or diameter) increases from 30% to 70%. However, in case of diameter, because of increased NP volume to lateral direction, the interferences are also getting dominant horizontally.

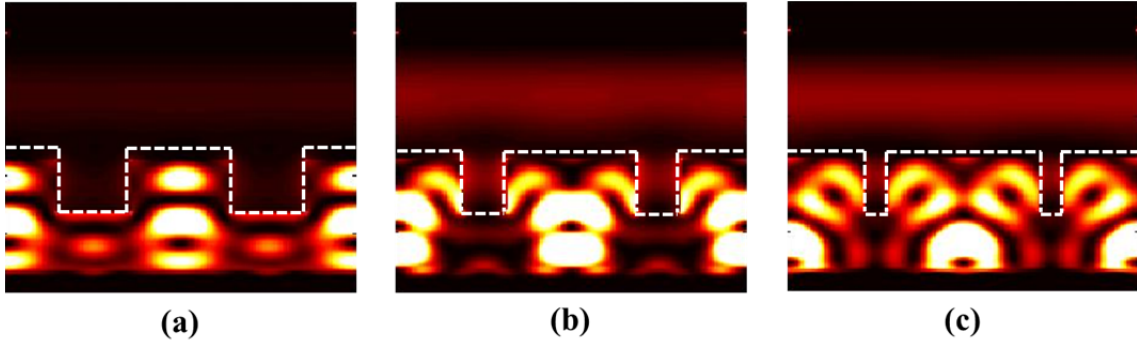


Figure 3.7. Incident light scattering behavior ($\lambda = 900\text{nm}$) with various Si FF; (a) 30%, (b) 50%, (c) 70% at 200nm fixed height

These increased light interferences are confirmed by Figure 3.8 (a) and (b) which shows red-shifting of front surface reflection as FF (or diameter, at 100nm height) and height (at 70% FF) increases. We know that downshifting of light is natural phenomenon with secondary light scattering (or interference).

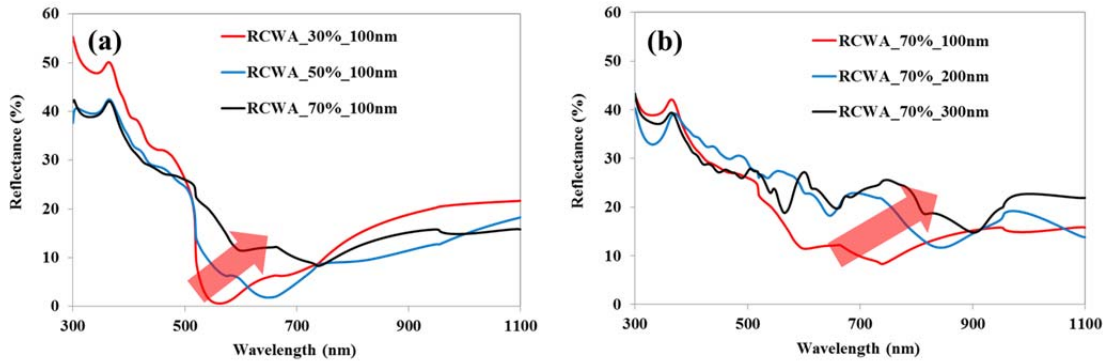


Figure 3.8. Red-shifting of front surface reflection as (a) FF (or diameter, at 100nm height) and (b) height (at 70% FF) increases.

From the RCWA and FDTD simulations, it is very obvious that well-defined NP dimension is highly crucial to produce effective incident light confinement within the NP volume producing maximum light transmittance to the medium for absorption. From the simulations, we found that, for 600nm period, the 200nm height and 30% FF (344nm in diameter) are the desired Si NP dimensions in our conditions.

3.2.3. Diffraction Efficiency of Transmitted Light

From previous sections, we mostly focused on the light scattering behavior on front surface with various aspect-ratio Si NPs to produce suppressed front surface reflection. In this section, the grating effect of Si NP will be studied for large fraction of high order transmitted light diffraction. As illustrated in Figure 3.9, the effective light absorption in the longer λ region requires reduction on both of front and back surface reflection. For maximum light absorption in the longer λ region, the transmitted light path-length must be increased due to dramatically increased absorption length of light in longer λ region as discussed in the introduction.

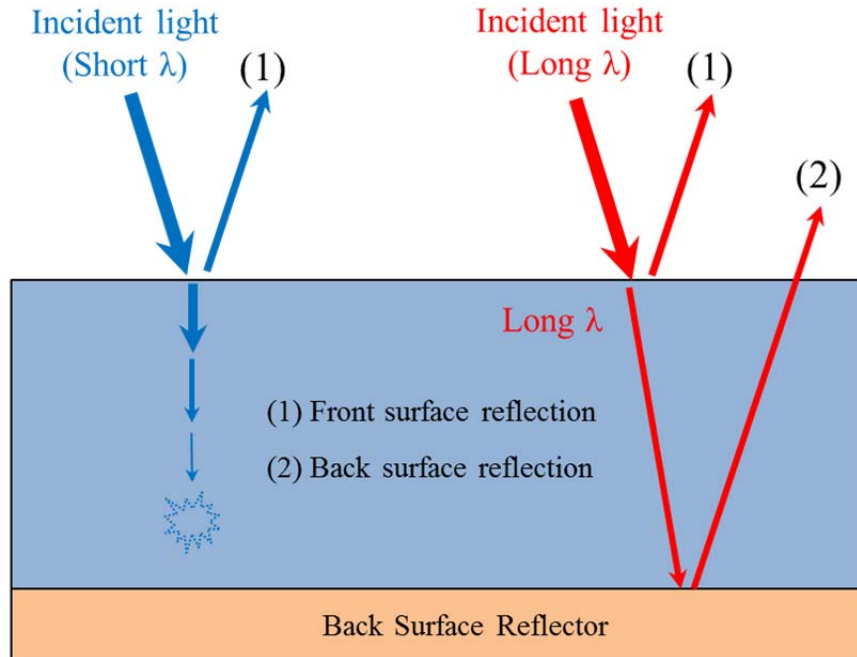


Figure 3.9. Schematic illustration of light loss mechanisms for incident light in short (blue arrow), and long (red arrow) wavelength region

With plain Si surface or large-scale surface structures larger than incident wavelength, 0th order transmitted light diffraction is dominant due to no or weak grating effect with those surface geometric conditions. In Figure 3.10 (a), it is shown that bare Si surface produce no specific direction of transmitted light scattering and Figure 3.10 (b) shows that total transmitted light is transmitted to Si substrate with 0th order diffraction which is just normal to the incident surface. Therefore, the transmitted light path-length for absorption will have its shortest; in a consequence, large back-surface reflection loss will be un-avoidable as illustrated in Figure 3.9 with red arrow (2).

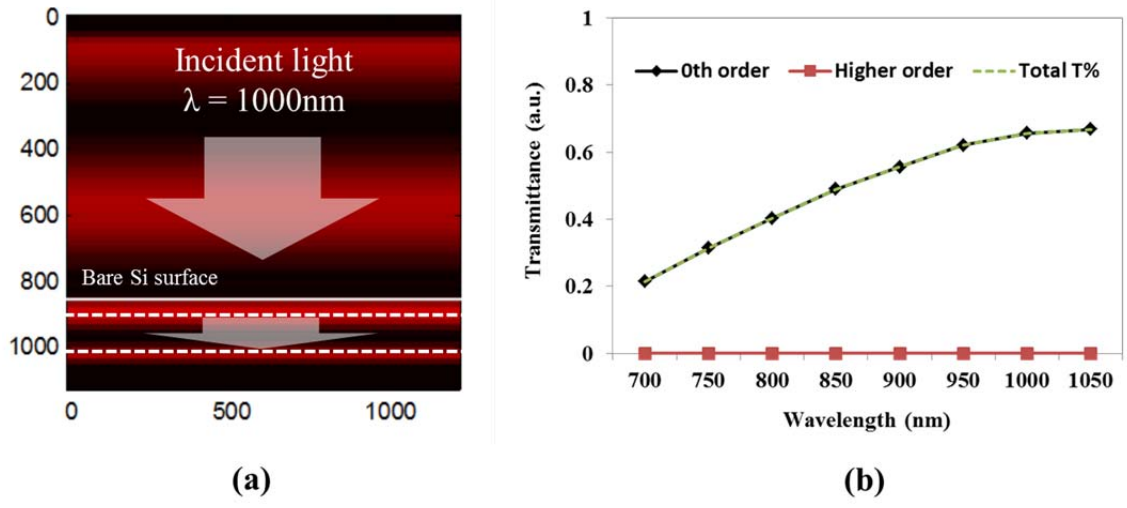


Figure 3.10. Optical simulation for transmitted light orientation with (a) FDTD ($\lambda = 1000\text{nm}$), and (b) RCWA

Here, fractional diffraction efficiency at higher order above 0^{th} with 2-D hexagonal arrayed Si NPs is calculated with RCWA for same NP conditions from Figure 3.5. This calculation is done to investigate grating effect of each NP to produce large fraction of high order transmitted light diffraction as illustrated in Figure 3.11.

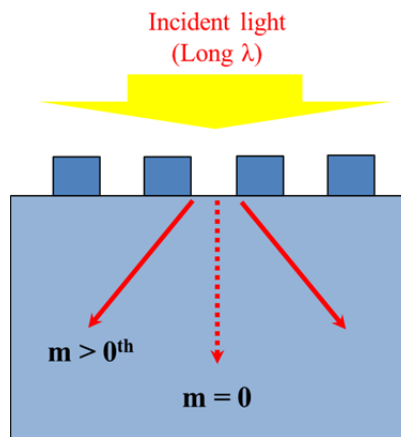


Figure 3.11. Schematic illustration of grating effect with Si NP to produce high order transmitted light diffraction

In Figure 3.12, along with enhanced forward scattering of 30% FF, Si NP in 30% FF also produces larger fraction of transmitted light diffraction above 0th order compared to 50%, and 70% FF. The overall decrease of high order diffraction with larger diameter can be attributed to reduced amount of total transmitted light from longer λ as shown in Figure 3.5 (d) with solid-line. The height effect on high order diffraction can be explained by light inferences after resonant scattering. For instance, in Figure 3.12 (a) for 30% FF, the overall increase of high order diffraction from 100 nm to 200nm is originated from stronger scattering producing no or insignificant light interferences as shown in Figure 3.6 (b). However, with 300nm NP height, we observed that 700 ~ 900 nm λ has reduced high order diffraction in contrast to spectral region above 900nm showing increased fraction of high order diffraction. As shown in Figure 3.6(c), dominant direction of scattered light is forward direction to the substrate which indicates that red-shifted incident λ after scattering is involved in increased high order diffraction; in a consequence, imbalance in high order diffraction over the spectral range is produced. In case of 400nm NP, as shown in Figure 3.5(a), for 400nm, there is highly increased front surface reflection in 700 ~ 1100nm λ since excess light interferences are occurred within 400nm NP producing intensified back scattering. From Figure 3.6 (d), increased back scattering within NP is shown as height increases from 300nm to 400nm producing more surface reflection of red-shifted incident λ . It is clear that larger Si NPs generally produce reduced fraction of high order diffraction which indicates its weakened grating effect with large FF of Si NP array.

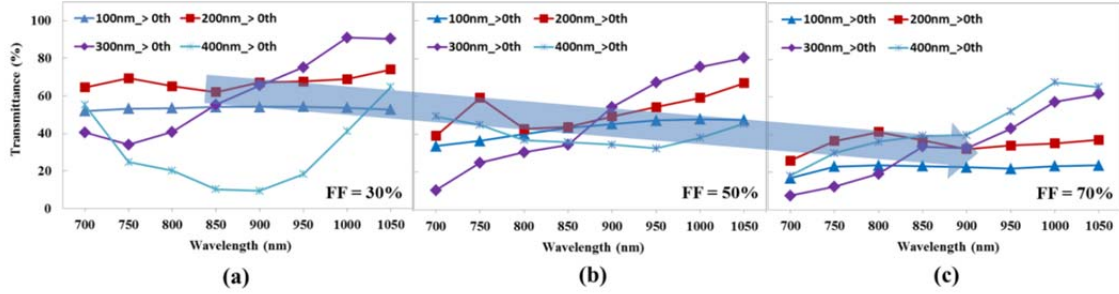


Figure 3.12. Fraction of high order ($>0^{\text{th}}$) transmitted light diffraction with (a) 30%, (b) 50%, and (c) 70% Si FF at various height from 100nm to 400nm

This weakened grating effect is because even though the period is fixed at 600nm, larger diameter (or FF) of Si NP provides increased volume for light scattering which produces more light loss from the surface by scattered light interferences which we already discussed in Figure 3.7. In Figure 3.12, the total T% with 1 μm thick Si substrate with 30%, 50%, and 70% FF of Si NP arrays is calculated and as FF increases, the fraction of transmitted light is decreased which is because of increased back scattering. Therefore, along with highly increased transmitted light, 30% FF & 200nm also provide most effective NP dimension to produce high order light diffraction in the absorbing medium, Si.

3.2.4. Absorption Enhancement of Si NP array

The absorption with Si NP arrayed 5 μm thick Si substrate is also calculated with ideal NP conditions (30% FF, 200nm height at 600nm period) which compares with bare Si surface. In Figure 3.13, from the comparison with bare Si surface representing $L \gg \lambda$, Si NP arrayed Si surface (L is comparable or slightly smaller than incident λ) offers

highly enhanced light absorption right above 580nm to 1100nm. This spectral region is where we plan to increase absorption with 600nm period based on “statistical coupled-mode theory” in the beginning of this chapter.

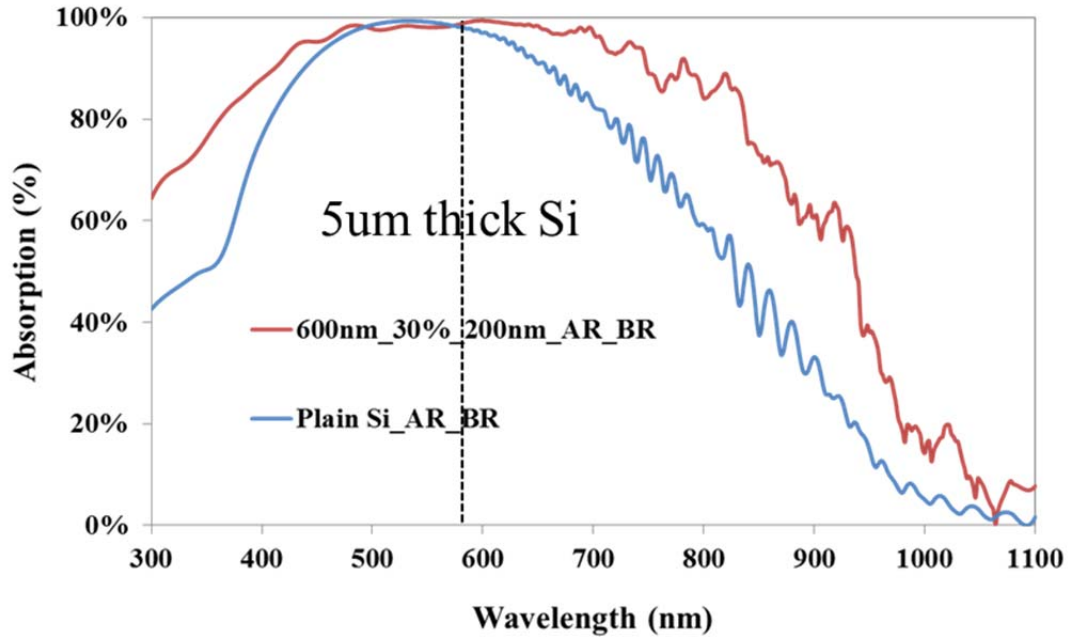


Figure 3.13. RCWA results for reflection of Si NP fabricated at 30% FF, 200nm height and 600nm period and reference reflection from bare Si surface (5 μm thick Si substrate). Both surfaces have back reflector (BR, 200nm in perfect mirror condition) and front anti-reflection layer (AR, 70nm SiN_x).

Therefore, for highly enhance light absorption with periodically arrayed grating structure on the front surface, having optimal scale of diameter and height is also highly crucial to produce light absorption in the interest spectral region.

3.2.5. Summary

In conclusion, from the RCWA and FDTD optical modeling, we found that 600nm period, 30% FF, and 200nm height are the most ideal geometric condition for Si NPs arrayed in 2-D hexagonal formation. This is because this physical condition of Si NP produces significantly suppressed front surface reflection and most enhanced grating effect for enhanced light absorption especially for the longer λ region where requires highly increased absorption length compared to shorter λ ; in a consequence, the NP array in this dimension at 600nm period can provide great potential for thin c-Si solar cell application.

In addition, the simplicity of surface geometry of our Si NP potentially offer a lower barrier to fabricate high efficiency nanostructure thin Si solar cell since it provides improved compatibility with conventional device fabrication process which are for effect surface passivation, AR coating, and electrode contact.

Chapter. 4

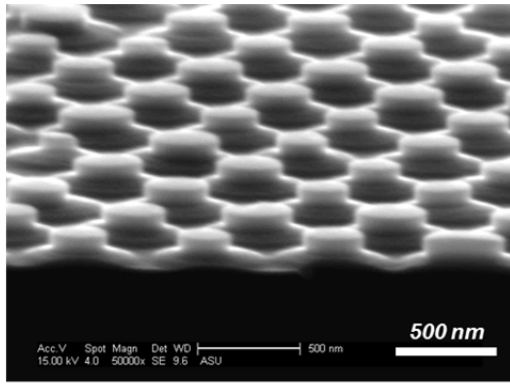
FABRICATED SI NP BASED ON OPTICAL MODELING

In previous chapter, RCWA and FDTD optical simulations had been performed to find the ideal geometric conditions for Si NP array which is potentially applicable for high efficiency thin Si solar cell. In chapter 2, we also demonstrated that our capability to produce Si NP in various periods and dimension arrayed at hexagonal formation with enhanced lithographical accuracy. Therefore, in this section, comparison between experimental and computational results for Si NPs will be made to show the accuracy of our nano-lithography and nano-fabrication process to realize control period and dimension of Si NP to produce simulated optical property.

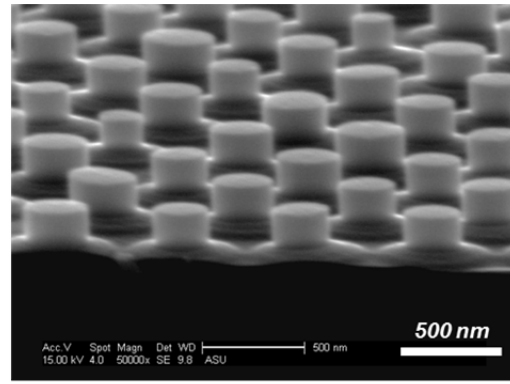
4.1. Demonstration of Simulated Si NPs

4.1.1. Fabricated Si NP vs. Simulated Si NP

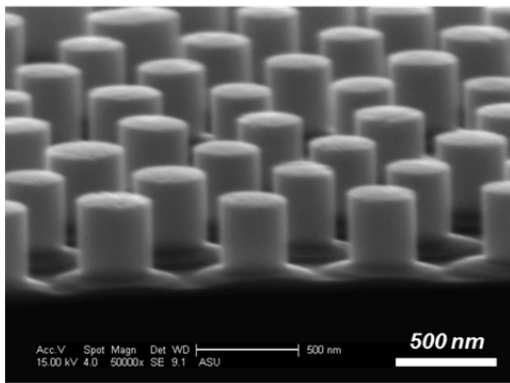
The simulated Si NPs in Chapter 3 are experimentally fabricated with SNS lithography technique after combined with MaCE process which we already showed in Chapter 2. For comparison of computational and experimental results, 600nm period and 30% FF of Si NPs are fabricated and the reflectance trend has been studied for various heights to confirm the effectiveness of low aspect-ratio Si NP to suppress the surface reflection. In Figure 4.1, the fabricated Si NPs (600nm period, 30% FF) are shown for various heights from 100nm to 400nm.



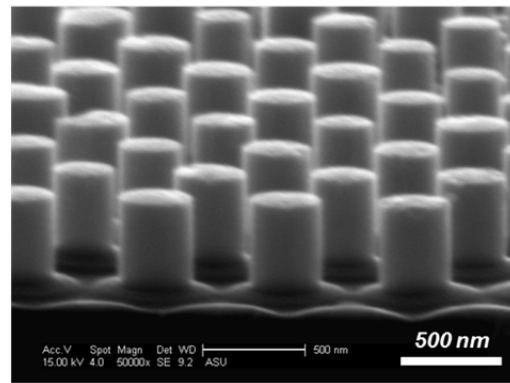
(a)



(b)



(c)



(d)

Figure 4.1. Fabricated 30% FF Si NPs in 600nm periodic hexagonal array approximately for (a) 100nm, (b) 200nm, (c) 300nm, and (d) 400nm heights

After Si NP fabrication, deposited Au catalyst layer (30nm) is removed by dipping the samples in gold etchant solution to measure accurate reflection (R%) from Si NP fabricated Si surfaces. In Figure 4.2, the measured surface R% is shown and from the results, it is clear that 200nm Si NP (red-line) produces the lowest surface R% compared to others. This suppressed R% with 200nm height at 600nm period and 30% FF is well matched with previous computational result as shown in Figure 3.6 (a).

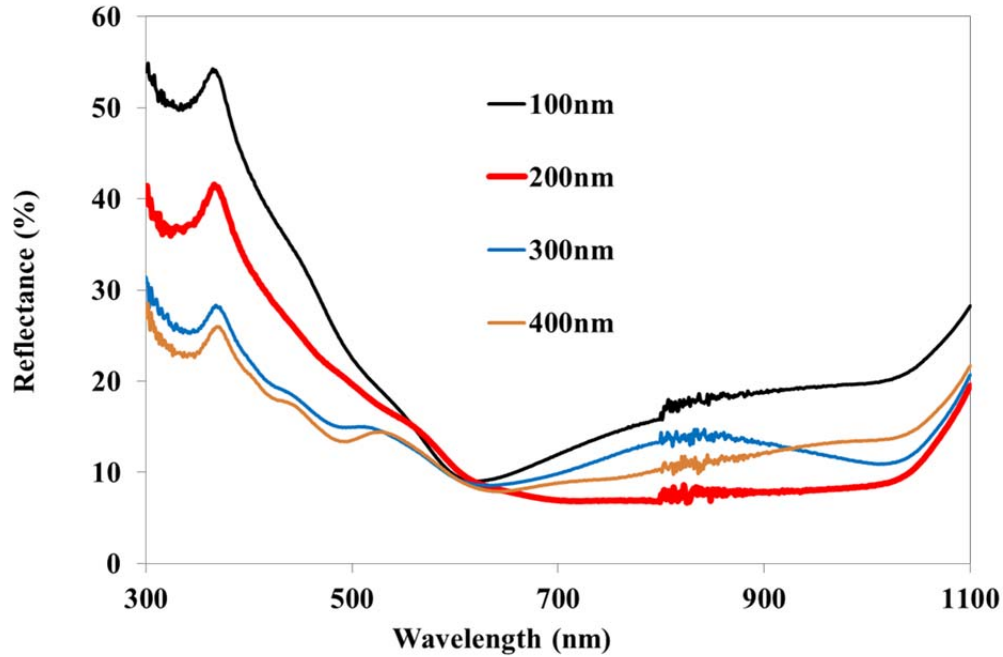


Figure 4.2. Measured reflectance of Si NPs at different heights

The surface reflection from fabricated Si NPs is also compared with optical modeling results as shown in Figure 4.3. From the Figure 4.3 (a) and (b) for 100 and 200nm NP heights, pretty well-agreed reflection behaviors are obtained, but with 300 and 400nm heights, there is noticeable increased mismatch between measured and calculated results. We believe that this mismatch is because as height increases, the light scattering with Si NP gets complicated due to significantly increased light interference as shown in Figure 3.6; in a consequence, accurate optical simulation for taller Si NP array is more challenging.

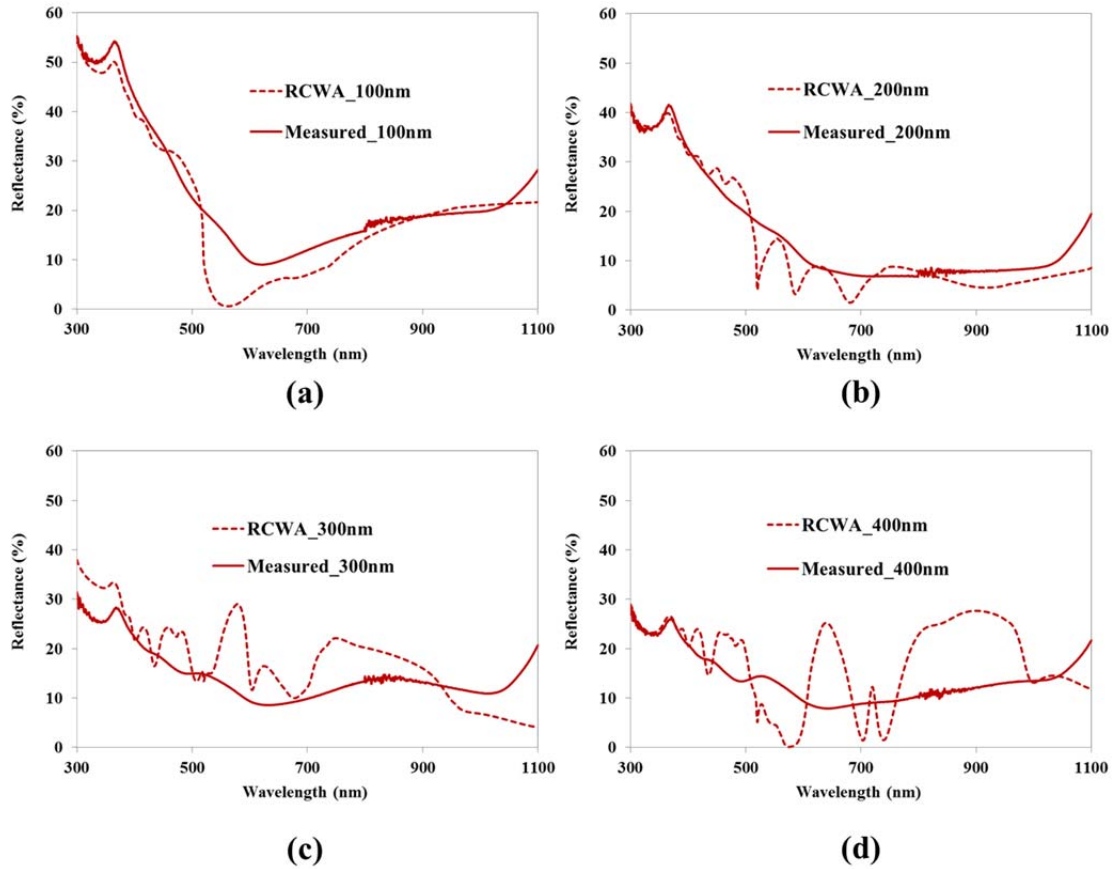


Figure 4.3. Comparison of surface reflection between computational (RCWA, dash-line) and measured (Measured, solid-line) reflection for (a) 100nm, (b) 200nm, (c) 300nm, and (d) 400nm Si NP heights (Measured Si substrate thickness = 280 μm and RCWA simulated Si substrate thickness = semi-infinite)

However, despite the some mismatch with higher aspect-ratio Si NPs between calculated and measured reflection, the overall reflection trend is pretty well matched between them. In Figure 4.4, we compare the trend of weighted reflection, R_w , for whole (300 ~ 1100nm), short (300 ~ 600nm) and long (600 ~ 1100nm) λ region between measured and RCWA simulated results.

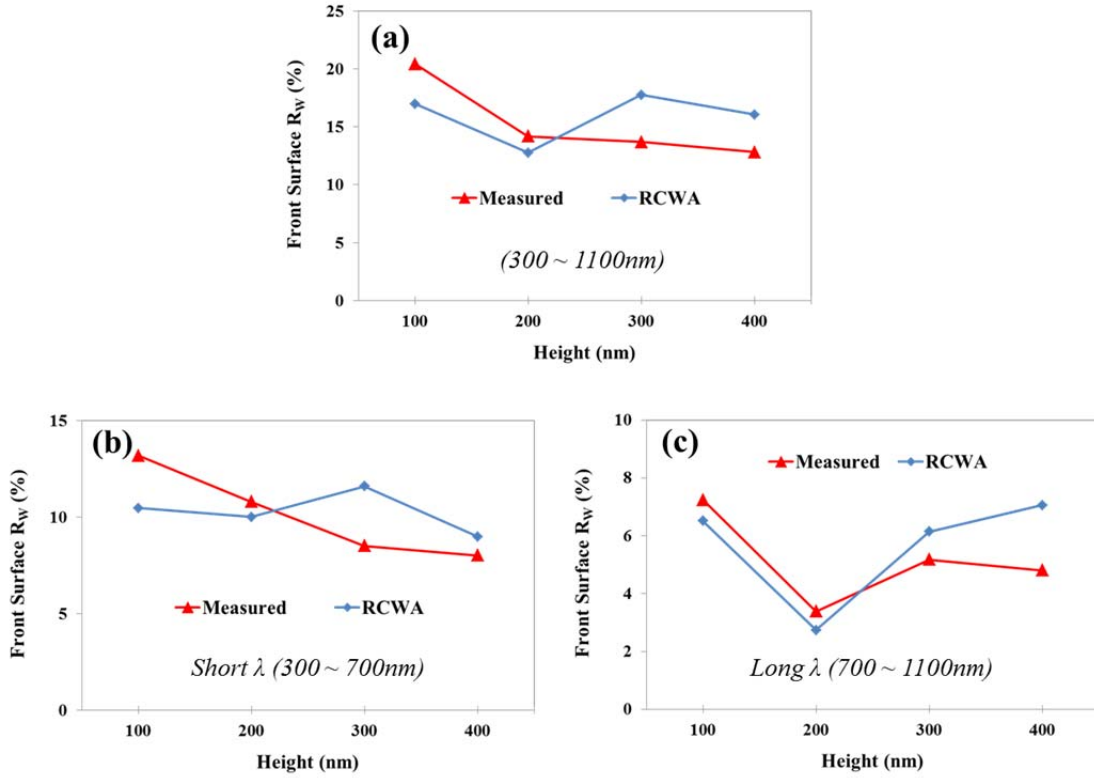


Figure 4.4. Comparison of measured (Red solid-triangle) and RCWA simulated (blue solid-diamond) weighted reflection change for (a) whole wavelength range (300 ~ 1100nm), (b) short (300 ~ 700nm) and (c) long (700 ~ 1100nm) λ region with increasing Si NP height

From Figure 4.4 (a), the whole wavelength range from 300nm to 1100nm, as we observed from Figure 4.3, the trend of R_W starts to be mismatched with Si NPs taller than 200nm. The measured R_W keeps decreasing as height increases but the RCWA simulated R_W reveals the highest R_W for 300nm and the lowest for 400nm height. From Figure 4.4 (b) and (c) for short and long λ region R_W , the short λ region is the problematic region to cause this R_W mismatch since the long λ region produces quite well-agreed trend between two results. We believe that this R_W mismatch for short λ can be attributed to increased structure damage for taller Si NPs. In Figure 4.6, the damage on Si NP is shown in red-

circle. Most probably, this physical damage but in small-scale can increase the number of light scattering for short λ on the nanostructured Si surface and provide improved AR effect for short λ region which can explain the reduced surface reflection with taller Si NPs.

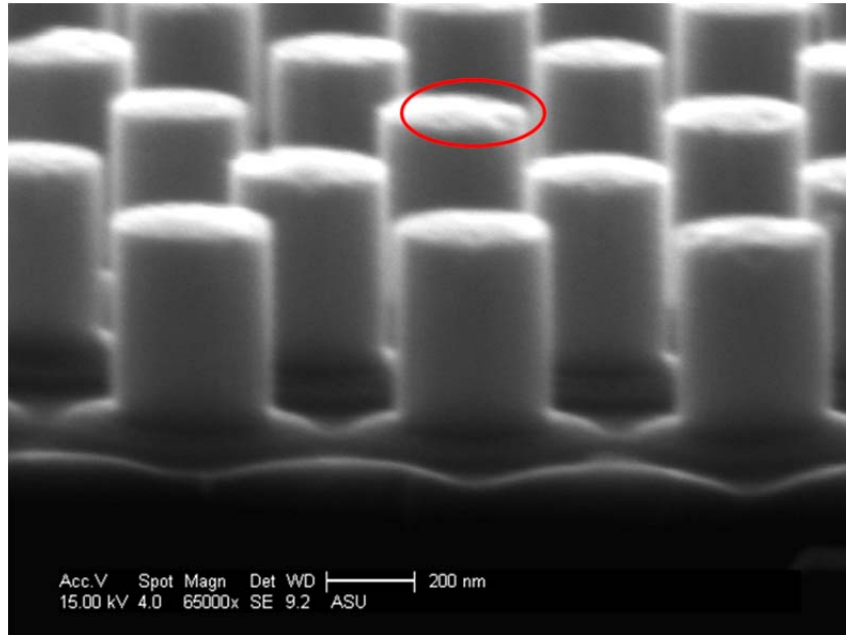


Figure 4.5. Example of structural damage on top of 400nm Si NP in red-circle

However, regardless of some optical property mismatch for higher aspect-ratio Si NPs, we still can state that 200nm height at 30% FF in 600nm period can provide the most reduced surface reflection especially for long λ region. Even though significant amount of light loss can be expected for short λ region with this Si NP, effective AR coating (i.e., SiN_x) might be achieved due to its low aspect-ratio and less densely packed Si NP array for further suppression of surface reflection including short λ region. Therefore, further optimization for AR layer deposition on this Si NPs will offer greatly improved absorption for thin c-Si solar cell application.

4.1.2. Si NP vs. Conventional KOH Pyramid

To confirm the increased light absorption of geometrically optimized Si NP array, the surface reflection from our Si NP array and conventional KOH random pyramid is made as shown in Figure 4.6. The KOH pyramid is chosen since it can represent the surface structure from conventional ray-optic approach having $L \gg \lambda$. If it is true that our optimal Si NP array fabricated in 600nm can provide enhanced light absorption beyond bulk-limit, $4n^2$, for 600nm ~ 1100nm spectral range where we plan initially, the surface reflection from Si NP arrayed surface must be lower than KOH pyramid textured surface.

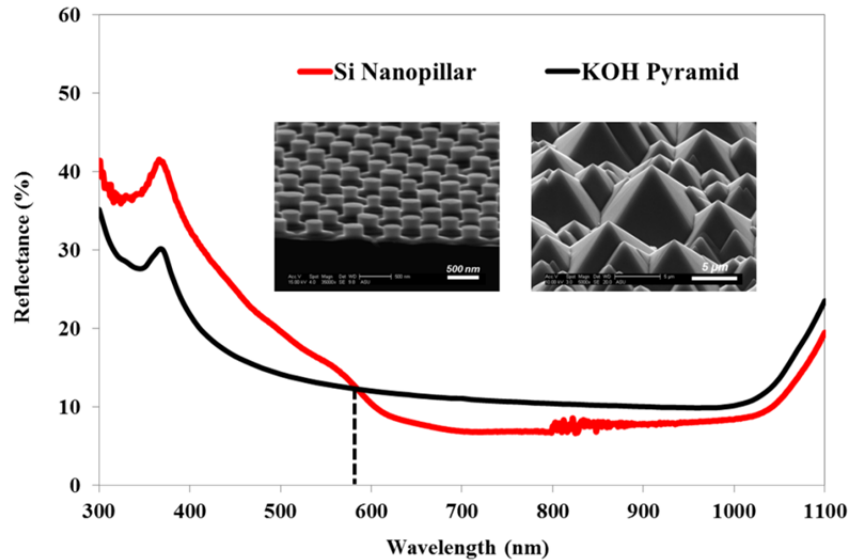


Figure 4.6. Comparison of surface Reflection between Si NPs (Red solid-line, 200nm height, 30% FF, and 600nm period) and conventional KOH solution etched random pyramid (Black solid-line) fabricated on 280um Si substrate.

In Figure 4.6, from the measured surface reflection for both surface structures, as we expected, Si NP arrayed Si surface provides significantly suppressed surface reflection for longer λ region ($580\text{nm} < \lambda < 1100\text{nm}$) compared to KOH pyramid. The

absorption enhancement is observed from 580nm, not 600nm since the Si NP array fabricated in hexagonal formation which can provide wider frequency range for absorption enhancement compared to square lattice structure. This is because wavevector, k , of hexagonal lattice structure is slight large than that of square lattice. More explanation about the effect of lattice structure is further explained in Appendix section for “statistical coupled-mode theory”.

4.1.3. Summary

From the comparison of results between computational and experimental works, highly increased light absorption for target wavelength region can be achieved by introducing a proper scale of period and optimal dimension of Si NPs including diameter and height. From the results, we confirm that Si NP array fabricated at 30% FF and 200nm height in 600nm hexagonal array can provide absorption enhancement beyond bulk-limit for target spectral region (600 ~ 1100nm).

Chapter. 5

ORGANIC PASSIVATION FOR SI SURFACE

5.1. Understanding of Molecular Contribution for Effective Quinhydrone/Methanol Organic Passivation for Silicon

5.1.1. Fundamental of Recombination Processes

Whenever the thermal-equilibrium condition of a semiconductor system is disturbed (*i.e.*, $pn \neq n_i^2$ where p = hole, n = electron, and n_i = intrinsic carrier concentration) by any external excitation, processes exist to restore the system to equilibrium (*i.e.*, $pn = n_i^2$). These processes are recombination when $pn > n_i^2$. And can occurs both in the bulk and at the surface of the semiconductor system. This recombination process is problematic especially for photovoltaic device since photo-generated excess carriers (*i.e.*, e-h pair) can be lost due to recombination processes before being extracted to the external circuit. During recombination, photo-generated electrons in the conduction band fall back to the valance band; in a consequence, recombination between the electron and hole will be occurred, and the excess carrier concentration in the semiconductor system eventually reaches its equilibrium level. For PV system, if it has a high recombination rate, the photo-generated current (J_{sc}) would be dropped and subsequently, open circuit voltage (V_{oc}) would be decreased by Eq. 5.1. Higher rate of recombination increases the magnitude of saturation current (J_0) followed by overall device efficiency drop by Eq. 5.2.

$$V_{oc} = \frac{kT}{q} \ln \left(\frac{J_{sc}}{J_0} + 1 \right) \quad 5.1$$

$$Efficiency (\eta) = \frac{J_{sc} \cdot V_{oc} \cdot FF}{Power_{in}} \quad 5.2$$

Therefore, sufficiently long carrier lifetime (τ) must be achieved for effective photo-generated carrier collection before recombination. The τ is a function of excess carrier density, Δn , and net recombination rate, U , given by Eq. 5.3.

$$\tau = \frac{\Delta n}{U} \quad 5.3$$

From Eq. 5.3, higher τ can be achieved by offering reduced net recombination (U) to semiconductor system which relies on different recombination processes occurring in the bulk and the surface of the semiconductor system. The recombination is basically originated by;

- Shockley Read Hall (SRH) recombination via defects in the band gap
- Radiative recombination
- Auger recombination
- Surface recombination

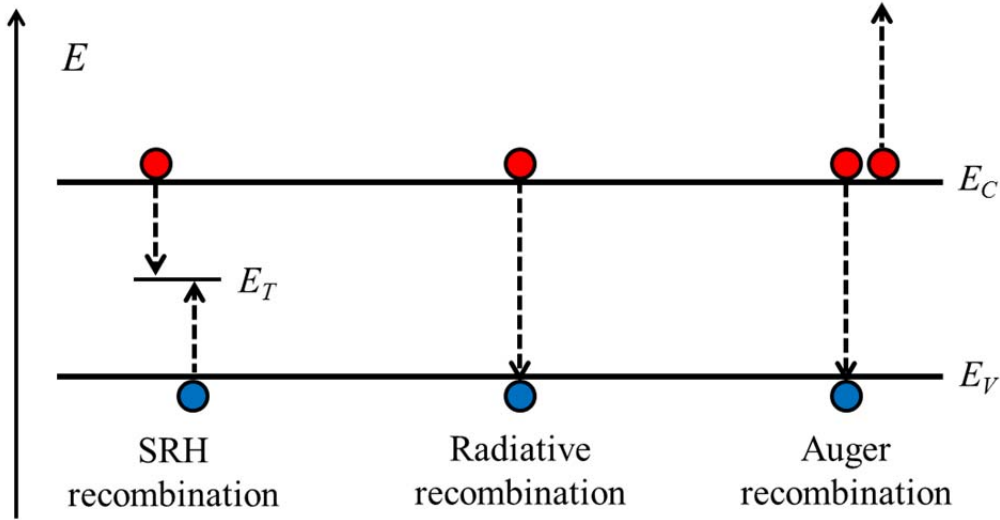


Figure 5.1. Carrier recombination mechanism in semiconductor system.[107]

SRH recombination: SRH recombination is the process directly related to impurities or crystal defects of semiconductors.[108] In this process, the e-h pairs recombined through the defects or impurities which act as deep trap states lying within the forbidden band. These deep trap states can effectively facilitate a two-step recombination process where conduction electrons can relax to the defect level and then relax to the valence band, annihilating a hole in the process. Therefore, the SRH recombination is mainly dependent on the density of trap states (N_T), their energy levels (E_T) within the band gap, the capture cross-sections of electrons (σ_n) and holes (σ_p). The SRH recombination rate, U_{SRH} , is given by Eq. 5.4.

$$U_{SRH} = \frac{np - n_i^2}{\tau_p(n + n_1) + \tau_n(p + p_1)} \quad 5.4$$

where, $n = n_0 + \Delta n$ and $p = p_0 + \Delta p$ (n_0, p_0 are the equilibrium carrier concentration and $\Delta n, \Delta p$ are the excess carrier concentration), τ_p and τ_n are the lifetime parameters (for hole and electron, respectively) whose values depend on the type of trap and the volume density of trapping defects given by Eq. 5.5 and n_1, p_1 are the parameters that introduce the dependency of the recombination rate on the trapping energy level, E_T , given by Eq. 5.6.

$$\tau_p = \frac{1}{\sigma_p N_T v_{th}} \quad \text{and} \quad \tau_n = \frac{1}{\sigma_n N_T v_{th}} \quad 5.5$$

$$n_1 = n_i \exp\left(\frac{E_T - E_i}{kT}\right) \quad \text{and} \quad p_1 = n_i \exp\left(\frac{E_T - E_i}{kT}\right) \quad 5.6$$

Therefore, using the relation between τ and U given in Eq. 5.3, SRH lifetime can be given by Eq. 5.7.

$$\tau_{SRH} = \frac{\tau_p(n + n_1) + \tau_n(p + p_1)}{(p_0 + n_0 + \Delta n)} \quad 5.7$$

where, p_0 and n_0 are carrier concentration for equilibrium condition.

Radiative recombination: For radiative recombination, Band-to-band recombination occurs when an electron moves from its conduction band state into the empty valence band state after releasing the excess energy in the form of photon. Radiative recombination process directly opposite to carrier generation process occurred

by introducing external energy to the system (*i.e.*, incident light). During the radiative recombination process, the excess electrons in the conduction band fall back to the valence band and recombine with holes. The radiative lifetime, τ_{rad} can be given by Eq. 5.8.

$$\tau_{rad} = \frac{1}{B (p_0 + n_0 + \Delta n)} \quad 5.8$$

where, B is the radiative recombination coefficient. For silicon, $B = 4.73 \times 10^{-15} \text{ cm}^3/\text{s}$ at 300 K. The radiative recombination is more prevailed in direct bandgap semiconductors like GaAs and in case of silicon the radiative recombination rate is extremely small due to its indirect band-gap where phonon emission is dominant instead of photon.

Auger recombination: For Auger recombination process, an electron and a hole recombine in a band-to-band transition, but now the resulting energy is given off to another electron or hole. The involvement of a third particle affects the recombination rate so that we need to treat Auger recombination differently from band-to-band recombination. The Auger lifetime is given by Eq. 5.9.

$$\tau_{Auger} = \frac{1}{C_p(p_0^2 + 2p_0 \cdot \Delta n + \Delta n^2) + C_n(n_0^2 + 2n_0 \cdot \Delta n + \Delta n^2)} \quad 5.9$$

where, C_p and C_n are Auger recombination coefficient for holes = $1 \times 10^{-31} \text{ cm}^6/\text{s}$ and for electrons = $2.8 \times 10^{-31} \text{ cm}^6/\text{s}$, respectively. From Eq. 5.9, we can see that τ_{Auger} is

inversely dependent on Δn^2 which implied that for heavily doped substrates or under high carrier injection conditions, τ_{Auger} will be the limiting factor for overall carrier lifetime.

Surface recombination: For semiconductor materials, recombination at surfaces and interfaces can have a significant impact on the behavior of semiconductor devices. This is because surfaces and interfaces typically contain a large number of recombination centers because of the abrupt termination of the semiconductor crystal, which leaves a large number of electrically active states. In addition, the surfaces and interfaces are more likely to contain impurities since they are exposed during the device fabrication process. The net recombination rate, U_s , due to trap-assisted recombination and generation is given by Eq. 5.10.

$$U_s = \int_{E_v}^{E_c} \frac{(n_s p_s - n_i^2) \cdot v_{th} D_{it}(E_T)}{\frac{(n_s + n_1)}{\sigma_p(E_T)} + \frac{(p_s + p_1)}{\sigma_n(E_T)}} \quad 5.10$$

where, D_{it} is the interface defect density as a function of trap energy level, E_T . n_s , p_s are the electron and hole concentration at the surface, respectively and n_i is the intrinsic carrier concentration (for Si, $n_i = 1 \times 10^{10} \text{ cm}^{-3}$ at 300 K).[109] From the net recombination rate, U_s , the surface recombination velocity, S , can be obtained by Eq. 5.11.

$$S = \frac{U_s}{\Delta n_s} \quad 5.11$$

where, Δn_s is the excess carrier density at the surface. When electrical charges are introduced to the surface by oxidation or depositing dielectric layer, the surface energy band can be bended to positive or negative direction depending on the polarity of the electrical charge; in a consequence, the surface exhibits electric field by the surface band bending which produces carrier imbalance between electron and hole at the surface, and this phenomenon is called as field effect passivation. Therefore, the effective surface recombination velocity, S_{eff} can be given by Eq. 5.12.

$$S_{eff} = \frac{U}{\Delta n(x = d)} \quad 5.12$$

where, $x = d$ indicates the length of the space charge region at the surface. Therefore, effective surface passivation requires a low surface recombination velocity in addition to low surface defect density.

After considering all of recombination processes above, the effective carrier lifetime can be given by Eq. 5.13 since carrier lifetime is inversely proportional to recombination velocity.

$$\frac{1}{\tau_{eff}} = \frac{1}{\tau_{SRH}} + \frac{1}{\tau_{rad}} + \frac{1}{\tau_{Auger}} + \frac{1}{\tau_{surface}} + \frac{1}{\tau_{emitter}}$$

where, $\tau_{emitter}$ is defined by effective carrier lifetime due to doping level of emitter.

5.1.2. Surface Passivation Approaches

There are essentially two approaches to reduce surface recombination to realize effective surface passivation for semiconductors which are (1) chemical passivation and (2) field effective passivation. The first, chemical passivation, is to reduce the density of surface states D_{it} , through saturation of surface dangling bonds which act as trap state for carriers. The second, because the rate in Eq. 5.10 is linearly dependent on the product of the density of electrons and holes at the surface (n_s and p_s), is to remove one type of charge carriers from the surface region which can be done using a local electric field, usually induced by a dielectric material, hosting a large density of fixed charges, deposited onto the surface, and is referred to as field effect passivation.

5.1.3. Motivation of This Work

Due to many promising applications over a diverse group of electronic devices, certain specialized organic materials are very much of interest. Ultra-thin organic films such as self-assembled monolayers (SAMs) are extensively studied due to their potential to modify the surface electronic properties of metallic and semiconductor materials.[110-112] Recently, organic molecules or ligands have been used for silicon (Si) surface passivation, improving the effective carrier lifetime (τ_{eff}) and reducing the surface recombination velocity (SRV) due to the importance of semiconductor surface quality as discussed in previous sections.[113, 114]

High quality passivation of Si is especially important for solar cells which require minimizing the SRV of photo-generated carriers. Conventionally, dielectric thin films such as silicon dioxide (SiO_2) and silicon nitride (SiN_x) are commonly used to provide effective Si surface passivation. However, the deposition of SiO_2 and SiN_x typically requires a high vacuum and/or high temperature process which adds cost to the devices. The use of organic coatings will reduce cost, and in addition, the rising interest in nanostructured devices that require ultra-thin and highly conformal passivation layers further motivates the organic molecular passivation approach.

A large number of studies report organic Si passivation using different organic molecules,[114, 115] but in most cases insufficient passivation qualities have limited their further development. However, a quinhydrone/methanol (QHY/MeOH) method initially developed by Takato [116], has been reported to result in a high τ_{eff} (3.3 ms) and a low SRV (7 cm/sec) at $1.0 \text{ E}15 \text{ cm}^{-3}$ carrier injection levels with n-type float-zone (FZ) Si substrates.[117] The simplicity of a Si passivation process in which the sample is just dipped in a QHY/MeOH solution at room temperature is highly attractive.[118]

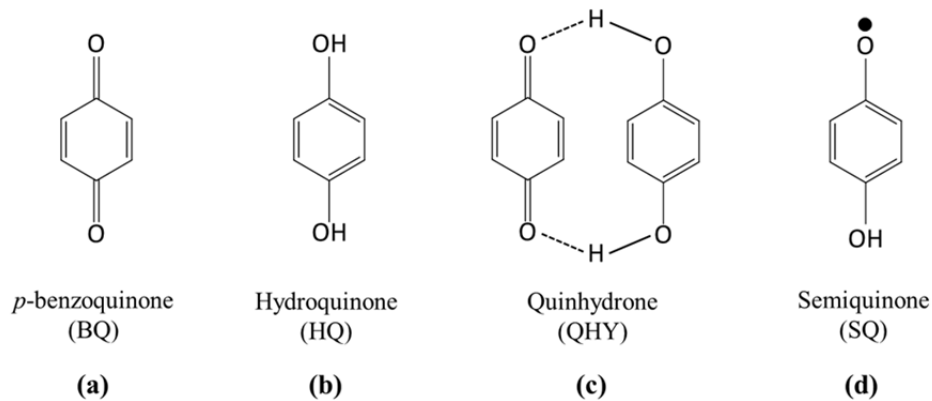


Figure 5.2. Molecular structures of (a) BQ, (b)HQ, (c) QHY, (d) SQ (passivation agent).

QHY, Figure 5.1 (c), is a very well-known charge-transfer complex between *p*-benzoquinone (BQ), Figure 5.1 (a), and hydroquinone (HQ), Figure 5.1 (b), which was initially studied by Paul et al. in 1980s.[119-122] However, the QHY charge-transfer complex is also known to be very labile in a solution environment [123, 124] and previous reports show that QHY exists as various formations of intermediate molecular radicals in different solvents.[125-127] Because of the instability of QHY in the solution, QHY itself cannot act as the passivating agent for the Si surface. The study by Cahen et al. revealed that semiquinone (SQ), Figure 1(d), is the actual passivating molecule bonding to the Si surface.[128] However, even though the QHY/MeOH passivation method has been widely studied by research groups, the contribution mechanism of each molecule (BQ and HQ) and the solvent (MeOH) for Si surface passivation is not clearly understood. In this thesis we report on the molecular contributions of BQ and HQ in MeOH to produce effective Si surface passivation in terms of (1) the uniformity of the passivation layer, and (2) SQ formation.

5.1.4. Experimental Section

To prepare the samples with organic passivation, we used 2-inch × 2-inch squares cut from n-type FZ Si <100>, 100 Ω-cm resistivity, 450 μm thick double side polished wafers. The wafers were cleaned in piranha, (H₂O₂ and H₂SO₄ mixed in 1 : 4 ratio) for 15 min followed by a 10 min rinse in DI-water and then dipped in a 10 vol% HF solution for 2 min with a 5 min DI-water rinse thereafter. The passivation with BQ/HQ/MeOH

solutions was done for 1-hr (if not specified) in a glass beaker sealed by paraffin tape to prevent solution concentration changes during the process.

Carrier lifetime and AFM measurements were performed immediately after removal of the samples from the solution and the FT-IR measurements of each solution were done within 1-hour after the solution was made. The tunneling mode (TUNA) and high resolution tapping mode AFM (HR-AFM) scans were performed on a Veeco DI-3100 using a platinum coated conductive probe and super-sharp probe (probe diameter < 2nm), respectively. τ_{eff} was measured using a Sinton lifetime tester, WCT-120, in the quasi-steady state (QSS) mode.

5.1.5. Minority Carrier Lifetime

The minority carrier lifetimes (τ_{eff}) with various solution conditions were measured to distinguish the dominant passivation molecule between the BQ and HQ for the Si surface. In the measurement of τ_{eff} with either BQ/MeOH or HQ/MeOH solutions (10 mM concentration each), as shown in Figure 5.3 (a), the BQ/MeOH produced ~ 1.7 ms at a $2.0\text{E}15 \text{ cm}^{-3}$ carrier injection level, but for the sample with the HQ/MeOH, only 68 μs was measured. From repeated measurements, we found that the τ_{eff} of HQ/MeOH treated samples never exceeded the τ_{eff} of the HF pre-cleaned only sample which indicates that the HQ/MeOH treatment just degrades the SRV of the HF treated surface.

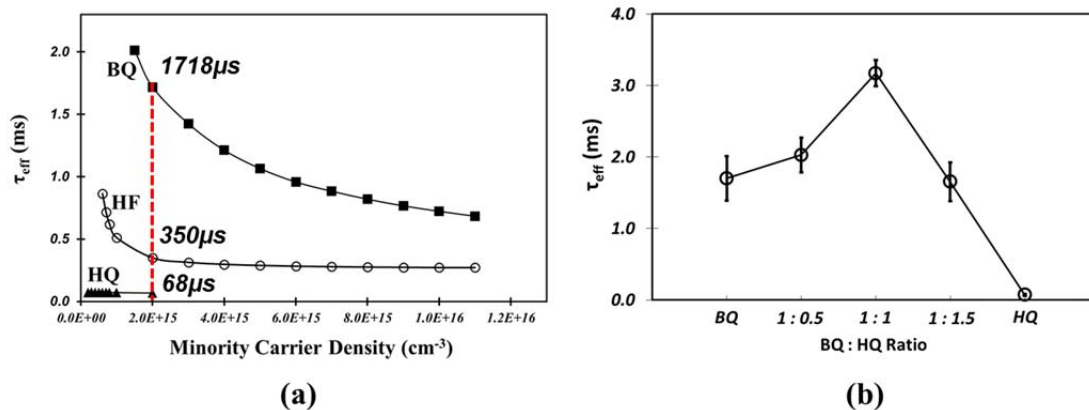


Figure 5.3. (a) Measured minority carrier lifetimes (τ_{eff}) of BQ (solid-square) and HQ (solid-triangle) treated Si compared to an HF (open-circle) only cleaned sample and (b) the measured τ_{eff} at a minority carrier density of $2 \times 10^{15} \text{ cm}^{-3}$ with 100% BQ, HQ, and various HQ mixture ratios into a fixed 10mM BQ in MeOH.

However, from Figure 5.3 (b), when we measured τ_{eff} while varying the HQ ratio with fixed 10 mM of BQ, the highest τ_{eff} , 3.2ms at $2.0\text{E}15 \text{ cm}^{-3}$ was achieved at a 1 to 1 mixture ratio of BQ and HQ (1.0 HQ), while with the other BQ : HQ ratios, 1 : 0.5 (0.5 HQ) and 1 : 1.5 (1.5 HQ), a lower τ_{eff} of 2.0ms and 1.6ms were measured, respectively. This result leads us to assume that while HQ has little involvement in the passivation reaction when it exists alone, it enhances the effectiveness of surface passivation under an optimal mixture ratio with BQ.

5.1.6. Uniformity of Organic Passivation Layer

In order to understand how HQ is involved in the Si passivation process, the Si surface morphologies after dipping in the solutions with different HQ mixture ratios were

investigated using tapping mode AFM which is a direct way to see the uniformity of the passivation layer. Because the molecular passivation layer is ultra-thin, the AFM scans were done with a super-sharp probe (probe diameter < 2nm) to generate high resolution AFM (HR-AFM) images. The HR-AFM images shown in Figure 5.4 (a) ~ (d) were obtained from the samples passivated with (a) pure BQ, (b) 0.5 HQ, (c) 1.0 HQ, and (d) 1.5 HQ with 10 mM of fixed BQ.

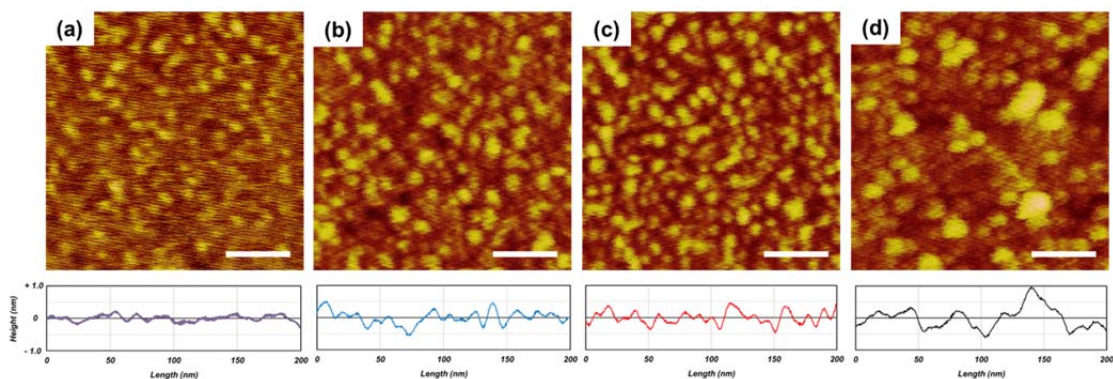


Figure 5.4. HR-AFM images of (a) pure BQ, (b) 5 mM HQ, (c) 10 mM HQ, (c) 15 mM HQ addition into 10 mM of BQ in MeOH. (Scan scale : 200 nm x 200 nm & scale bar : 50nm)

It is evident that higher HQ ratios produce more prominent molecular islands on the surface indicating higher molecular density on the surface. However, as shown in Figure 5.4 (d), the uniformity of the islands deteriorated with the 1.5 HQ mixture ratio. The cross-section profile for each sample also supports the idea that excess HQ degrades the uniformity of the passivation layer and this corresponds with the decrease in τ_{eff} shown in Figure 5.3 (b).

To further clarify the influence of HQ for uniformity of passivation layer, tunneling mode AFM (TUNA) has been also introduced to provide surface conductivity

mapping with high current sensitivity ($< 1\text{pA}$). With the TUNA mode AFM, therefore, we can distinguish the densely packed molecular area (higher conductivity) and areas where native oxide has formed (lower conductivity) because the passivation layer is not or only sparsely present. (Note: It is known that the densely packed molecule area on the Si surface delays formation of native oxide) [129, 130] Examining the TUNA mode AFM images of surfaces treated with an excess HQ ratio in Figure 5.5 (c), a large number of dark areas (white circle) were observed on the surface representing areas where rapid formation of native oxide is allowed corresponding to only localized molecular passivation when using excess HQ. With lower HQ ratios of 0.5 HQ and 1.0 HQ, however, fewer dark areas were detected. The large contrast different between 0.5 HQ and 1.0 HQ can be explained by the different density of SQ produced by H^+ exchange between BQ and HQ since SQ is the actual molecule passivating Si surface as was confirmed by Cahen et al.[128] From the HR-AFM and TUNA results, therefore, it is clear that HQ affects the uniformity of the molecular passivation layer on the Si surface.

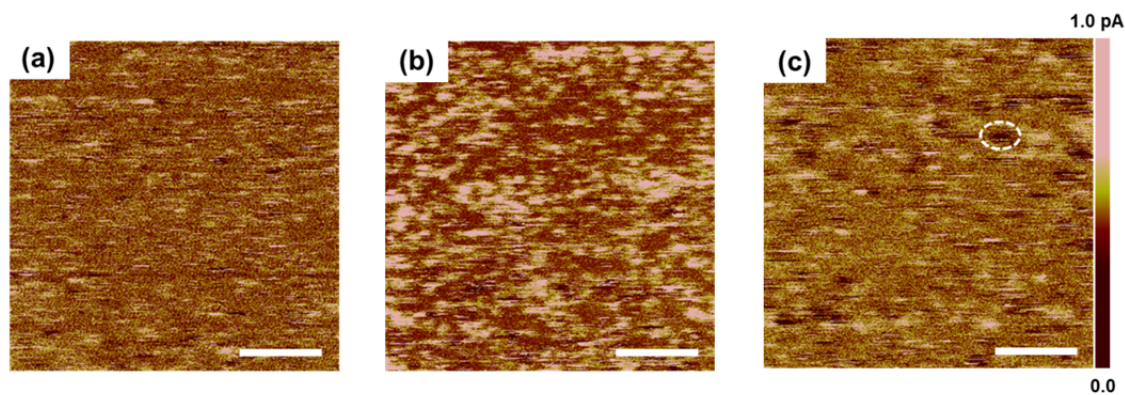


Figure 5.5. TUNA image of (a) 5 mM HQ, (e) 10 mM HQ, (f) 15 mM HQ addition into 10 mM of BQ in MeOH. (Scan scale : 200 nm x 200 nm & scale bar : 50nm), (Note: It is note-worthy that a 1 to 1 mixture ratio of BQ and HQ might also produce a more ordered molecular stacking of the passivation layer since the higher current flow (or brighter color) at the molecular island region in Figure.5 (b) might indicate that there is a well-

ordered pi-pi stacking formation among molecules which improves the conductivity of the molecular layer.[118, 131, 132])

5.1.7. Understanding of Molecular Reaction for Passivation

To better understand the reasons for the variation of passivation layer morphology and τ_{eff} with different HQ ratios, the molecular interaction between BQ, HQ and MeOH must be clarified. Therefore, FT-IR measurements were taken for the various solution conditions and Figure 5.6 (a) shows the results including pure MeOH for comparison. Note in particular the characteristic absorption for the alcohol O-H bond at 3390 cm^{-1} (stretch) and 1400 cm^{-1} (bending) which have been marked with vertical lines. BQ in MeOH produces a highly hydroxyl (O-H) deficient solution since BQ is a strong oxidizing agent which deprives a hydrogen (H^+) from MeOH. Considering that there is only 10mM of BQ in MeOH, the reaction between BQ and MeOH must be extremely fast and dynamic since the O-H peaks at 3390 cm^{-1} and $\sim 1400\text{ cm}^{-1}$ have nearly disappeared. (Note: the C-H peak at $\sim 2900\text{ cm}^{-1}$ is fairly ubiquitous, so the origin of the C-H peak intensity change is hard to specify.)[133] Further, FT-IR results showed that the addition of HQ to the BQ/MeOH solution increased the O-H peak intensity up to the 1 to 1 ratio with BQ. This is because the oxidation potential of HQ in MeOH is $\sim 0.29\text{ V}$,[82] and this is lower than that of MeOH itself, $\sim 0.38\text{ V}$. [134] Therefore, when HQ exists with BQ in MeOH, HQ acts as a strong reducing agent for BQ replacing the role of MeOH as a H^+ donor as shown in Figure 5.6 (c), so a higher fraction of MeOH molecules retain their H^+ . In a consequence, the overall absorbance of solution from O-H bonds gradually

increased as HQ ratio increases. Above a 1 to 1 ratio the intensity of the O-H peaks at both 3390 and 1400 cm^{-1} become saturated which is evidence that only a limited amount of HQ will react with BQ. This is because the BQ – HQ redox system is known to produce a stabilized intermediate molecule of semiquinone (SQ) radical by exchanging one H^+ in a non-aqueous and weak hydrogen bonding agent like MeOH.[125] In addition, from the report by Har-Lavan et al. it was confirmed the final molecular formation bonding with Si surface is the SQ molecule. In Figure 5.6, the schematic illustration is shown for SQ formation in the solution to produce Si-SQ bond for passivation.

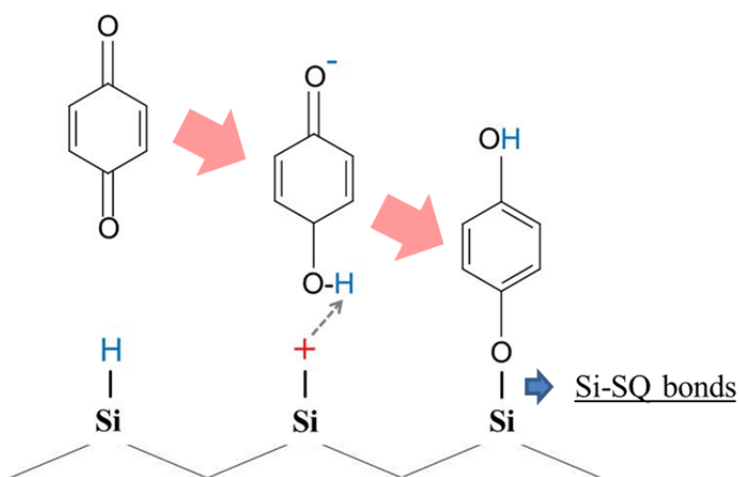
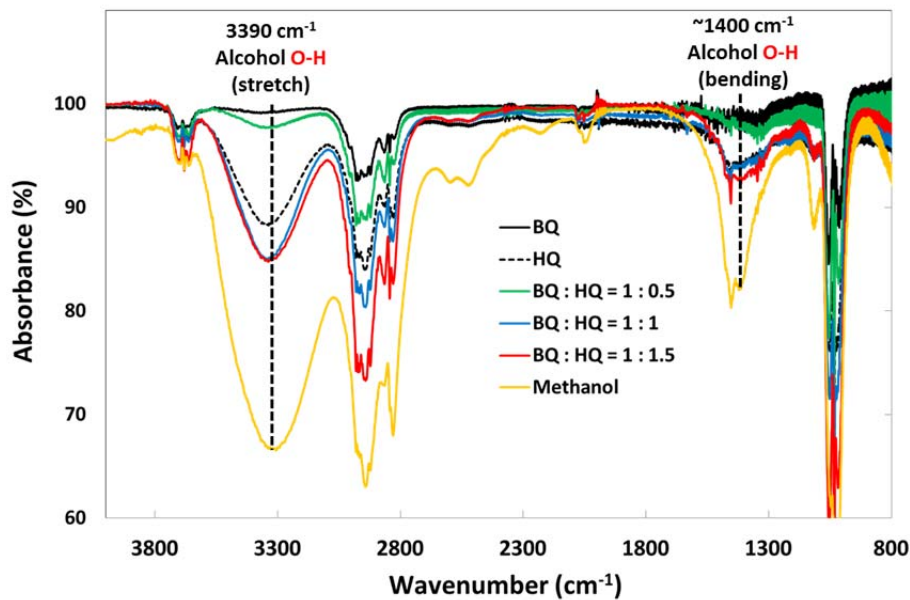


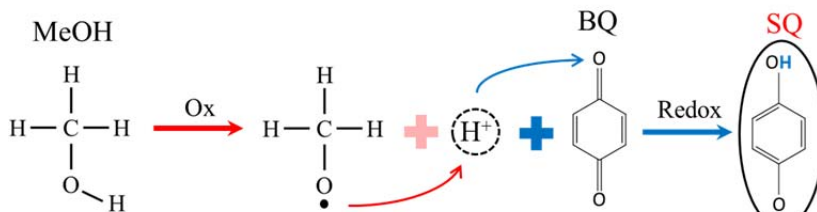
Figure 5.6. Schematic illustration for SQ formation in solution to produce Si-SQ bonding for Si surface passivation

For SQ formation, only one H^+ exchange is required, so 1 to 1 interaction between BQ and HQ should be the maximum reaction ratio which indicates excess HQ above the 1 to 1 ratio with BQ will remain un-reacted in the solution. In Figure 5.3, it was shown that HQ alone is not involved in the passivation reaction. Based on the HR-AFM images

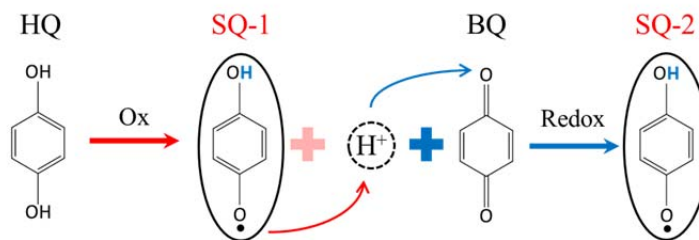
in Figure 5.4 (d), this un-reacted HQ prevents an intimate interaction between the passivation molecule and the Si surface thus deteriorating the uniformity of the passivation layer.



(a)



(b)



(c)

Figure 5.7. (a) FT-IR results of BQ, HQ, and various HQ mixture ratios into fixed BQ in MeOH and pure MeOH, (b) Reducing BQ into one SQ in BQ/MeOH, (c) two SQ formation in BHQ/MeOH.

5.1.8. Carrier Lifetime vs. Passivation Time in Solution

We also investigated the effect of treatment time in both pure BQ and BQ : HQ = 1 : 1 (BHQ) in MeOH solutions upon passivation quality using minority carrier lifetime measurements. Figure 5.7 (a) shows the measured τ_{eff} data for Si samples dipped in these solutions from 10-min to 180-min. A dramatic increase of τ_{eff} occurs with BHQ/MeOH compared to BQ/MeOH for treatment times less than 50-min. This rapid increase of τ_{eff} can be explained by the higher density of SQ in BHQ/MeOH than that of BQ/MeOH accelerating the reaction rate between SQ and Si dangling bonds. However, a gradual decrease of τ_{eff} with BHQ/MeOH was also observed as the treatment time was further increased in contrast to the BQ/MeOH solution. From repeated τ_{eff} tests for different treatment times, 1-hr and 3-hr are determined to be the optimal passivation times for BHQ/MeOH and BQ/MeOH, respectively.

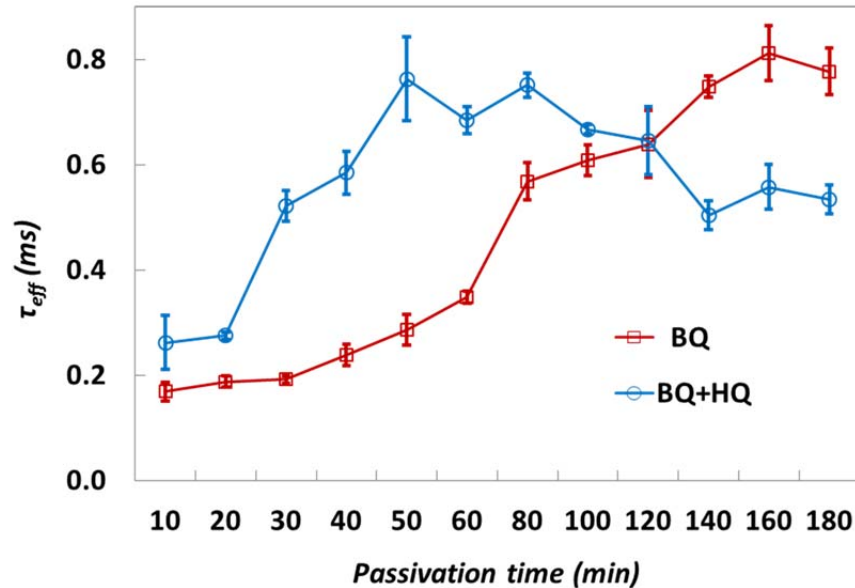


Figure 5.8. Measured τ_{eff} of Si samples after dipping in pure BQ and HQ added MeOH solution for 10-min to 180-min.

5.1.9. Kelvin Probe Measurement: Si Surface Band-Bending

To help understand the different passivation time effect with BHQ and BQ solution, the electrical property of passivated Si surface has been investigated by using Kelvin probe (KP) technique which can measure the variation of surface work-function. The work-function is extremely sensitive indicator of surface condition which is affected by absorbed or evaporated layers, surface reconstruction, surface charring, etc. Here, we used KP system to measure specifically the surface photovoltage (SPV) after organic passivation. The SPV was measured by comparison the contact potential differences (CPD) between dark and illumination condition. In Table 5.1, the measured SPV and τ_{eff} for n-type Si substrates with two different surface treatment time in BHQ, BQ, and HQ solution, 1-hr and 3-hr, respectively.

From Table 5.1, it is obvious that there would be SPV formation with BHQ and BQ treatment, but no meaningful values of SPV were observed with HQ which has good agreement with lifetime measurement results. For 1-hr passivation with n-type Si, the significant SPV has been measured along with increased τ_{eff} for both of BHQ and BQ solution compared to HF pre-cleaned sample. From the SPV results, BHQ and BQ surface passivation would induce positive (+) charge at Si surface which indicates that organic molecules offer relatively negative electric charge to the surface.

Table 5.1. N-type Si - SPV values (induced charge at Si surface) measured by Kelvin Probe, and τ_{eff} & implied Voc measured by photoconductivity decay with various surface treatments & passivation (or dipping) time.

Passivation molecules	Substrate polarity	Passivation time	SPV (meV) (3×10^{15})	τ_{eff} (μs)
BHQ	N	1-hr	(+) 314 \pm 26	1284
		3-hr	(+) 249 \pm 8	525
BQ	N	1-hr	(+) 254 \pm 13	835
		3-hr	(+) 317 \pm 44	1293
HQ	N	1-hr	(+) 13 \pm 24	68
		3-hr	(+) 20 \pm 22	91
HF	N	2-min	(-) 70	244

* BHQ \rightarrow Mixture of BQ and HQ in 1 to 1 ratio

* n-type : FZ, $>100 \Omega\text{-cm}$, $\langle 100 \rangle$, $450 \mu\text{m}$, DSP

However, after 3-hr extended passivation time, the measured SPV decreases with BHQ, but that of BQ increases. In addition, as already shown in Figure 5.7, the 3-hr passivation with BHQ produces degraded τ_{eff} in contrast to the improved τ_{eff} with BQ solution. From the comparison between SPV and τ_{eff} , results in Table 5.1, it is clear that field effect passivation is the dominant mechanism for BHQ and BQ organic passivation.[117]

In Figure 5.8, HR-AFM images are shown for 1-hr and 3-hr passivated Si samples with BHQ and BQ solution passivation which are same samples from Table 5.1.

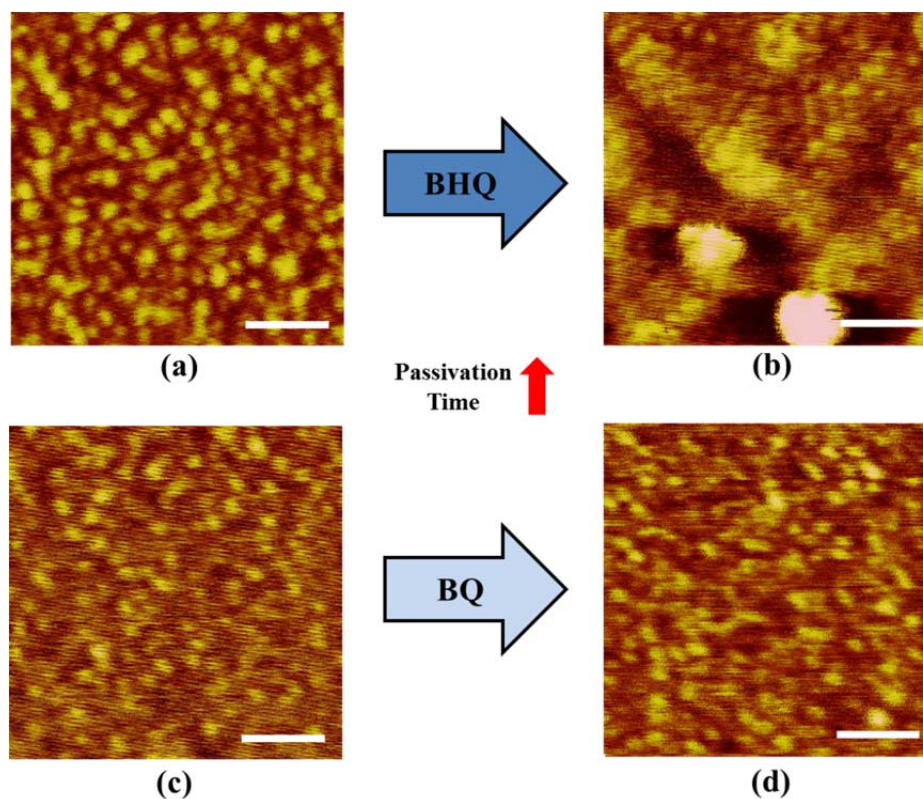


Figure 5.9. HR-AFM images of Si surface after dipping in BHQ [a, b] and BQ solution [c, d] for 1-hr and 3-hr, respectively. (scale-bar = 50nm)

From the Figure 5.8 (a) and (b), 3-hr extended passivation in BHQ/MeOH produces severe molecular aggregation on the surface, but for BQ/MeOH, the 3-hr passivation offers more prominent molecular island without aggregation which indicates BQ produces less dramatic passivation rate compared to BHQ. After analyzing the morphology, τ_{eff} , and SPV from Si samples passivated in various conditions, we can claim that the surface passivation with BHQ (or BQ) is originated from dipole moment of absorbed molecules which supports that SPV decreases with increased aggregation of molecules. This is because, as schematically illustration in Figure 5.10 (a), dipole moment is a vector quantity produced by charge asymmetry within molecules, but

random stacking of molecules in various orientations, Figure 5.10 (b), would encourage π - π interaction between stacked molecules, reducing magnitude of molecular asymmetry in a result, producing a weakened dipole moment within the molecular layer. [135]

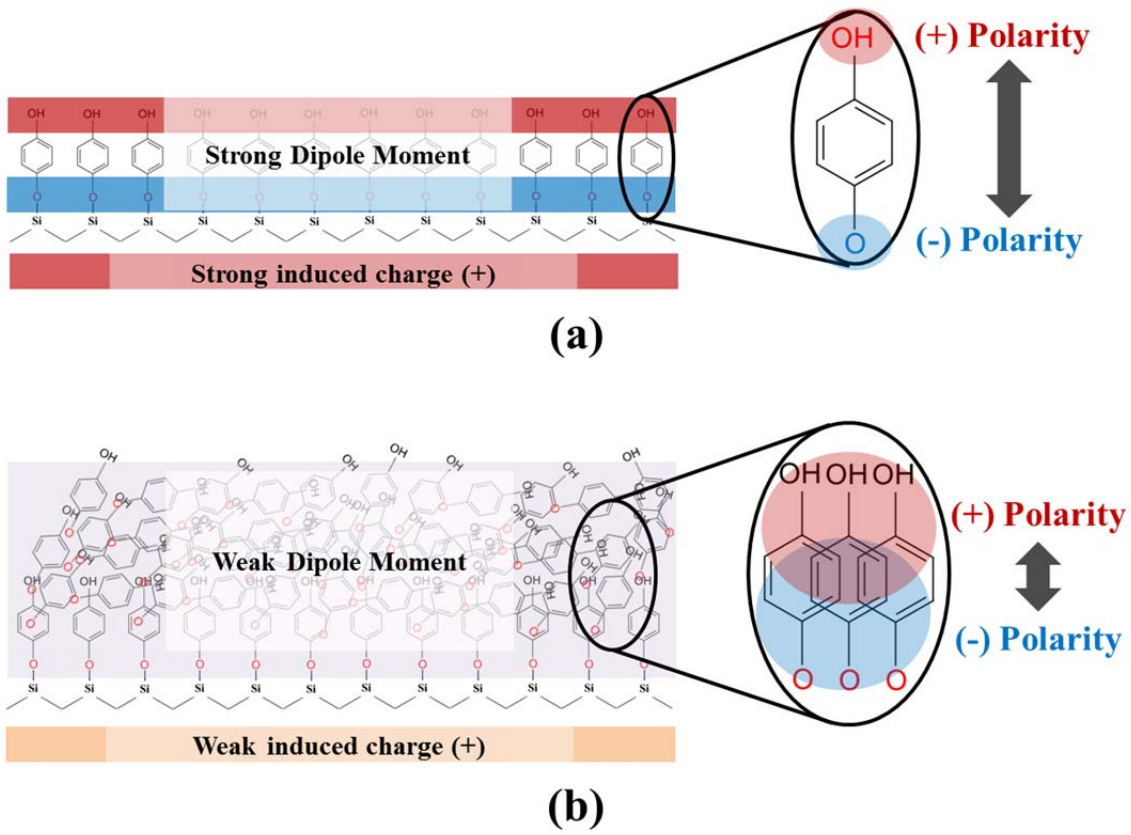


Figure 5.10. Schematic illustration of (a) SQ in mono-layer, and (b) SQ in aggregation (or multi-layer) producing different degree of molecular dipole moment

5.1.10. Summary

Because of the dramatic uniformity change of the passivation layer after HQ addition, BHQ/MeOH might not be suitable for a complex Si surface geometry which requires a very uniform and conformal ultra-thin passivation layer. Therefore, depending on the degree of surface geometrical complexity, adjusting the HQ addition and optimizing the dipping time is expected to improve the effectiveness of the passivation.

In conclusion, the role of the HQ component of the QHY/MeOH passivation of the Si surface has been clarified. From the report, HQ alone cannot provide a passivation effect for Si, but an optimal mixture ratio between HQ and BQ provides a highly accelerated passivation rate compared to pure BQ due to increased density of SQ after H^+ exchange between BQ and HQ in the solution. However, excess addition of HQ causes severe molecular aggregation and reduced coverage of the passivation layer. Even with an optimal HQ amount, an excess dipping time also produced a highly non-uniform surface morphology which, subsequently, degraded τ_{eff} . Regardless of its slower passivation rate, a less dramatic change of passivation layer morphology was observed with a pure BQ/MeOH solution as dipping time increased, producing a τ_{eff} comparable with BHQ/MeOH. Therefore, pure BQ/MeOH may provide improved passivation for complex Si surface geometries which require highly conformal and uniform passivation layers.

Chapter. 6

CONCLUSION AND FUTURE WORK

6.1. Conclusion

The objective of this thesis was to develop a fast, cost-effective, and large-area nano-lithography technique which can also offer enhanced lithographical accuracy to fabricate Si surface nanostructures with a desired period and dimension. In terms of this effort, the DMF introduced SNS spin-coating method has been successfully developed, which provides wide flexibility on pattern size and its period. This is because various sizes of SNS can be easily deposited by just changing the SNS solution concentration, which is also predictable based on the diameter of SNS. In addition, uniform and stable SNS etching with a RIE process produces well-defined and controlled scale of surface patterns since our optimized RIE provides linear SNS size reduction as the etching time increases. Our SNS introduced nano-lithography techniques can be combined with various etching technique like alkaline solution etching, MaCE, and RIE process depending on the target shape of nanostructures, since different etching techniques offer different etching properties, like etching direction and selectivity. In this dissertation, we have successfully demonstrated that nanopillars, nanotips, and inverted pyramids with a desired period and dimension can be fabricated by using different etching techniques.

In this thesis, we also utilized two different optical modeling techniques which are the FDTD and RCWA methods. From each computational method, the incident light scattering and transmitted light diffraction behavior of Si NPs array have been clearly visualized and understood. From the results of RCWA and FDTD simulation, 600nm is

found to be the optimum period of Si NPs in a hexagonal array for both improved AR properties and grating effects. Furthermore, the physical dimension of Si NP determined by Si filling fraction and height is also crucial to produce intensified forward scattering and a large fraction of high order diffraction. As a result, 600nm period, 30% FF, and 200nm height Si NPs are potentially the ideal geometric specification for thin c-Si solar cell application.

The fabricated Si NPs based on optical modeling results have successfully produced well-agreed optical property which indicates that our SNS lithography combined with MaCE can provide highly accurate period and dimension control to realize the desired optical properties for Si nanostructures.

6.2. Proposed Future Work

In this thesis, we have introduced a novel nano-lithography and fabrication process by using the SNS lithography technique, which enables the realization of Si nanostructures with a desired period and dimension. However, our SNS solvent-controlled spin-coating method is optimized for Si surfaces, not for other material; as a consequence, the process application for different materials might be challenging. Therefore, we propose to combine our SNS lithography technique with nano-imprinting process. The combination of two different technologies can provide a highly accurate master mold for nano-patterning process, which also can apply for a wide variety of different applications for different materials. In addition, nano-imprint technology has

been widely researched and is presently reaching commercial level. However, the surface nano-patterning is still highly challenging, which requires time-consuming and expensive nano-fabrication process as we described in the introduction section. Furthermore, the surface quality where nanostructure is made will be less important with nano-imprinting process since the SNS monolayer does not have to be deposited.

References

1. Becquerel, A.-E., *Mémoire sur les effets électriques produits sous l'influence des rayons solaires*. Comptes Rendus, 1839. **9**(567): p. 1839.
2. Chapin, D., C. Fuller, and G. Pearson, *A new silicon p-n junction photocell for converting solar radiation into electrical power*. Journal of Applied Physics, 1954(25): p. 676-677.
3. Young, A., *World Solar Power 2014: Countries Installing Equivalent Of 12 Nuclear Power Plants Worth Of Solar Capacity*. International Business Times, 2014.
4. Smalley, R., *Our energy challenge*. Public Lecture presented at Low Library, Columbia University, 2003. **23**.
5. F., B.J., *Episodes*. 1989: p. p. 257.
6. Yu, K. and J. Chen, *Enhancing solar cell efficiencies through 1-D nanostructures*. Nanoscale Research Letters, 2009. **4**(1): p. 1-10.
7. Kamat, P.V., *Meeting the clean energy demand: nanostructure architectures for solar energy conversion*. The Journal of Physical Chemistry C, 2007. **111**(7): p. 2834-2860.
8. Keeling, C.D., et al., *Interannual extremes in the rate of rise of atmospheric carbon dioxide since 1980*. Nature, 1995. **375**(6533): p. 666-670.
9. Mann, M.E., et al., *Global temperature patterns*. Science, 1998. **280**(5372): p. 2029-2030.
10. Dresselhaus, M., G. Crabtree, and M. Buchanan, *Basic research needs for the hydrogen economy*. 2003, Technical report, Argonne National Laboratory, Basic Energy Sciences, US DOE, <http://www.sc.doe.gov/bes/hydrogen.pdf>.
11. EPIA, *European Photovoltaic Industry Association and Greenpeace, Solar Generation 6, 2011*. 2011: p. www.epia.org.
12. Luque, A. and S. Hegedus, *Handbook of photovoltaic science and engineering*. 2011: John Wiley & Sons.
13. Green, M.A., *Third generation photovoltaics: advanced solar energy conversion*. Vol. 12. 2006: Springer.

14. Barnham, K., M. Mazzer, and B. Clive, *Resolving the energy crisis: nuclear or photovoltaics?* Nature materials, 2006. **5**(3): p. 161-164.
15. Herasimenka, S.Y., W.J. Dauksher, and S.G. Bowden, *> 750 mV open circuit voltage measured on 50 μm thick silicon heterojunction solar cell.* Applied Physics Letters, 2013. **103**(5): p. 053511.
16. Taguchi, M., et al., *24.7% record efficiency HIT solar cell on thin silicon wafer.* 2013.
17. Demésy, G. and S. John, *Solar energy trapping with modulated silicon nanowire photonic crystals.* Journal of Applied Physics, 2012. **112**(7): p. 074326.
18. Campbell, P. and M.A. Green, *Light trapping properties of pyramidally textured surfaces.* Journal of Applied Physics, 1987. **62**(1): p. 243-249.
19. Mavrokefalos, A., et al., *Efficient light trapping in inverted nanopyramid thin crystalline silicon membranes for solar cell applications.* Nano letters, 2012. **12**(6): p. 2792-2796.
20. Chong, T.K., et al., *Optimal wavelength scale diffraction gratings for light trapping in solar cells.* Journal of Optics, 2012. **14**(2): p. 024012.
21. Füchsel, K., et al. *Transparent conductive oxides for nano-SIS solar cells.* in *SPIE Eco-Photonics*. 2011: International Society for Optics and Photonics.
22. Yoo, J., G. Yu, and J. Yi, *Black surface structures for crystalline silicon solar cells.* Materials Science and Engineering: B, 2009. **159**: p. 333-337.
23. Zhao, J., et al., *24% efficient PERL silicon solar cell: recent improvements in high efficiency silicon cell research.* Solar energy materials and solar cells, 1996. **41**: p. 87-99.
24. Tsigara, A., et al., *Metal microelectrode nanostructuring using nanosphere lithography and photolithography with optimization of the fabrication process.* Thin Solid Films, 2013. **537**: p. 269-274.
25. Burrow, G.M. and T.K. Gaylord, *Multi-beam interference advances and applications: nano-electronics, photonic crystals, metamaterials, subwavelength structures, optical trapping, and biomedical structures.* Micromachines, 2011. **2**(2): p. 221-257.
26. http://www.ptreb.com/Electron_Beam_EB_Welding_EBW/.
27. http://nanooptics.uni-graz.at/ol/work/m_ebl.html.

28. Ganesan, R., et al., *Direct nanoimprint lithography of Al₂O₃ using a chelated monomer-based precursor*. Nanotechnology, 2012. **23**(31): p. 315304.
29. Han, K.-S., et al., *Enhanced performance of solar cells with anti-reflection layer fabricated by nano-imprint lithography*. Solar energy materials and solar cells, 2011. **95**(1): p. 288-291.
30. Hirai, Y., et al., *Nano-imprint lithography using replicated mold by Ni electroforming*. Japanese journal of applied physics, 2002. **41**(6S): p. 4186.
31. Hirai, Y., et al., *High aspect pattern fabrication by nano imprint lithography using fine diamond mold*. Japanese journal of applied physics, 2003. **42**(6S): p. 3863.
32. Han, K.-S., J.-H. Shin, and H. Lee, *Enhanced transmittance of glass plates for solar cells using nano-imprint lithography*. Solar energy materials and solar cells, 2010. **94**(3): p. 583-587.
33. Kuo, C.W., et al., *Fabrication of Large-Area Periodic Nanopillar Arrays for Nanoimprint Lithography Using Polymer Colloid Masks*. Advanced materials, 2003. **15**(13): p. 1065-1068.
34. Lai, C.-C., et al., *Formation mechanism of SiGe nanorod arrays by combining nanosphere lithography and Au-assisted chemical etching*. Nanoscale Research Letters, 2012. **7**(1): p. 1-6.
35. Pavesi, L., et al., *Optical gain in silicon nanocrystals*. Nature, 2000. **408**(6811): p. 440-444.
36. Schmidt, V., J. Wittemann, and U. Gosele, *Growth, thermodynamics, and electrical properties of silicon nanowires†*. Chemical reviews, 2010. **110**(1): p. 361-388.
37. Park, M.-H., et al., *Silicon nanotube battery anodes*. Nano letters, 2009. **9**(11): p. 3844-3847.
38. Geppert, T., et al., *Deep trench etching in macroporous silicon*. Applied Physics A, 2006. **84**(3): p. 237-242.
39. Kochergin, V. and H. Foell, *Novel optical elements made from porous Si*. Materials Science and Engineering: R: Reports, 2006. **52**(4): p. 93-140.
40. Huang, Z., et al., *Metal-assisted chemical etching of silicon: a review*. Advanced materials, 2011. **23**(2): p. 285-308.

41. <http://www.mpi-halle.mpg.de/index.html>.
42. Tripathi, S.K., et al., *Resolution, masking capability and throughput for direct-write, ion implant mask patterning of diamond surfaces using ion beam lithography*. Journal of Micromechanics and Microengineering, 2012. **22**(5): p. 055005.
43. Zhao, Y., et al., *A flexible chemical vapor deposition method to synthesize copper@carbon core-shell structured nanowires and the study of their structural electrical properties*. New Journal of Chemistry, 2012. **36**(5): p. 1161-1169.
44. Chang, P.-C., et al., *ZnO nanowires synthesized by vapor trapping CVD method*. Chemistry of materials, 2004. **16**(24): p. 5133-5137.
45. <http://www.nanowerk.com/spotlight/spotid=7938.php>.
46. Jang, H.S., H.-J. Choi, and S.M. Kang, *Formation of P-silicon wire by electrochemical etching using positive photoresist as an etch mask in organic electrolyte*. Electrochemical and Solid-State Letters, 2011. **14**(8): p. D84-D88.
47. Choi, D.G., et al., *Colloidal lithographic nanopatterning via reactive ion etching*. Journal of the American Chemical Society, 2004. **126**(22): p. 7019-7025.
48. Jeong, S., et al., *Hybrid Silicon Nanocone-Polymer Solar Cells*. Nano letters, 2012. **12**(6): p. 2971-2976.
49. Hulteen, J.C. and R.P. Vanduyne, *NANOSPHERE LITHOGRAPHY - A MATERIALS GENERAL FABRICATION PROCESS FOR PERIODIC PARTICLE ARRAY SURFACES*. Journal of Vacuum Science & Technology a-Vacuum Surfaces and Films, 1995. **13**(3): p. 1553-1558.
50. Huang, J.X., et al., *Spontaneous formation of nanoparticle stripe patterns through dewetting*. Nature materials, 2005. **4**(12): p. 896-900.
51. Hsu, C.-M., et al., *Wafer-scale silicon nanopillars and nanocones by Langmuir-Blodgett assembly and etching*. Applied Physics Letters, 2008. **93**(13).
52. Denkov, N.D., et al., *2-DIMENSIONAL CRYSTALLIZATION*. Nature, 1993. **361**(6407): p. 26-26.
53. Wong, S., V. Kitaev, and G.A. Ozin, *Colloidal crystal films: Advances in universality and perfection*. Journal of the American Chemical Society, 2003. **125**(50): p. 15589-15598.

54. Garnett, E. and P. Yang, *Light Trapping in Silicon Nanowire Solar Cells*. Nano letters, 2010. **10**(3): p. 1082-1087.
55. Ogi, T., et al., *Fabrication of a large area monolayer of silica particles on a sapphire substrate by a spin coating method*. Colloids and Surfaces a-Physicochemical and Engineering Aspects, 2007. **297**(1-3): p. 71-78.
56. Mihi, A., M. Ocana, and H. Miguez, *Oriented colloidal-crystal thin films by spin-coating microspheres dispersed in volatile media*. Advanced materials, 2006. **18**(17): p. 2244-+.
57. Colson, P., R. Cloots, and C. Henrist, *Experimental Design Applied to Spin Coating of 2D Colloidal Crystal Masks: A Relevant Method?* Langmuir, 2011. **27**(21): p. 12800-12806.
58. Cheung, C.L., et al., *Fabrication of nanopillars by nanosphere lithography*. Nanotechnology, 2006. **17**(5): p. 1339-1343.
59. Jiang, P., et al., *Two-dimensional nonclose-packed colloidal crystals formed by spincoating*. Applied Physics Letters, 2006. **89**(1).
60. Picard, R.H., *ABSORPTION AND SCATTERING OF LIGHT BY SMALL PARTICLES - BOHREN,C, HUFFMAN,D*. Optical Engineering, 1984. **23**(2): p. SR48-SR48.
61. Denkov, N.D., et al., *MECHANISM OF FORMATION OF 2-DIMENSIONAL CRYSTALS FROM LATEX-PARTICLES ON SUBSTRATES*. Langmuir, 1992. **8**(12): p. 3183-3190.
62. Kralchevsky, P.A., et al., *CAPILLARY MENISCUS INTERACTION BETWEEN COLLOIDAL PARTICLES ATTACHED TO A LIQUID-FLUID INTERFACE*. Journal of Colloid and Interface Science, 1992. **151**(1): p. 79-94.
63. Kralchevsky, P.A. and N.D. Denkov, *Capillary forces and structuring in layers of colloid particles*. Current Opinion in Colloid & Interface Science, 2001. **6**(4): p. 383-401.
64. Zhang, X., et al., *Two-Dimensional Self-Assemblies of Silica Nanoparticles Formed Using the "Bubble Deposition Technique"*. Langmuir, 2010. **26**(22): p. 16828-16832.
65. Das, S.K., N. Putra, and W. Roetzel, *Pool boiling characteristics of nano-fluids*. International Journal of Heat and Mass Transfer, 2003. **46**(5): p. 851-862.

66. Jansen, H., et al., *A survey on the reactive ion etching of silicon in microtechnology*. Journal of Micromechanics and Microengineering, 1996. **6**(1): p. 14-28.
67. Oh, N.R., et al., *Polystyrene Nanosphere Lithography Improved by the Insertion of a Sacrificial Polyimide Film*. Electronic Materials Letters, 2005. **1**(2): p. 135-139.
68. Easwarakhanthan, T., et al., *Spectroellipsometric analysis of CHF₃ plasma-polymerized fluorocarbon films*. Journal of Vacuum Science & Technology A, 2006. **24**(4): p. 1036-1043.
69. Spinelli, P., M.A. Verschuuren, and A. Polman, *Broadband omnidirectional antireflection coating based on subwavelength surface Mie resonators*. Nature Communications, 2012. **3**.
70. Kim, I., et al., *Silicon nanodisk array design for effective light trapping in ultrathin c-Si*. Optics Express, 2014. **22**(S6): p. A1431-A1439.
71. Rasband, W., *Imagej*. Bethesda, Maryland, USA: U.S. National Institutes of Health; 1997–2006. <http://rsbinfo.nih.gov/ij>.
72. Choi, J.-Y., T.L. Alford, and C.B. Honsberg, *Solvent-Controlled Spin-Coating Method for Large-Scale Area Deposition of Two-Dimensional Silica Nanosphere Assembled Layers*. Langmuir, 2014. **30**(20): p. 5732-5738.
73. Han, S.E. and G. Chen, *Optical Absorption Enhancement in Silicon Nanohole Arrays for Solar Photovoltaics*. Nano letters, 2010. **10**(3): p. 1012-1015.
74. Wang, H.-P., et al., *Periodic Si Nanopillar Arrays Fabricated by Colloidal Lithography and Catalytic Etching for Broadband and Omnidirectional Elimination of Fresnel Reflection*. Langmuir, 2010. **26**(15): p. 12855-12858.
75. Teng, D., et al., *High-Density Silicon Nanowires Prepared via a Two-Step Template Method*. Langmuir, 2014. **30**(8): p. 2259-2265.
76. Oh, J., H.-C. Yuan, and H.M. Branz, *An 18.2%-efficient black-silicon solar cell achieved through control of carrier recombination in nanostructures*. Nature Nanotechnology, 2012. **7**(11): p. 743-748.
77. Li, X. and P.W. Bohn, *Metal-assisted chemical etching in HF/H₂O₂ produces porous silicon*. Applied Physics Letters, 2000. **77**(16): p. 2572-2574.
78. Peng, K., X. Wang, and S.-T. Lee, *Silicon nanowire array photoelectrochemical solar cells*. Applied Physics Letters, 2008. **92**(16).

79. Li, X. and P. Bohn, *Metal-assisted chemical etching in HF/H₂O₂ produces porous silicon*. Applied Physics Letters, 2000. **77**(16): p. 2572-2574.
80. Peng, K., et al., *Fabrication of Single-Crystalline Silicon Nanowires by Scratching a Silicon Surface with Catalytic Metal Particles*. Advanced Functional Materials, 2006. **16**(3): p. 387-394.
81. Harada, Y., et al., *Catalytic amplification of the soft lithographic patterning of Si. Nonelectrochemical orthogonal fabrication of photoluminescent porous Si pixel arrays*. Journal of the American Chemical Society, 2001. **123**(36): p. 8709-8717.
82. Huang, Z., et al., *Metal-Assisted Chemical Etching of Silicon: A Review*. Advanced materials, 2011. **23**(2): p. 285-308.
83. J.A. Mucha, D.W.H., and E.S. Aydil, *"Plasma etching" Introduction to Microlithography, 2nd ed.* 1994: ACS Professional Reference book, American Chemical Society.
84. Yoo, J., G. Yu, and J. Yi, *Large-area multicrystalline silicon solar cell fabrication using reactive ion etching (RIE)*. Solar energy materials and solar cells, 2011. **95**(1): p. 2-6.
85. Bermel, P., et al., *Improving thin-film crystalline silicon solar cell efficiencies with photonic crystals*. Optics Express, 2007. **15**(25): p. 16986-17000.
86. Wang, B. and P.W. Leu, *Enhanced absorption in silicon nanocone arrays for photovoltaics*. Nanotechnology, 2012. **23**(19): p. 194003.
87. Wellenzohn, M. and R. Hainberger, *Light trapping by backside diffraction gratings in silicon solar cells revisited*. Optics Express, 2012. **20**(101): p. A20-A27.
88. Yu, Z. and S. Fan, *Angular constraint on light-trapping absorption enhancement in solar cells*. Applied Physics Letters, 2011. **98**(1): p. 011106.
89. Brongersma, M.L., Y. Cui, and S. Fan, *Light management for photovoltaics using high-index nanostructures*. Nature materials, 2014. **13**(5): p. 451-460.
90. Narasimhan, V.K. and Y. Cui, *Nanostructures for photon management in solar cells*. Nanophotonics, 2013. **2**(3): p. 187-210.
91. Li, J., H. Yu, and Y. Li, *Solar energy harnessing in hexagonally arranged Si nanowire arrays and effects of array symmetry on optical characteristics*. Nanotechnology, 2012. **23**(19): p. 194010.

92. Huang, Y.-F., et al., *Improved broadband and quasi-omnidirectional anti-reflection properties with biomimetic silicon nanostructures*. Nature Nanotechnology, 2007. **2**(12): p. 770-774.
93. Spinelli, P., M. Verschuuren, and A. Polman, *Broadband omnidirectional antireflection coating based on subwavelength surface Mie resonators*. Nature Communications, 2012. **3**: p. 692.
94. Kim, I., et al., *Silicon nanodisk array design for effective light trapping in ultrathin c-Si*. Optics express, 2014. **22**(106): p. A1431-A1439.
95. Nevière, M. and E. Popov, *Light propagation in periodic media: differential theory and design*. 2002: CRC Press.
96. Moharam, M. and T. Gaylord, *Rigorous coupled-wave analysis of planar-grating diffraction*. JOSA, 1981. **71**(7): p. 811-818.
97. Li, L., *Formulation and comparison of two recursive matrix algorithms for modeling layered diffraction gratings*. JOSA A, 1996. **13**(5): p. 1024-1035.
98. Li, L., *New formulation of the Fourier modal method for crossed surface-relief gratings*. JOSA A, 1997. **14**(10): p. 2758-2767.
99. Hench, J.J. and Z. STRAKOŠ, *The RCWA method-a case study with open questions and perspectives of algebraic computations*. Electronic Transactions on Numerical Analysis, 2008. **31**: p. 331-357.
100. Hagness, S.C. and A. Taflove, *Computational electrodynamics: The finite-difference time-domain method*. Norwood, MA: Artech House, 2000.
101. Gjessing, J., *Photonic crystals for light trapping in solar cells*. 2012.
102. Yu, Z., A. Raman, and S. Fan, *Fundamental limit of light trapping in grating structures*. Optics Express, 2010. **18**(103): p. A366-A380.
103. Yu, Z., A. Raman, and S. Fan, *Fundamental limit of nanophotonic light trapping in solar cells*. Proceedings of the National Academy of Sciences, 2010. **107**(41): p. 17491-17496.
104. Wang, Z., et al., *Broadband optical absorption by tunable Mie resonances in silicon nanocone arrays*. Scientific reports, 2015. **5**.
105. Bezares, F.J., et al., *Mie resonance-enhanced light absorption in periodic silicon nanopillar arrays*. Optics Express, 2013. **21**(23): p. 27587-27601.

106. Sgrignuoli, F., et al., *Purcell effect and luminescent downshifting in silicon nanocrystals coated back-contact solar cells*. Solar energy materials and solar cells, 2015. **132**: p. 267-274.
107. Schroder, D.K., *Carrier lifetimes in silicon*. Electron Devices, IEEE Transactions on, 1997. **44**(1): p. 160-170.
108. Shockley, W. and W. Read Jr, *Statistics of the recombinations of holes and electrons*. Physical review, 1952. **87**(5): p. 835.
109. Aberle, A.G., *Crystalline silicon solar cells: advanced surface passivation and analysis*. 1999: Centre for Photovoltaic Engineering. University of New South Wales.
110. Tredgold, R.H., *AN INTRODUCTION TO ULTRATHIN ORGANIC FILMS - FROM LANGMUIR-BLODGETT TO SELF-ASSEMBLY - ULMAN,A*. Nature, 1991. **354**(6349): p. 120-120.
111. Ulman, A., *Formation and structure of self-assembled monolayers*. Chemical reviews, 1996. **96**(4): p. 1533-1554.
112. Poirier, G.E. and E.D. Pylant, *The self-assembly mechanism of alkanethiols on Au(111)*. Science, 1996. **272**(5265): p. 1145-1148.
113. Royea, W.J., A. Juang, and N.S. Lewis, *Preparation of air-stable, low recombination velocity Si(111) surfaces through alkyl termination*. Applied Physics Letters, 2000. **77**(13): p. 1988-1990.
114. Avasthi, S., et al., *Silicon surface passivation by an organic overlayer of 9,10-phenanthrenequinone*. Applied Physics Letters, 2010. **96**(22).
115. Fletschli, F.D., et al., *Organic Thin-Film Transistors: The Passivation of the Dielectric-Pentacene Interface by Dipolar Self-Assembled Monolayers*. Langmuir, 2010. **26**(18): p. 15044-15049.
116. Takato, H., I. Sakata, and R. Shimokawa, *Quinhydrone/methanol treatment for the measurement of carrier lifetime in silicon substrates*. Japanese Journal of Applied Physics Part 2-Letters, 2002. **41**(8A): p. L870-L872.
117. Chhabra, B., et al., *High effective minority carrier lifetime on silicon substrates using quinhydrone-methanol passivation*. Applied Physics Letters, 2010. **96**(6).
118. Cornil, J., J.P. Calbert, and J.L. Bredas, *Electronic structure of the pentacene single crystal: Relation to transport properties*. Journal of the American Chemical Society, 2001. **123**(6): p. 1250-1251.

119. Patil, A.O., D.Y. Curtin, and I.C. Paul, *SOLID-STATE FORMATION OF QUINHYDRONES FROM THEIR COMPONENTS - USE OF SOLID-SOLID REACTIONS TO PREPARE COMPOUNDS NOT ACCESSIBLE FROM SOLUTION*. Journal of the American Chemical Society, 1984. **106**(2): p. 348-353.
120. Patil, A.O., D.Y. Curtin, and I.C. Paul, *INTERCONVERSION BY HYDROGEN TRANSFER OF UNSYMMETRICALLY SUBSTITUTED QUINHYDRONES IN THE SOLID-STATE - CRYSTAL-STRUCTURE OF THE 1-2 COMPLEX OF 2,5-DIMETHYLBENZOQUINONE WITH HYDROQUINONE*. Journal of the American Chemical Society, 1984. **106**(14): p. 4010-4015.
121. Scheffer, J.R., et al., *CPMAS C-13 NMR-SPECTRA OF QUINONES, HYDROQUINONES, AND THEIR COMPLEXES - USE OF CMR TO FOLLOW A REACTION IN THE SOLID-STATE*. Journal of the American Chemical Society, 1985. **107**(17): p. 4898-4904.
122. Patil, A.O., et al., *RECENT STUDIES ON THE FORMATION AND PROPERTIES OF QUINHYDRONE COMPLEXES*. Molecular Crystals and Liquid Crystals, 1986. **134**(1-4): p. 279-304.
123. Indurkar, J.R., *Tech dissertation*, in Nelson Mandela Monicipal University (NMMU). 2008.
124. Toda, F., *Organic solid state reactions*. Vol. 254. 2005: Springer.
125. Guin, P.S., S. Das, and P. Mandal, *Electrochemical reduction of quinones in different media: a review*. International Journal of Electrochemistry, 2011. **2011**.
126. Eggins, B. and J. Chambers, *Proton effects in the electrochemistry of the quinone hydroquinone system in aprotic solvents*. Journal of The Electrochemical Society, 1970. **117**(2): p. 186-192.
127. Astudillo, P.D., et al., *Electrochemical and chemical formation of a low-barrier proton transfer complex between the quinone dianion and hydroquinone*. Electrochimica Acta, 2012. **81**: p. 197-204.
128. Har-Lavan, R., et al., *Molecular field effect passivation: Quinhydrone/methanol treatment of n-Si(100)*. Journal of Applied Physics, 2013. **113**(8).
129. Haick, H., et al., *Electrical characteristics and chemical stability of non-oxidized, methyl-terminated silicon nanowires*. Journal of the American Chemical Society, 2006. **128**(28): p. 8990-8991.
130. Ho, J.C., et al., *Controlled nanoscale doping of semiconductors via molecular monolayers*. Nature materials, 2008. **7**(1): p. 62-67.

131. Anthony, J.E., et al., *Functionalized pentacene: Improved electronic properties from control of solid-state order*. Journal of the American Chemical Society, 2001. **123**(38): p. 9482-9483.
132. Holmes, D., et al., *On the nature of nonplanarity in the N phenylenes*. Chemistry-a European Journal, 1999. **5**(11): p. 3399-3412.
133. Rykaczewski, K., et al., *Guided Three-Dimensional Catalyst Folding during Metal-Assisted Chemical Etching of Silicon*. Nano letters, 2011. **11**(6): p. 2369-2374.
134. Lehn, J.M. and R. Ziessel, *PHOTOCHEMICAL GENERATION OF CARBON-MONOXIDE AND HYDROGEN BY REDUCTION OF CARBON-DIOXIDE AND WATER UNDER VISIBLE-LIGHT IRRADIATION*. Proceedings of the National Academy of Sciences of the United States of America-Physical Sciences, 1982. **79**(2): p. 701-704.
135. Atkins, P. and J. De Paula, *Atkins' physical chemistry*. 2014: Oxford University Press.
136. Tiedje, T., et al., *Limiting efficiency of silicon solar cells*. Electron Devices, IEEE Transactions on, 1984. **31**(5): p. 711-716.
137. Goetzberger, A. *Optical confinement in thin Si-solar cells by diffuse back reflectors*. in *15th Photovoltaic Specialists Conference*. 1981.
138. Campbell, P. and M.A. Green, *The limiting efficiency of silicon solar cells under concentrated sunlight*. Electron Devices, IEEE Transactions on, 1986. **33**(2): p. 234-239.
139. Fan, S. and J. Joannopoulos, *Analysis of guided resonances in photonic crystal slabs*. Physical Review B, 2002. **65**(23): p. 235112.
140. Bertolotti, M., *Waves and Fields in Optoelectronics*. Journal of Modern Optics, 1985. **32**(7): p. 748-748.
141. Fan, S., W. Suh, and J. Joannopoulos, *Temporal coupled-mode theory for the Fano resonance in optical resonators*. JOSA A, 2003. **20**(3): p. 569-572.
142. Yablonovitch, E., *Statistical ray optics*. JOSA, 1982. **72**(7): p. 899-907.

APPENDIX A

LIMIT OF ABSORPTION ENHANCEMENT IN THIN-FILM WITH GRATING STRUCTURE FABRICATED IN SUBWAVELENGTH-SCALE PERIOD

A.1. Statistical Coupled-mode Theory

For high efficiency thin Si solar cell fabrication, proper surface architectures are must be designed and built to provide effective light trapping for longer wavelength region. In many previous studies has successfully demonstrated that periodically arrayed nanostructure fabricated in the incident wavelength-scale period can provide highly effective light trapping which offers enhanced light absorption of Si beyond its bulk-limit.

The theory of light trapping was initially developed for conventional thick ($> 100\mu\text{m}$) solar cell which offers sufficient absorption length for transmitted light.[136-138] In terms of ray-optics perspective, conventional light trapping theory was utilizing the concept of total internal reflection between the absorbing and surrounding media. Realizing total internal reflection results in a significantly increased light propagation distance inside absorbing medium, in a consequence, highly enhanced light absorption can be expected. For conventional light trapping theory, with normally incident light, the absorption enhancement factor (F) has an upper limit of $4n^2$ where n is a refractive index of absorber material. This $4n^2$ is called as a bulk limit of absorption enhancement in conventional theory.

For nano-scale thin absorber in comparable or smaller than incident wavelength-scale, some of the basic assumptions from conventional theory are no more valid. Therefore, different perspective must be introduced to explain the light behavior in the reduced thickness of absorbing medium which is a rigorous electro-magnetic theory. In terms of this effort, Yu et.al has well developed a statistical coupled-mode theory to

explain the absorption enhancement for this reduced volume of media in sub-wavelength scale.[103] From the study by Yu et.al, the absorption enhancement can be achieved beyond bulk-limit of $4n^2$ if the light absorbing medium is properly designed in subwavelength-scale.

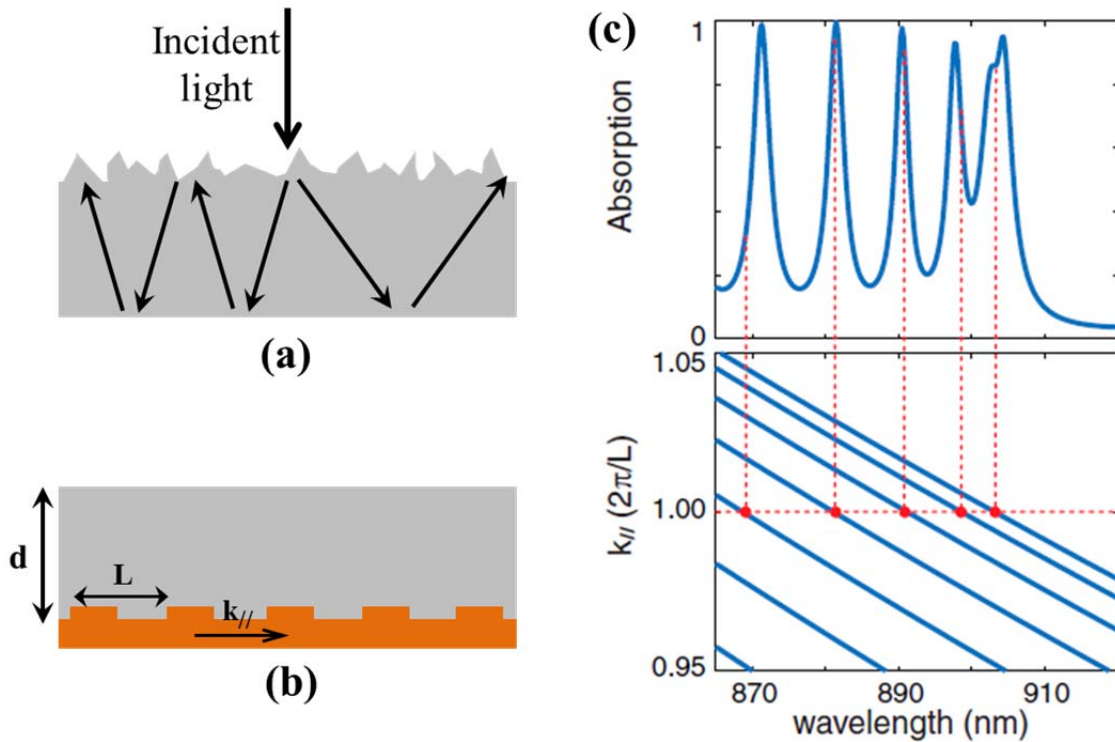


Figure A1. Light trapping with random texture and a grating structure. (A) Light trapping by randomly textured surface. (B) Light trapping using a periodic grating on a back-reflector (yellow); $d = 2 \mu\text{m}$, $L = 250 \text{ nm}$. The depth and width of the dielectric groove in the grating are 50 and 175 nm, respectively. The dielectric material is crystalline silicon. (C) Absorption spectrum [transverse magnetic (TM) mode, normal incidence] and dispersion relation of waveguide modes for the structure in B. Resonances occur when $k_{||} = 2\pi/L$ (red dots). Reprinted from Reference [103].

To illustrate statistical coupled-mode theory, we consider a high refractive index light absorbing medium in a few wavelength-scale with a perfect mirror at the bottom and

air for surrounding medium to support guided optical modes in the light absorbing medium. This is because guided mode can provide longer light propagation distance along the active layer which is longer than layer thickness. In a consequence, light trapping can be achieved by coupling incident plane waves into these guided modes when the surface has a periodic grating structure array in the subwavelength-scale period (L), Figure 1.5(a), or random Lambertian texturing, Figure 1.5(b). In this section, we will focus on grating structure in Figure 1.5(b). From the statistical coupled-mode theory, as long as L is in comparable scale to the incident wavelength-scale, each incident plane wave can couple into at least one guided mode which can couple to external plane waves, creating a guided resonance.[139]

The common absorption spectrum for Figure 1.5(b) is shown in Figure 1.5(c) which consists of multiple peaks corresponding to guided resonance. From the Figure 1.5(c), strongly enhanced absorption in between each guided resonance. However, due to the narrow spectral width of each peak, the broad absorption spectral must be reproduced by collection of these peaks which is the goal of statistical coupled-mode theory.

A.2. Overview of the Theory

This section provides overview descriptions to understand the absorption enhancement of grating structure and its limit based on previously reported statistical coupled-mode theory in reference [102]. Since the periodic grating structure improves the absorption by aggregating contribution of each resonance as shown in Figure A1.1(c), we need to identify the contribution of each resonance to the total absorption over the spectrum range. When plane wave reaches the surface of absorbing medium, the behavior of single guided resonance can be explained by the temporal coupled mode theory equation below;[140, 141]

$$\frac{d}{dt}a = \left(j\omega_0 - \frac{N\gamma_e + \gamma_i}{2}\right)a + j\sqrt{\gamma_e}S \quad Eq. (1)$$

where, a is the resonance amplitude which can be normalized in $|a|^2$ as the energy per unit area in the thin medium. ω_0 is the resonance frequency. γ_i is the intrinsic loss rate of the resonance due to material absorption. S is the amplitude of the incident plane wave which $|S|^2$ is corresponding to its intensity. Here, the plane wave coupling to the resonance is defined as a *channel*. γ_e is the leakage rate of the resonance to the channel, N , which carries the incident wave. Mostly, the grating may phase-match the resonance to other plane-wave channels as well. The theory assumes that total number of N is equal to the assumption of a conventional Lambertian emission profile as presented in reference [142], and also assume that the resonance leaks to each N with the same rate γ_e . Under these assumptions, the absorption spectrum of the resonance is;

$$A(\omega) = \frac{\gamma_i \gamma_e}{(\omega - \omega_0)^2 + \frac{(\gamma_i + N\gamma_e)^2}{4}} \quad Eq. (2)$$

For light trapping purpose, the linewidth of the resonance must be wider than the incident light spectrum. When this is satisfied, the contribution of a single resonance can be defined by a spectral cross-section;

$$\sigma = A(\omega) d\omega \quad Eq. (3)$$

which has a unit of frequency. For an incident spectrum with bandwidth $\Delta\omega \gg \sigma$, a resonance contributes $\sigma/\Delta\omega$ to the spectrally-averaged absorption coefficient. For a single resonance, from Eq. (2) and (3), its spectral cross-section is;

$$\sigma = 2\pi \frac{\gamma_i}{N + \frac{\gamma_i}{\gamma_e}} \quad Eq. (4)$$

which has its maximum value of

$$\sigma_{max} = \frac{2\pi\gamma_i}{N} \quad Eq. (5)$$

in the *over-coupling* regime when $\gamma_e \gg \gamma_i$. The requirement to operate in the strongly over-coupling regime arises from the need to achieve broad-band absorption enhancement.

From the equations above, now the upper limit of absorption in a given medium, by summing over the maximal spectral cross-section of all resonances;

$$A = \frac{\sum \sigma_{max}}{\Delta\omega} = \frac{2\pi\gamma_i}{\Delta\omega} \cdot \frac{M}{N} \quad Eq. (6)$$

where, M is number of resonances within the frequency range $\Delta\omega$. After comparing the average absorption with the single-pass absorption, the upper limit of absorption enhancement is;

$$F = \frac{A}{\alpha d} = \frac{2\pi\gamma_i}{\alpha d \Delta\omega} \cdot \frac{M}{N} \quad Eq. (7)$$

where, $\alpha = n\gamma_i / c$ is the absorption coefficient.

Eq. (7) is the main result of the theory. From the descriptions above, the maximum absorption enhancement ratio is determined by both the properties of free space, in terms of the number of accessible plan wave channel, N , as well as the thin absorber itself, in terms of the number of resonances, M .

A.3. Upper Limit of Absorption Enhancement in 2-D Grating

In this section, the theoretical upper limit of absorption enhancement with 2-D grating with a periodicity of L in both dimensions. in a square lattice. We assume that the medium has a high refractive index, n , such that the following conditions are satisfied;

$$L \gg \frac{\lambda}{n} \quad \& \quad d \gg \frac{\lambda}{n} \quad Eq. (8)$$

Under these conditions, the resonance in the film can still be approximated as forming a continuum of states. In the frequency range $[\omega, \omega + \Delta\omega]$, the total number of guided resonances in the film is;

$$M = \frac{8\pi n^3 \omega^2}{c^3} \left(\frac{L}{2\pi}\right)^2 \left(\frac{d}{2\pi}\right) \Delta\omega \quad Eq. (9)$$

Note that the number of resonances increase quadratically as a function of frequency.

When a plane wave is normally incident to the film, the grating can excite plan waves in other propagating directions in free space. The parallel wavevectors $G_{m,n}$ of these excited plane wave in free space are;

$$G_{m,n} = m \frac{2\pi}{L} \hat{x} + n \frac{2\pi}{L} \hat{y} \quad Eq. (10)$$

where m and n are integers. Therefore, these parallel wavevectors form a square lattice in the wavevector vector space as shown in Figure A1.2 (a) with blue-dots. In addition, because there are propagating plane waves, their wavevectors need to lie within a circle as defined by $|G| < k_0 \equiv \omega/c$ as shown in Figure A1.2 (a) with dash-line. The total number of different wavevector points, multiplied by two in order to take into account both polarization (s & p), defines the number of channels, N , which is required for the calculation using Eq. (7).

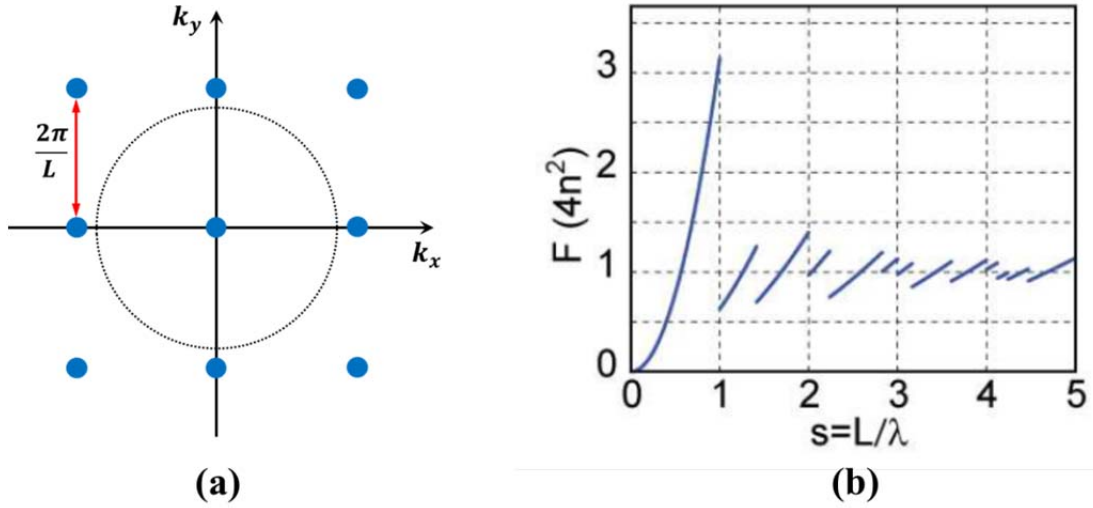


Figure A2. (a) Channels in 2-D k -space for a grating with the square lattice periodic structure and (b) its upper limit of absorption enhancement. Reprinted from Reference [102]

When normalized frequency $s = L/\lambda < 1$, only two channels ($N = 2$) are existed after accounting two polarizations in the normal direction, while the number of resonances increases with frequency, ω , quadratically. In a result, the enhancement factor, F , increases quadratically with frequency and reaches its maximum value, $4\pi n^2$, at $s = 1$ as shown in Figure A1.2 (b). However, immediately above $s = 1$, the wavelength becomes shorter than the period, L , and the number of channels increases to $N = 10$, leading to a step-function drop of the enhancement factor, F , and in the regime of $L \gg \lambda$, the theoretical limit falls to 3-D bulk limit of $4n^2$.

A.4. Effect of Periodic Lattice Structure

In this section, we briefly talk about the effect of periodic lattice structure on the enhancement factor, F . In reality, hexagonal (or tri-angluar) lattice is often found in self-assembled nanoparticle in close-packing density which is also shown in this thesis. For hexagonal lattice with period, L , the channels forms a hexagonal lattice in k-space as shown in Figure A1.3 (b). The distance between the nearest two channels at k-space is;

$$k_{hexa} = \left(\frac{2}{\sqrt{3}}\right) \left(\frac{2\pi}{L}\right)$$

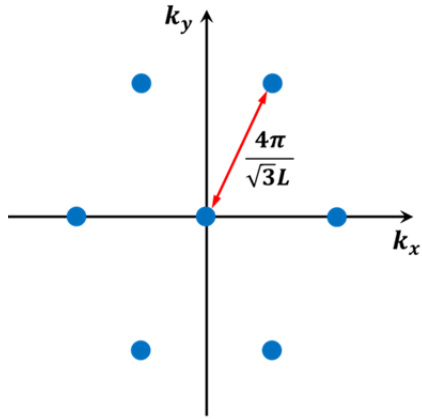
which is shown in Figure A1.3 (a) and this is larger than that of the square lattice, $2\pi/L$ (Figure A1.2 (a)). As a result, for normally incident light, the frequency range where the grating operates with only 2 channels is larger,

$$0 < s < \frac{2}{\sqrt{3}},$$

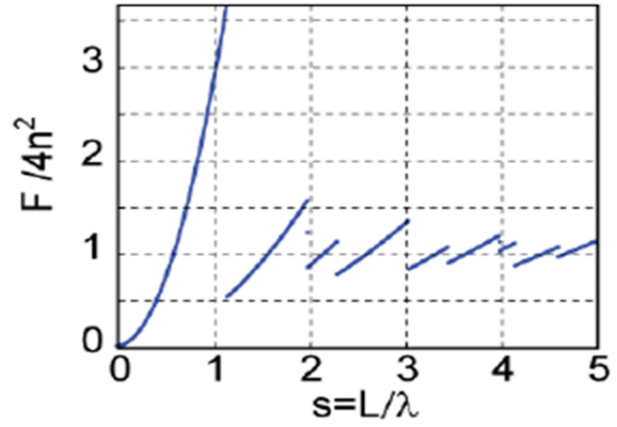
compared to the case of the square lattice ($0 < s < 1$). This leads to a higher maximum enhancement factor of;

$$F_{hexa}^{max} = 8n^2 \frac{\pi}{\sqrt{3}}$$

as shown in Figure A1.3 (b). However, like square lattice, the enhancement factor is also drop to bulk limit, $4n^2$, when the period becomes larger, $L \gg \lambda$.



(a)



(b)

Figure A3. (a) Channels in 2-D k -space for a grating with hexagonal lattice periodic structure and (b) its upper limit of absorption enhancement. Reprinted from Reference [102]